Quantitative Structural Investigations of the Water / Metal Oxide Interface

Author:

Hadeel Hussain

Thesis submitted for the Degree of Doctor of Engineering of the University College London

University College London

Department of Chemistry

June 2013

Declaration

I, Hadeel Hussain, confirm that the work presented in this thesis is my own. Where information has been derived from other sources, I confirm that this has been indicated in the thesis.

To my family...

Abstract

This thesis presents new findings that provide insight into the structural features of the adsorption of water on the $TiO_2(110)$, $ZnO(10\bar{1}0)$ and $SrTiO_3(001)$ surfaces.

After exposing the $TiO_2(110)(1 \times 1)$ surface to 1×10^{-6} mbar partial pressure of H_2O for 3 h a (2 x 1) overlayer is produced as seen with STM. This overlayer was shown to lie in registry with the Ti_{5c} rows. SXRD measurements show that every other surface Ti atom is occupied with an OH in atop position. The same average structure was found after exposing the surface to partial pressures of H_2O and after the dipping the surface in 20 ml liquid H_2O for 15 s. SXRD measurements were also collected for in-situ immersion of liquid. The results revealed the presence of a hydration layer.

We found that adsorption of water from the residual produces a (1 x 1) structure consisting of a slightly shifted H_2O/OH molecule on the $ZnO (10\bar{1}0)$ surface. After exposing the surface to a constant partial pressure of 5×10^{-7} mbar, a second water layer was detected with partial occupancy. Significant changes occurred when exposing the surface to 8 mbar partial pressure of H_2O. The results revealed that the slightly shifted H_2O/OH molecule displaces to a position that is atop of the surface Zn and the second water layer is now fully occupied.

SXRD results demonstrate that the $SrTiO_3$ (001) surface is mixed terminated with SrO and TiO_2 layers and cover equally large areas. These layers are only partially occupied and leads to a surface coverage TiO_2:SrO ratio of 68:32. When contacting this surface with a drop of water, the adsorption mode for the TiO_2 terminated terrace is molecular in nature. On the other hand, for the SrO terminated terrace it appears that dissociation is the favoured adsorption mode.

Acknowledgements

I would like to express my gratitude to both of my supervisors, Prof. Geoff Thornton and Dr. Jorg Zegenhagen, for all their support and guidance throughout my EngD. I must thank them for giving me the opportunity to work in such an exciting area of science, their expertise has helped to improve my research skills giving me the confidence to tackle any challenges ahead.

I would also like to thank Dr. Rob Lindsay, Dr. Xavier Torrelles, Dr. Oier Bikondoa and Dr. Gregory Cabailh, all of which provided invaluable support and advice during synchrotron beamtimes. A special thanks must go to Dr. Xavier Torrelles for making the daunting task of understanding SXRD theory and analysis a relatively easy one.

Many thanks to all members of the ID32 beamline and to the Thornton group for their peer support through good times and bad.

Lastly, I would like express my deepest appreciation to my family for all their support for the last four years. Special thanks are given to Mrs Gözde Hussain, without whose support, love and care this EngD would never have been.

Contents

List of Figures

List of Tables

Chapter 1

Introduction

The study of metal oxide surfaces has increasingly become a topic of general interest and perhaps the main reason is that they are virtually everywhere; all metals besides gold forms an oxide when exposed to the ambient [1] and so it is the oxide that requires our attention rather than the metal itself. As a result, there has been a whole host of investigations in the literature to try and gain an understanding of the physics and chemistry of oxide surfaces and try to improve their performance for technological applications [2–6]. Although, over the last decade or so, surface science has made great leaps and bounds there is still a lack of detailed investigations for well defined single crystal surfaces. This is in part due to the technical difficulties with working with metal oxides and/or fundamental problems related to polar surface stabilisation. They're inherently complex systems to work with often displaying a variety of structural phases even for a particular chemical composition of the surface. One of the difficulties that had to be overcome was sample preparation, a non-trivial task due to the propensity for oxide surfaces to form various forms of defects and thus increasing its complexity. As a result, there is a lack of key information regarding these surfaces when compared to that of metal surfaces; this is especially the case when considering adsorbates. There is a clear gap between model studies, which are normally conducted at/near Ultra High Vacuum (UHV) and the technologically relevant environment. Recently, however, surface scientists have began to move away from UHV to address the problem rather vigorously through the development of novel equipment with 'environmental capability', including synchrotron based probes. Broadly speaking, the systems investigated can be divided into three categories [7]: (1) Bulk oxide single crystals that are cleaved to expose surfaces of various crystallographic directions. Such examples are TiO_2 and ZnO (2) Ultra thin oxide films, which make naturally insulating oxides good conductors (eg. MgO and SiO_2) and lastly (3) The oxide that forms on top of the metal surface. Research of these particular systems are mainly focussed in the field of corrosion e.g. Fe_2O_3 and Fe_3O_4 growing on iron surfaces. In this body of work the systems investigated fall under category (1).

Water is one of the most important substances known to man and is arguably the most important molecule to understand with respect to adsorption on solid surfaces. This is mainly due to its omnipresence and hence its central role in many scientific disciplines including catalysis, corrosion protection, photovoltaics, chemistry and its many subcategories etc. Over the past few years, interest in the water-solid interface has increased where great progress has been made with water adsorption on transition metals (eg. Cu [8], Ni [9], Pd [10], Ag [11], Pt [12], Rh [13] etc...). By using several surface-sensitive experimental techniques it has been shown that beautiful arrays of highly ordered 2D superstructures and small clusters can be formed. Many of these techniques are performed in UHV and exploit a number of different probes to gather surface sensitive information eg. electrons, ions and photons. These techniques include low energy electron diffraction (LEED), surface x-ray diffraction (SXRD), auger electron diffraction (AES), x-ray and ultraviolet photoelectron spectroscopy (XPS/UPS), scanning tunnelling microscopy (STM) and many more. Originally designed to investigate metals and semiconductors, these surface sensitive techniques have been applied to the gas and liquid phase water-metal oxide interface. Some progress has been made on several oxide surfaces (eg. TiO_2 [14], ZnO [1], MgO [15], Fe_2O_3 [16], Fe_3O_4 [17], Al_2O_3 [18]).

One question that arises when adsorbing water to any solid surface is whether the molecule dissociates or not. This is of fundamental importance as a surface covered with molecular water can have different surface properties (eg. reactivity) than the same surface covered with hydroxyls, which ultimately can alter chemical reactions and processes in its application. Generally, water dissociation is a one step process whereby two products are formed, OH and H, however some reports have suggested that further dissociation of the OH may occur to produce O and a second H [19]. Here, depending on the coverage and preparation procedure different highly ordered overlayers of oxygen are present on the surface and the H recombine and desorb from the surface as H_2 gas. Of course, whether the molecule dissociates or not is highly dependant on a number of different variables, including temperature, pressure, surface morphology and structure, surface defects, water-surface interactions, water-water interactions etc. The modern surface science tools at our disposal today make answering this question a relatively easy one, many systems have been studied (see above) at sub-monolayer to monolayer coverage, an excellent example is the $TiO_2(110)$ surface. After many years of research it is now widely understood, from both an experimental and theoretical point of view, that water dissociation at room temperature occurs via oxygen defects on the surface [14, 20].

The main aim of this thesis is to bridge the so-called 'pressure gap' between our understanding and the technologically relevant environment. Here, we have exposed metal oxide surfaces to water ranging from sub-monolayer to beyond monolayer coverage in both the gas and liquid phases and probe the structure of the interface using STM and SXRD. No one technique can answer all the questions, it requires several techniques both experimental and computational to fully understand a system, however these particular surface sensitive techniques have been chosen due to the complimentary information gained; STM provides real-space imaging of the surface rich in qualitative structural information (terrace sizes, surface reconstructions, defect concentration, surface roughness etc...) that feeds into a starting model for SXRD data analysis, which provides quantitative structural information (bond angles and lengths, interlayer buckling and relaxations etc...) The materials used to try and bridge this gap are titanium dioxide, zinc oxide and strontium titanate. The following sections will aim to highlight each of their structures and importance in varying technological applications that purposely or inadvertently expose the surface to water.

1.1 $TiO_2(110)$

Titanium dioxide (TiO_2) surfaces are arguably the most studied single-crystalline metal oxide surfaces in the literature, its huge popularity stems from its importance in a wide range of technological applications that mainly take advantage of its photocatalytic properties i.e its ability to create surface electron-hole pairs under UV irradiation (Figure 1.1).

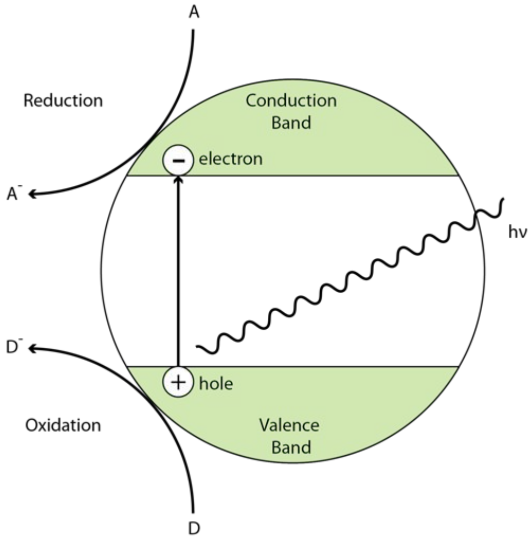

Figure 1.1: Schematic representation of the creation of surface electron-hole pairs.

It was in the 1970s, at the height of the 'oil crisis', where TiO_2 became well known to scientists of all disciplines. Fujishima and Honda [21] demonstrated the electrochemical photolysis of water, a phenomenon analogous to natural photosynthesis. With this new foundation, the research community worldwide have since discovered many uses for TiO_2 in our everyday lives. One such example is self cleaning windows, which stemmed from an AFM study on the $TiO_2(110)$ surface covered with one monolayer of stearic acid [22]. Here, they monitored the surface morphology under UV irradiation as a function of time and found that the stearic acid completely decomposed to CO_2 leaving behind a clean surface.

Another application in which TiO_2 is becoming increasingly important during our own 'oil crisis' are dye-sensitised solar cells (DSSCs) [23]. Figure 1.2 schematically illustrates the components that comprise a DSSC; at the front end (left) is the transparent anode usually made of fluoride doped tin dioxide (SnO_2:F), other materials such as zinc oxide are also being used, deposited on the back of a glass plate. On the back of this electrode TiO_2 nanoparticles are adsorbed, which creates a highly porous structure with a large surface area. This electrode is then immersed in a photosensitive dye (eg. ruthenium polypyridine or ruthenium based dyes) coating the TiO_2 nanoparticles. Finally, there is the counter electrode, usually made of platinum, which is immersed in an electrolyte (eg. iodide).

The main processes that occur in the solar cell are:

1. Incident photons of light pass through the SnO_2:F electrode and are absorbed by the dye coated on the TiO_2 nanoparticles.
2. Photons with enough energy liberate electrons from the dye leaving it in an oxidised state. The liberated electrons are injected into the conduction band of the TiO_2 nanoparticles.
3. The injected electrons are then transported between the nanoparticles by diffusion towards the front electrode (SnO_2:F) where they are collected to power a load. After flowing through the circuit and doing work the electrons are deposited at the counter electrode.
4. During process (3), the oxidised dye accepts an electron from the electrolyte leading to the regeneration of the ground state and leaving the electrolyte in an oxidised state.
5. The oxidised electrolyte then diffuses over to the counter electrode where it is reduced.

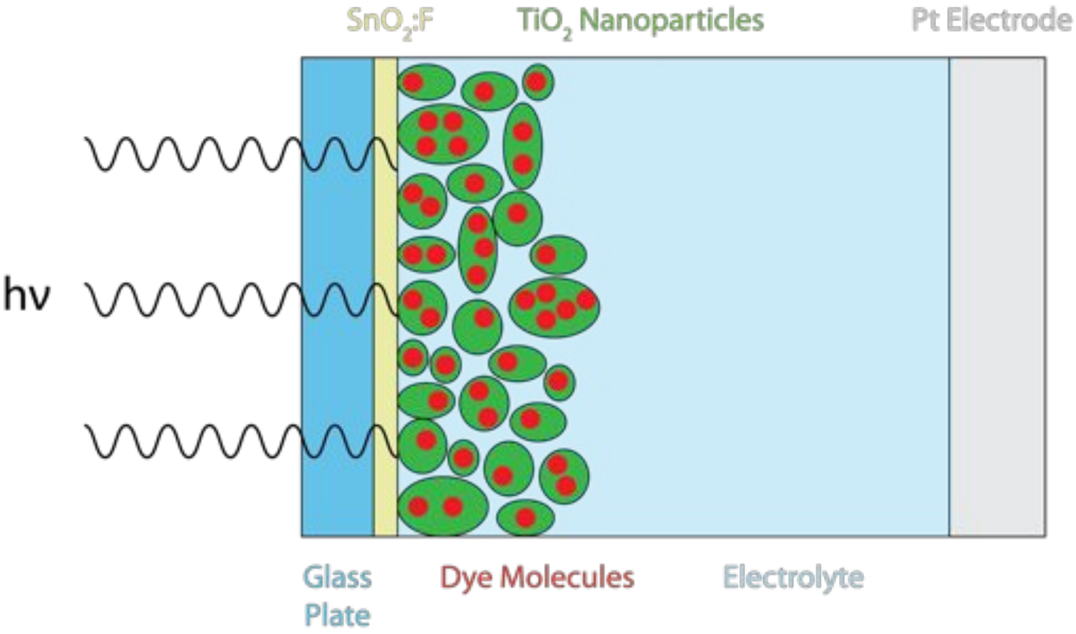

Figure 1.2: Schematic representation of the components of a dye-sensitised solar cell.

TiO_2 has a very high refractive index making it appear brighter than actually is. This property has been vastly exploited where it is now employed as a pigment in paint, coatings, plastics, toothpaste, paper and food. Other applications in which TiO_2 is commonly found are corrosion protection [24], bone implants [25].

Of the surfaces of the three polymorphs of TiO_2, rutile, anatase and brookite, the most energetically favourable rutile $TiO_2(110)$ surface has become the prototypical metal oxide surface. Rutile TiO_2 crystallises in a tetragonal structure, illustrated in Figure 4.1. The bulk unit cell comprises six-fold coordinated titanium atoms and three fold coordinated oxygen atoms. In this thesis, experiments are performed on the (110) termination only. Several excellent reviews have been written detailing the physical and electronic structures of TiO_2 surfaces, including adsorption of organic and inorganic molecules [14, 20, 26, 27].

Figure 1.3: Structure of tetragonal bulk rutile TiO_2 unit cell. Labels indicate bond distances between the octahedrally coordinated Ti atoms. Figure taken from Ref [14].

1.2 ZnO(10$\bar{1}$0)

Zinc Oxide (ZnO) is a common material which has many uses in our everyday lives. It can be found in such things as paint or colouring of paper as a white pigment, in medicine by exploiting the anti-septic properties for wound treatment and more recently, in semiconductors. Perhaps the biggest interest in ZnO in surface science to date has emerged from its role in low temperature methanol synthesis [28] and the water-gas shift reaction [29]. Methanol is produced on an industrial scale from synthesis gas (CO, CO_2 and H_2O) at elevated temperatures (200° C - 300° C) and pressures over a Cu/ZnO/Al_2O_3 catalyst. Although the preparation and use of this catalyst in methanol synthesis has been around for a number of years, the exact role ZnO plays in the reaction mechanism is still up for debate [30]. A series of investigations by Chinchen *et al* have shown [31–33] that the synthesis reactions occur only on metallic copper and that ZnO plays no role in the activity instead it is a carrier to prevent the sintering of copper particles and therefore increase the lifetime of the catalyst. In contrast, a study by Kanai *et al* have shown ZnO to enhance activity by creating Cu^+-O-Zn active sites [34]. Particular interest for this work is the preparation of Cu/ZnO catalysts; generally speaking many stages are required however most methodologies have an initial filtration and washing stage [35] where the ZnO is exposed to water.

ZnO crystallises in the hexagonal wurtzite structure characterised by tetrahedrally co-ordinated ions indicative of rather covalent semiconductors. However, ZnO is remarkably similar to ionic insulators such as MgO [36] and so represents the ionic extreme of the II-VI compound semiconductors. The most important surfaces that make up a wurtzite crystal are the mixed terminated nonpolar ($10\bar{1}0$) and ($11\bar{2}0$) surfaces and the polar zinc terminated (0001)-Zn and the oxygen terminated ($000\bar{1}$)-O surfaces, as illustrated in Figure 1.4 [37]. A review by Wöll [1] provides a comprehensive summary of the chemistry and structural properties of all the surfaces of ZnO.

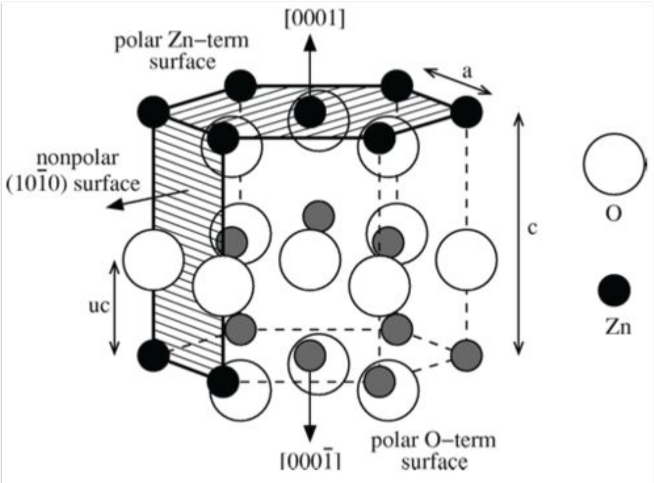

Figure 1.4: Structure of wurtzite ZnO displaying the nonpolar ($10\bar{1}0$), polar Zinc terminated (0001)-Zn and the Oxygen terminated ($000\bar{1}$)-O surfaces. Figure taken from [37].

In this thesis the focus of investigation will be on the nonpolar ($10\bar{1}0$) surface and unlike the other low Miller index surfaces, is a Tasker type 1 surface consisting of layers of mixed stoichiometry [38]. These layers carry no dipole moment therefore are electrostatically stable and do not undergo any reconstructions. It is characterised by an equal number of Zn-O dimers separated by trenches.

1.3 Nb-SrTiO$_3$(001)

SrTiO$_3$ (or STO) falls within the class of perovskite type oxides, having the general formula ABO$_3$. A ball and stick model of the bulk structure is shown in Figure 1.5. Perovskites have been the subject of intense research in recent years due to their intriguing properties and uses in many technological applications, such as an oxide fuel cell [39], oxygen sensors [40] and a substrate for thin film deposition of perovskites [41–43]. More recently, its photocatalytic properties are now being investigated [44]. Although the surfaces of STO have been the subject of intense investigation there is still a lack of experimental consensus regarding the structure of the surface. This can be assigned to the sensitivity of the surface to the preparation and processing conditions; there are at least nine different surface terminations for the STO(001) surface. Depending on the various preparation and ambient conditions, the (1 x 1), (2 x 1), (2 x 2), (6 x 2), c(4 x 2), c(6 x 2), c(4 x 4), ($\sqrt{5}$ x $\sqrt{5}$) R26.6° and ($\sqrt{13}$ x $\sqrt{13}$) R33.7° reconstructions and relaxations have been seen [45–57].

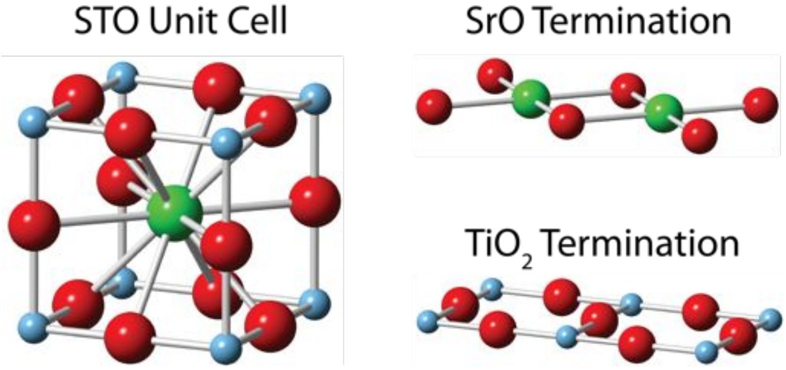

Figure 1.5: Structure of the cubic perovskite $SrTiO_3$(STO) bulk unit cell. Depending on the preparation procedure the surface can be singly terminated, with TiO_2 or SrO, or mixed terminated.

The variety of structures and chemical compositions means that perovoskite oxides, in general, have good electrical conductivity similar to that of metals. Furthermore, they exhibit good ionic conductivity and mixed ionic and electronic conductivity. It is due to these variations in electrical conductance that perovskite oxides are chosen as electrodes in solid oxide fuel cells (SOFCs). Figure 1.6 shows schematically how a SOFC works. The cell is constructed with two porous electrodes that are placed either side of a solid electrolyte. Air flows at the cathode ('air electrode') where the reduction of oxygen molecules occurs at the cathode/electrolyte interface producing oxygen ions. These ions then migrate through the electrolyte via diffusion to the anode ('fuel electrode') where oxidation of hydrogen 'fuel' produces H_2O, CO_2, heat and excess electrons. These electrons migrate through the anode to an electrical circuit to power a load and deposited back at the cathode.

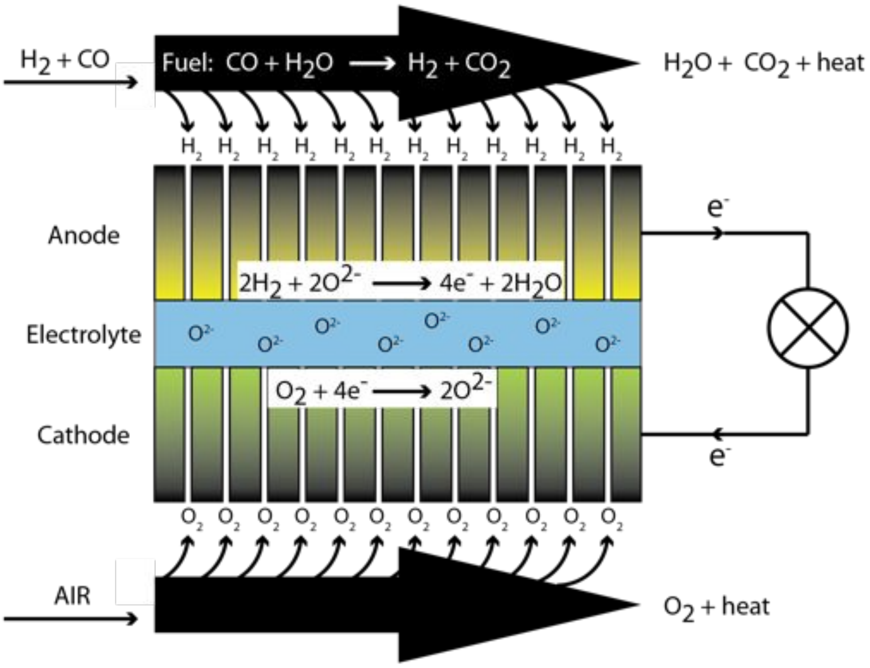

Figure 1.6: A schematic illustration of how a solid oxide fuel cell works.

In this thesis, attention focuses on the (1 x 1) surface where, depending on the preparation procedure, it is either of single termination, TiO_2 or SrO, or exhibits a mixed terminated surface, as shown in Figure 1.5.

1.4 Thesis Structure

Chapter 2 of this thesis briefly details the theoretical considerations of the experimental techniques used for investigations on the single crystal surfaces described above. These include scanning tunnelling microscopy (STM) and surface x-ray diffraction (SXRD), as well as ancillary techniques such as low energy electron diffraction (LEED) and Auger electron spectroscopy (AES).

The details of the experimental techniques are presented in Chapter 3. Focus is particularly given to the three ultra high vacuum (UHV) instruments used and their facilities for sample preparation and manipulation. Following this, a description of the ID32 beamline and the diffractometer will be given, including the use of two portable UHV 'baby' chambers.

The experimental results are given in Chapters 4-6. Starting with Chapter 4, a detailed description of a structural investigation of the rutile $TiO_2(110)$ / H_2O interface using STM and SXRD will be described. This investigation comprise three separate experiments, where the substrate is exposed to both liquid and gas-phase water, and models are proposed for each based on the STM results of this work and by Tom Woolcot.

Chapter 5 is a study of the $ZnO(10\bar{1}0)$ surface and its interaction with water at different coverages using STM and SXRD. STM results at monolayer coverage reveal an ordered overlayer of (2 x 1) periodicity. The structure of the overlayer and substrate going beyond monolayer coverage will also be discussed based on STM and SXRD results.

Chapter 6, the final results chapter, is an investigation of the adsorption of liquid water to the 0.1 wt% Nb:$SrTiO_3$ surface. Here, the structures of the 'clean' surface, prepared by annealing in an O_2 partial pressure of 1×10^{-2} mbar, the adsorption of liquid water and 'blow drying' the liquid water with a flow of N_2 will be discussed.

The final chapter of this thesis summarises the results and proposes pathways for future research to build on this work.

References

[1] C. Wöll, Prog. Surf. Sci., 82, 55, (2007)

[2] J. Strunk, K. Kahler, X. Xia, M. Muhler, Surf. Sci., 603, 1776, (2009)

[3] R. Kaváčik, B. Meyer, D. Marx, Angew, Chem, Int, Ed., 46, 4894, (2007)

[4] T. M. Parker, N.G. Condon, R. Lindsay, F.M. Leibsle, G. Thornton, Surf. Sci., 415, L1046, (1998)

[5] X. Yin, A. Birkner, K. Hnel, T. Lber, U. Khler, C. Wȯll, Phys. Chem. Chem. Phys., 8, 1477, (2006)

[6] Y. Wang, B. Meyer, X. Yin, M. Kunat, D. Langenberg, F. Traeger, A. Birkner, C. Wȯll, Phys. Rev. Lett., 95, 266104, (2005)

[7] U. Diebold, S.C. Li, M. Schmid, Annu. Rev. Phys. Chem., 61, 129148 (2010)

[8] P.S. Uy, J. Bardolle, M. Bujor, Surf. Sci., 129, 219231 (1983)

[9] D. Sebastiani and L.D. Site, J. Chem. Theory Comput., 1, 78-82 (2005)

[10] Y. Cao, Z.X. Chen, Phys. Chem. Chem. Phys., 9, 739746 (2007)

[11] E.M. Stuve, R.J. Madix, B.A. Sexton, Surf. Sci. Lett., 111, A379 (1981)

[12] H. Ogasawara, B. Brena, D. Nordlund, M. Nyberg, A. Pelmenschikov, L.G.M. Pettersson, A. Nilsson, Phys. Rev. Lett., 89, 276102 (2002)

[13] A.A. Rar, V.P. Ivanov, React. Kinet. Catal. Lett., 34, 445450 (1987)

[14] U. Diebold, Surf. Sci. Rep., 48, 53, (2003)

[15] M.A. Johnson, E.V. Stefanovich, T.N. Truong, J. Gunster, D.W. Goodman, J. Phys. Chem. B, 103, 3391-3398 (1999)

[16] S. Yamamoto, T. Kendelewicz, J.T. Newberg, G. Ketteler, D.E. Starr, E.R. Mysak, K.J. Andersson, H. Ogasawara, H. Bluhm, M. Salmeron, G.E. Brown, A. Nilsson, J. Phys. Chem. C, 114, 22562266 (2010)

[17] K.T. Rim, D. Eom, S.W. Chan, M.F. Stephanopoulos, G.W. Flynn, X.D. Wen, E.R. Batista, J. Am. Chem. Soc., 134, 1897918985 (2012)

[18] Z. Suprynowicz, J. Rayss, A. Patrykiejew, Chromatographia, 12, 742-746 (1978)

[19] M. Eder, K. Terakura, J. Hafner, Phys. Rev. B, 64, 115426 (2001)

[20] C. L. Pang, R. Lindsay, G. Thornton, Chem. Rev., (2013)

[21] A. Fujishima and K. Honda, Nature, 238, 37 (1972)

[22] P. Sawunyama, L. Jiang, A. Fujishima, K. Hashimoto: J. Phys.Chem. B, 101, 11000 (1997)

[23] B. O′Regan, M. Gratzel, Nature, 35, 737, (1991)

[24] A. Shanaghi, A. R. Sabour, T. Shahrabi, M. Aliofkhazraee, Protection of Metals and Physical Chemistry of Surfaces, Vol. 45, No. 3, pp. 30531, (2009)

[25] K. S. Brammer, C. J. Frandsen, S. Jin, Trends Biotechnol. 30(6), 315-22, (2012)

[26] C. L. Pang, R. Lindsay, G. Thornton, Chem. Soc. Rev., 37, 2328, (2008)

[27] C. Sun, L.-M. Liu, A. Selloni, G.Q. (Max) Lu, S.C. Smith, J. Mater. Chem., 20, 10319 (2010)

[28] T. S. Askgaard, J. K. Norskov, C. V. Ovesen, P. Stoltze, J. Catal., 156, 229, (1995)

[29] D. S. Neusome, Rev. Sci. Eng., 21, 275, (1980)

[30] M.S. Spencer, Top. Catal., 8, 259266 (1999)

[31] G.C. Chinchen,K. Mansfieldand, M.S. Spencer, Chem. Tech, (1990)

[32] G.C. Chinchen, K.C. Waughand, D.A. Whan, Appl. Catal, 25, 101 (1986)

[33] G.C. Chinchen, P.J. Denny, J.R. Jennings, M.S. Spencer, K.C. Waugh, Appl. Catal. 36, 1 (1986)

[34] Y. Kanai, T. Watanabe, T. Fujitani, T. Uchijima, J. Nakamura, Catal. Lett., 38, 157163 (1996)

[35] M.S. Spencer, Topics in Catalysis, 8, 259266 (1999)

[36] P. Cox, Metal Oxides: An Introduction to Their Electronic Structure and Properties, (Clarendon Press, Oxford, 1992)

[37] B. Meyer, D. Marx, Phys. Rev. B., 67, 035403, (2003)

[38] P. Tasker, J. Phys. C, 12, 497784 (1979)

[39] J. C. Ruiz Morales, J. Canales-Vzquez, C. Savaniu, D. Marrero-Lpez, W. Zhou, J. T. S. Irvine Nature(London)., 439, 568, (2008)

[40] W. Menesklou, H. J. Schreiner, K. H. Hardtl, E. Ivers-Tiffee, Sensors and Actuators: B Chemical., 59, 184, (1999)

[41] A. Ohtomo and H. Y. Hwang, Nature(London)., 427, 423, (2004)

[42] F. Silly, M. R. Castell, Appl. Phys. Lett., 85, 3223, (2004)

[43] M. Marshall, M. R. Castell, Phys. rev. Lett., 102, 146102, (2009)

[44] J. G. Mavroides, J. A. Kafalas, and D. F. Kolesar, Appl. Phys. Lett., 28, 241, (1976)

[45] T. Matsumoto, H. Tanaka, T. Kawai, S. Kawai, Surf. Sci., 278, L153, (1992)

[46] M. Naito, H. Sato, Physica C., 229, 1, (1994)

[47] Q. D. Jiang, J. Zegenhagen, Surf. Sci., 338, L882, (1995)

[48] Q. D. Jiang, J. Zegenhagen, Surf. Sci., 425, 343, (1999)

[49] G. Charlton, S. Brennan, C.A. Muryn, R. McGrath, D. Norman, T.S. Turner, G. Thornton Surf. Sci., 457, L376, (2000)

[50] T. Kubo, H. Nozoye, Phys. Rev. Lett., 86, 1801, (2001)

[51] A. Kazimirov, D.M. Goodner, M. J. Bedzyk, J. Bai, C. R. Hubbard, Surf. Sci., 492, L711, (2001)

[52] C. H. Lanier, A. van de Walle, N. Erdman, E. Landree, O. Warschkow, A. Kazimirov, K. R. Poeppelmeier, J. Zegenhagen, M. Asta, L. D. Marks, Phys. Rev. B., 76, 045421, (2007)

[53] M. R. Castell, Surf. Sci., 505, 1, (2002)

[54] M. R. Castell, Surf. Sci., 516, 33, (2002)

[55] K. Johnston, M.R. Castell, A.T. Paxton, M.W. Finnis, Phys. Rev. B., 70, 085415, (2004)

[56] V. Vonk, S. Konings, G.J. van Hummel, S. Harkema, H. Graafsma, Surf. Sci., 595, 183, (2005)

[57] F. Silly, D.T. Newell and M.R. Castell. Surf. Sci. Lett., 600, L219, (2006)

Chapter 2

Theoretical Considerations

This chapter will examine the theoretical aspects of the techniques used in this body of work. It will begin with some basic concepts in physical chemistry regarding adsorption on surfaces. Focus will then be turned to the techniques, primarily focusing on scanning tunnelling microscopy and surface x-ray diffraction. Other surface characterisation techniques will also be discussed, namely low energy electron diffraction and auger electron spectroscopy. Finally the chapter will end by introducing the reader to the theory behind the analysis procedure.

2.1 Adsorption on Surfaces

2.1.1 Langmuir Adsorption Isotherm

The Langmuir adsorption isotherm is a model used to interpret the behaviour of adsorbent molecules on surfaces and to determine the total surface area of any given substrate. As with all fundamental models certain assumptions must be made in order for it to be derived and there is no exception for this model [1]:

1. The surface contains a number of equivalent sites that can only be occupied by one molecule.
2. At constant temperature, there is a dynamic equilibrium between the gas phase and the first adsorbed layer on the surface.
3. There is a continuous collision of gas molecules with the surface. If the molecule collides with an unoccupied surface site then it forms a bond a sticks whereas if it collides with an occupied surface site it is reflected back in to the gas phase.
4. Once the molecules have adsorbed they do not migrate from their site and the enthalpy of adsorption remains constant at all coverages.

For associative adsorption, if we assume there is a dynamic equilibrium between the gas phase molecules and the surface then:

$$M_g + S \rightleftharpoons M - S \tag{2.1}$$

where M_g is the adsorbent molecule and S is the surface site. Associated with the reaction are the rate constants, k_a and k_d, for adsorption and desorption, respectively. The rate of adsorption and desorption are then defined as:

$$\text{rate of adsorption} = k_a P(1-\theta) \tag{2.2}$$

$$\text{rate of desorption} = k_d \theta \tag{2.3}$$

where P is the pressure and θ is the fractional coverage of the adsorbate on the surface and is defined as $\theta = \frac{\text{Number of surface sites occupied by adsorbate}}{\text{Total number of substrate adsorption sites}}$

At equilibrium:

$$k_a P(1-\theta) = k_d \theta \tag{2.4}$$

and so the Langmuir adsorption isotherm is defined as:

$$\theta = \frac{KP}{1+KP} \tag{2.5}$$

where $K = \frac{k'_a}{k'_d}$. This equation can be used to predict how the fractional coverage of the adsorbate changes with pressure for associative adsorption. For dissociative adsorption, we now have:

$$M_{2(g)} + 2S \rightleftharpoons 2(M-S) \tag{2.6}$$

The rate of adsorption and desorption are similar to the associative case however are now in the second order due to more surface sites being needed for dissociative adsorption:

$$\text{rate of adsorption} = k'_a P(1-\theta^2) \tag{2.7}$$

$$\text{rate of desorption} = k'_d \theta^2 \tag{2.8}$$

At equilibrium, the rate of adsorption = the rate of desorption therefore:

$$k'_a P(1-\theta^2) = k'_d \theta^2 \tag{2.9}$$

Rearranging gives the Langmuir adsorption isotherm for dissociative adsorption:

$$\theta = \frac{\sqrt{\{KP'}}{\sqrt{1+KP'}} \tag{2.10}$$

2.1.2 Bonding to Surfaces

There are two main categories used to describe an adsorbate bonding to a surface, these are physisorption and chemisorption. In the former, the bonding between the adsorbate and substrate is considered to be a van der Waals-type interaction where bonding is weak but long range. Here, there is a negligible exchange of electrons as bonding is characterised by the redistribution of the electron density. Typical examples of physisorption are molecular adsorption of noble gases, where the weak bonding is exploited to determine the surface area of a substrate via the Langmuir model.

Chemisorption is characterised by an exchange of electrons and is usually distinguished from physisorption on the value of the enthalpy of adsorption, where anything greater than 35 kJ mol^{-1} is considered to be chemisorbed. This strongly depends on the surface coverage of the adsorbate as adsorbate-adsorbate interactions can decrease the enthalpy of adsorption by the formation of highly ordered overlayers.

2.1.3 Adsorption Kinetics

If, for a given system, we assume that molecules from the gas phase are chemisorbed to the surface then the probability of the molecule being associatively adsorbed is given by:

$$S = S_0(1-\theta) \tag{2.11}$$

where $S = \frac{\text{rate of adsorption of molecules by the surface}}{\text{rate of collision of molecules with the surface (Z)}}$. This is termed the so-called sticking probability (S) and S_0 is the sticking probability when the fractional coverage, θ, is zero i.e the sticking probability has a linear relationship with the number of unoccupied sites on the surface. However, it is often the case that this linear function does not hold when considering purely Langmuir theory and so it is necessary to consider the existence of a precursor state.

One of the assumptions from the Langmuir model is that if any adsorbate molecule collides with an occupied surface site then it simply rebounds back into the gas phase however in reality this may not happen. The adsorbate may form a weak van der Waals-type bond and diffuse over the surface for some finite length of time until it chemisorbs to an unoccupied surface site. The strength of bond depends on the mechanism of adsorption, where there are two types of precursor states; intrinsic, where the adsorbate molecule physisorbs to an occupied surface site, and extrinsic, where the adsorbate physisorbs to an unoccupied surface site. An important factor in the kinetics of adsorption is the residence time, which is defined by:

$$\tau = \tau_0 \exp -\Delta H_{AD}/RT \tag{2.12}$$

This estimates the lifetime an adsorbate molecule spends on the surface, which is critically dependant on the magnitudes of the physi/chemisorbtion potential energy well and the substrate temperature. It is generally thought that the longer the molecule is on the surface then there is a higher probability of energy exchange and the deeper the potential energy well, the longer the residence time.

$$\alpha = \frac{T_f - T_i}{T_s - T_i} \tag{2.13}$$

Equation 2.13 calculates the rate at which adsorbate molecules colliding with the surface can lose their energy and hence adsorb to the surface. It is defined as the thermal accommodation coefficient, α, where T_i is the initial temperature of the molecule in the gas phase, T_f is the temperature of the molecule after colliding with the surface and T_s is the surface temperature.

2.2 Scanning Tunnelling Microscopy (STM)

2.2.1 Introduction

Since its development in the 1980s, by Binnig and Rohrer [2,3], the STM has had a tremendous impact on many fields of surface science and nanotechnology. Its popularity has risen over the past few years and has found itself in remarkably diverse areas, not only used to work on highly ordered single crystal surfaces but on polymer surfaces, biological systems and even manipulating single atoms.

Although revolutionising many fields, the principles behind the STM are relatively simple. An atomically sharp tip is moved to within a few angstroms of a conducting or semi-conducting surface and a small potential difference is applied between the tip and surface. A small but measurable current is detected due to the phenomenon of tunnelling and is a function of tip-surface separation. If the tip is then rastered over the surface, a contour map of the local density of states (LDOS) of the surface can be built up.

Perhaps the greatest attraction of the STM is the generation of real space images at the atomic scale which, with refinement, can now be routinely achieved on model systems [4, 5]. Such images can provide key information and aid in the computational analysis by providing starting models (eg. SXRD) as will be shown in Chapters 4 and 5. However, there are limitations to the technique; STM lacks elemental specificity and it can sometimes be difficult to interpret images, particularly when dealing with adsorbates. Furthermore, the fabrication of atomically sharp tips, needed to obtain atomically resolved images, is at best a trial and error method.

In its simplest form and classically speaking, the gap between the tip and surface can be modelled as a one dimensional energy barrier [3]. Electrons cannot cross unless they have a greater kinetic energy than the barrier height, however due to wave-particle duality there is a finite probability of them tunnelling through it. At a low bias voltage and temperature, the tunnelling current is given by:

$$I \propto \exp(\pm \kappa d), \tag{2.14}$$

where I is the tunnelling current, d is the width of the barrier and κ the decay constant for the wave within the barrier given by:

$$\kappa = \sqrt{\frac{2m\Phi}{\hbar^2}}, \tag{2.15}$$

where m is the mass of the electron and Φ is the average work function of the tip and surface. From Equation 2.2 it can be seen that there is an exponential dependency of the tunnelling current with the tip-surface separation. For typical values of the work function, on the order of a few eV, changes in d in the region of 1 Å give rise to an order of magnitude variation in the tunnelling current. This relationship is what leads to the atomic scale sensitivity of STM.

This approach provides a very simple explanation of the behaviour of STM, however a better understanding of the process is necessary and for this we turn to the works of Tersoff and Hamann [6,7], Chen [8] and Lang [9,10].

2.2.2 Tersoff and Hamann

Tersoff and Hamann used a more sophisticated approach to determine the tunnelling current by considering the overlap of the tip wavefunction and the sample wavefunction. Using this approach, which is suitable to apply Bardeen's perturbation formula, for first order pertubation the current is given by:

$$I = \frac{2\pi e}{\hbar} \sum_{\mu v} f(E_\mu)[1 \pm f(E_v + eV)] \cdot |M_{\mu,v}|^2 \delta(E_\mu \pm E_v), \tag{2.16}$$

where *f(E)* is the Fermi Function, V is the applied voltage bias, M_{uv} the tunnelling matrix between the states ψ_μ of the tip and ψ_v of the surface and E_μ and E_v are the energy of the two states in the absence of tunnelling. In the small voltage and low temperature limit this becomes:

$$I = \frac{2\pi}{\hbar} e^2 V \sum_{\mu v} |M_{\mu,v}|^2 \delta(E_v \pm E_F) \delta(E_\mu \pm E_v), \tag{2.17}$$

where E_F is the Fermi level. By treating the tip as a point probe, the system is able to gain the maximum possible resolution and leads to a matrix element that is proportional to the amplitude of ψ_v at the position r_0 of the tip and hence:

$$I \propto \sum_{v} |\psi_v \overrightarrow{r_0}|^2 \delta(E_v \pm E_F), \tag{2.18}$$

This relationship highlights the approximation that the tunnelling current is proportional to the surface LDOS at E_f.

2.2.3 Lang

The models presented above do not take into account the composition of the tip or surface. Lang extended the wave function approach to consider the imaging of different atoms by modelling the tip and surface as two flat electrodes; one with a Na atom termination and the other with adsorbate atoms (C, O, Na and S). He showed that the Na 3s and S 2p resonances create an increase in the LDOS at the Fermi level, whereas the He, C and O 2p resonances cause a reduction, illustrated in Figure 2.1 [9].

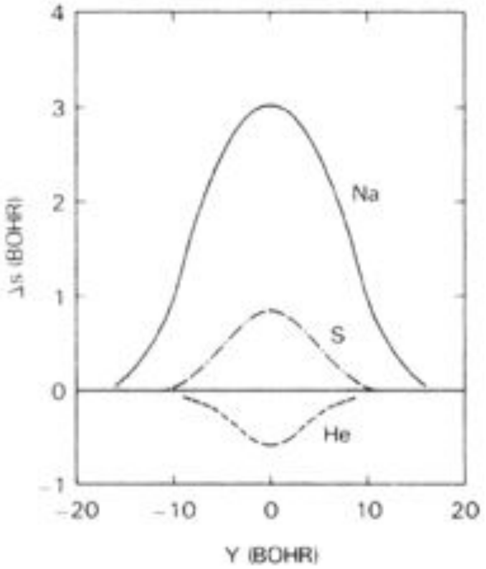

Figure 2.1: Tip displacement (△s) vs. lateral displacement (Y) for an STM scan with adsorbates for small bias voltages. Taken from Ref [9].

2.2.4 Chen

The approaches described above rely on modelling the tip electrons with spherically symmetric s-wave functions and predict a resolution of about 6 Å which is in clear disagreement with the experimentally obtained results, which resolve atoms at a spacing of about 3 Å. Chen's work highlights the point that the s-wave approximation is unlikely to be valid for common tip materials (W, Ir, Pt) whose Fermi level DOS are largely composed of d states. In addition to this, W is often considered to have highly localised d_{z^2} dangling bonds which play a major role in tunnelling. An important result that arose from Chen's work, displayed in Figure 2.2 [8] is that of the reciprocity principle, showing that a d_{z^2} tip scanning an s wave sample is the same as an s wave tip scanning a d_{z^2} sample.

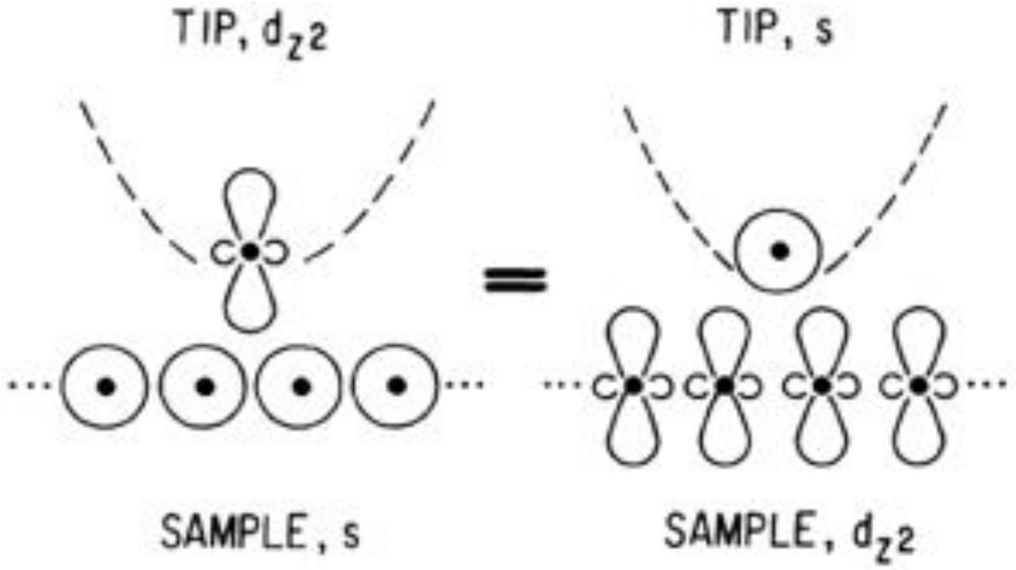

Figure 2.2: Illustration of the reciprocity principle. Taken from Ref [8]

2.3 Low Energy Electron Diffraction (LEED)

LEED was first demonstrated in the 1920s by Davisson and Germer [11]. In LEED, electrons impinge upon a surface where they are elastically backscattered and analysed in the energy range 20 - 1000 eV. Electrons in this energy range are excellent probes of the surface structure for two reasons:

1. their inelastic mean free paths are between ∼5 - 20 Å, meaning they can only penetrate a few atomic layers into the surface; and
2. their de Broglie wavelengths are of the same order of magnitude as the interatomic spacings between the atoms / molecules at the surface and hence may undergo diffraction if they are periodically arranged.

The wavelength of the electrons maybe estimated using the modified de Broglie equation:

$$\lambda(\mathring{A}) = \sqrt{\frac{150.6}{E(eV)}}, \tag{2.3.19}$$

Electrons with energies ranging between 20 and 1000 eV yield de Broglie wavelengths between 2.74 - 0.388 Å.

Figure 3.10 illustrates a simplistic view of how an electron beam is diffracted from an ordered array of atoms separated by a distance d. If two incident parallel beams, k_i, diffract off the surface then the path difference, △s, between the two is given by:

$$\triangle s = d(\sin\psi - \sin\phi), \tag{2.3.20}$$

In the case of coherent interference between the incident beams, the path difference must be an integer value of wavelengths. So, Equation 2.3.20 becomes:

$$n\lambda = d(\sin\psi - \sin\phi), \tag{2.3.21}$$

If n =1 and the values of ψ and ϕ are known then, by using Equation 2.3.21, the separation of atoms, d, can be calculated.

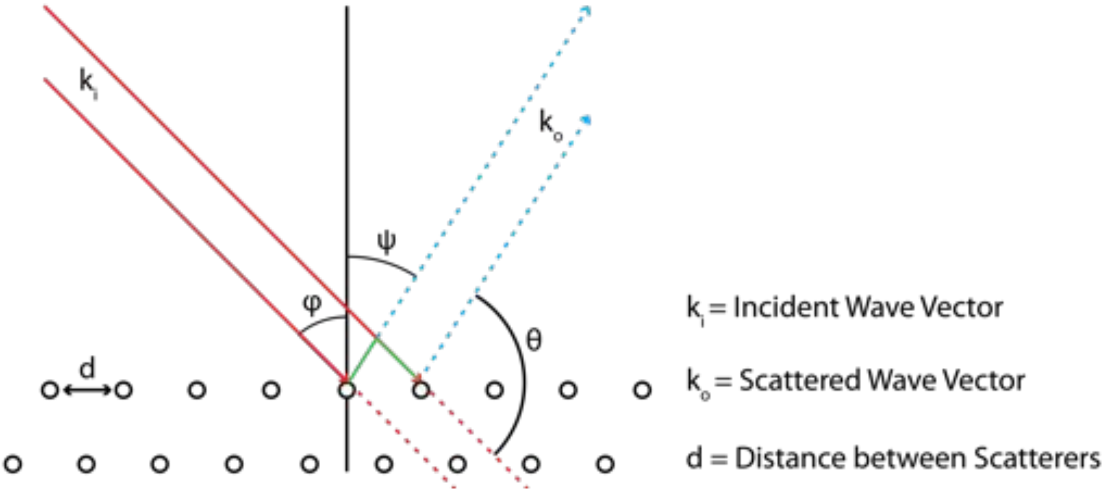

Figure 2.3: A simplistic view of the diffraction of two incident parallel beams, k_i, from an ordered array of atoms. ψ and ϕ are the angles of the incident and diffracted beam, respectively. θ is the angle of diffraction between the incident beam, k_i and the diffracted beam, k_o. Green lines visualise the path difference.

2.4 Auger Electron Spectroscopy (AES)

AES, since its discovery by Pierre Auger, has become one of the most widely used techniques for determining precise elemental information of surfaces [12, 13]. Figure 2.4 illustrates the Auger effect.

An incident photon (or electron) causes photoemission of a core electron (i) resulting in a hole. This core level hole may be neutralised by an electron of lower binding energy ('down' e^-, ii). As a result, a quantum of energy $\triangle$E, equal to the difference in binding energy between the core hole and the 'down' electron, now becomes available and can be removed in one of two ways:

1. as a photon (X-ray fluorescence) or
2. transferred to a third electron, which can escape with a kinetic energy E_{kin}.

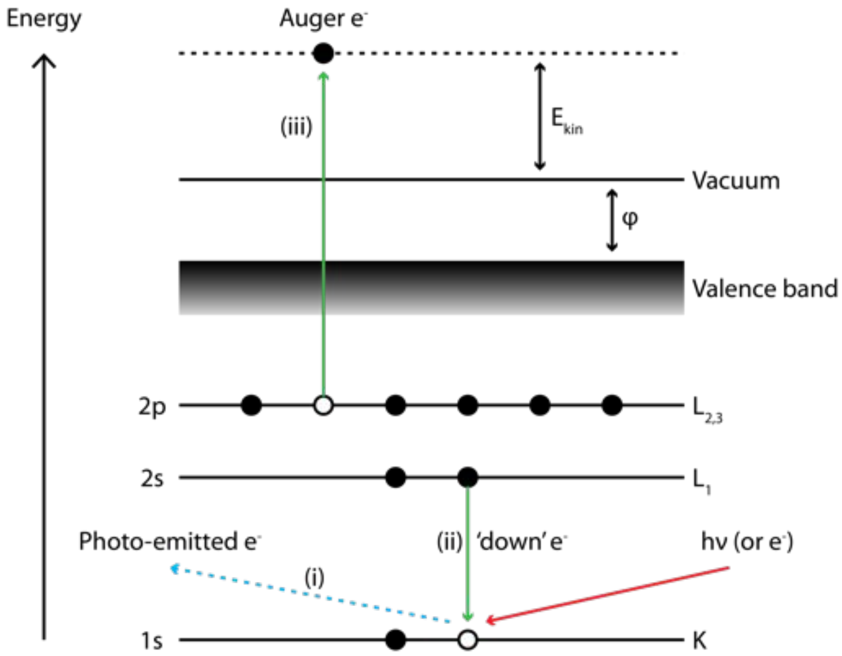

Figure 2.4: The Auger Process

This third electron is termed the Auger electron (iii) the kinetic energy of which is given by:

$$E_{kin} = E_K - E_{L1} - E_{L2,3} - \phi, \tag{2.4.1}$$

Auger peaks are usually assigned by three letters which specify the levels from which the core hole, the 'down' electron and the Auger electron originate. In the example shown in Figure 2.4, the Auger transition is termed $KL_1L_{2,3}$. The energy of the Auger electron is solely dependent on the binding energy of the electrons within the atom and so can be used for elemental identification.

When, the initial core level excitation is performed with electrons the small Auger peaks are superimposed on a large secondary electron background. For this reason electron excited spectra are displayed as the derivative (dN/dE) rather than the simple N(E) energy distribution.

2.5 Surface X-ray Diffraction (SXRD)

2.5.1 Introduction

X-rays have long been established as a routine technique for determining the bulk structures of materials. Their small scattering contribution, and thus a weak interaction with matter, allows x-rays to penetrate more deeply into a material when compared to other surface sensitive scattering techniques such as electron diffraction. This allows the investigation of buried interfaces, including solid-liquid and solid-gas. In contrast to electron diffraction techniques, multiple scattering processes are typically negligible and so a kinematical approach to the scattering theory is sufficient, reducing calculations of theoretical data from hours to seconds.

The surface of a material is typically described as the first few atomic layers and so there is a fraction of scattering atoms at the surface/interface than in the bulk. This leads to a very low scattering intensity signal. Over the last 30 years SXRD has become an established technique for the characterisation of systems and interfaces, largely due to the advent of synchrotron radiation, which provides sufficient counting statistics and reduces count time. In order to exploit x-rays for the employment of surface science, the incident radiation must be at grazing incidence with respect to the surface plane [14, 15], otherwise too a high a signal will be measured from the bulk of the crystal overlaying the signal from the surface.

The following section of this chapter will give a brief overview of the theoretical considerations of SXRD. All measurements conducted and given in this report were undertaken at the European Synchrotron Radiation Facility (ESRF), Grenoble on the ID32 beamline. As a beamline dedicated to studying surfaces and interfaces using x-ray diffraction, this particular beamline was chosen due to its high brilliance beam.

2.5.2 Single Crystal X-ray Diffraction

The scattering cross-section of x-rays is much smaller than that of electrons and so the diffraction of x-rays by the crystal can be assumed to be single scattering - the kinematical approximation [16]. Specifically, inelastic or Compton scattering are neglected as these do not give rise to coherent diffraction features. Figure 2.5 illustrates the typical geometry seen in a SXRD experiment.

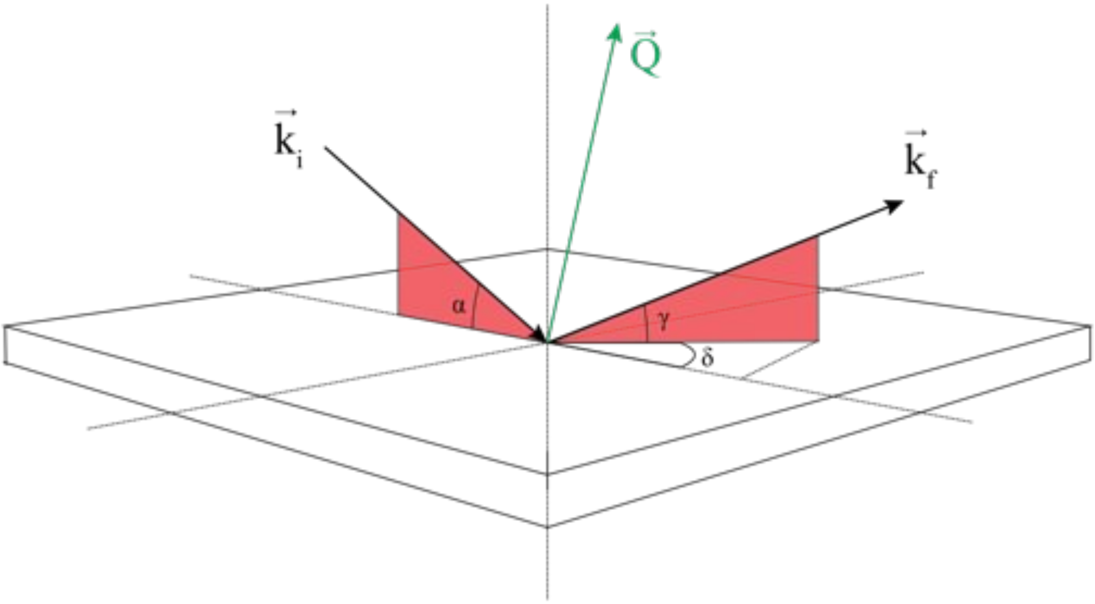

Figure 2.5: Simplistic view of the typical geometry in an SXRD experiment

If $\vec{k}_i$ represents an incident wave vector in momentum space and $\vec{k}_f$ represents the wave vector of a scattered wave, then for elastic scattering:

$$|\vec{k}_f| = |\vec{k}_i|, \tag{2.5.1}$$

$$\vec{k}_f - \vec{k}_i = \vec{Q}, \tag{2.5.2}$$

where $\vec{Q}$ is the scattering vector or momentum transfer.

The scattered intensity of a crystal that consists of N$_i$ unit cells in the directions ($\vec{a_1}$, $\vec{a_2}$, $\vec{a_3}$) of the real space lattice, at a fixed position in reciprocal space is proportional to the square of the structure factor [17]:

$$I(\vec{Q}) \propto |F_{crys}(\vec{Q})|^2 \tag{2.5.3}$$

$$= \left| \sum_{j_1=1}^{N_1} \sum_{j_2=1}^{N_2} \sum_{j_3=1}^{N_3} \underbrace{\sum_{j_1=1}^{N} f_j(\vec{Q}) \cdot e^{(2\pi i \vec{Q} \cdot \vec{r_j})} \cdot e^{(-B_j \vec{Q}^2/(4\pi)^2)}}_{\mathrm{F}\mu(\vec{Q})} \cdot e^{(2\pi i \vec{Q} \cdot (j_1 \vec{a_1} + j_2 \vec{a_2} + j_3 \vec{a_3}))} \right|^2 \tag{2.5.4}$$

$$= |F_\mu(\vec{Q}|^2 \cdot \left| \sum_{j_1=1}^{N_1} \sum_{j_2=1}^{N_2} \sum_{j_3=1}^{N_3} e^{(2\pi i \vec{Q} \cdot (j_1 \vec{a_1} + j_2 \vec{a_2} + j_3 \vec{a_3}))} \right|^2 \tag{2.5.5}$$

$$= |F_\mu(\vec{Q}|^2 \cdot \frac{\sin^2(\frac{1}{2} N_1 \vec{Q} \vec{a_1})}{\sin^2(\frac{1}{2} \vec{Q} \vec{a_1})} \cdot \frac{\sin^2(\frac{1}{2} N_2 \vec{Q} \vec{a_2})}{\sin^2(\frac{1}{2} \vec{Q} \vec{a_2})} \cdot \frac{\sin^2(\frac{1}{2} N_3 \vec{Q} \vec{a_3})}{\sin^2(\frac{1}{2} \vec{Q} \vec{a_3})} \tag{2.5.6}$$

$$= |F_\mu(\vec{Q}|^2 \cdot {N_1}^2 \cdot {N_2}^2 \cdot {N_3}^2, \quad for\ large\ N_1, N_2, N_3. \tag{2.5.7}$$

The structure factor, $F_\mu(\vec{Q})$, is dependent on the atomic scattering factor, $f_i(\vec{Q})$, which is given by the Fourier transform of the electron density, ρ_j, of the atoms at position $\vec{r_j}$ in the unit cell:

$$f_j(\vec{Q}) = \int_{cell} \rho_j(\vec{r}) e^{(i\vec{Q}\cdot\vec{r})} d^3\vec{r}, \tag{2.5.8}$$

Thermal vibrations scatter intensity into an incoherent background, reducing the intensity of diffraction features. This is taken into account by the Debye-Waller factor, $\exp(\frac{-B_i \vec{Q}^2}{(4\pi)^2})$, which is related to the mean square thermal vibration amplitude $\langle \mu^2 \rangle$ as [17]:

$$B = 8\pi^2 \langle \mu^2 \rangle, \tag{2.5.9}$$

2.5.3 Surface Diffraction

The bulk of a material is described as having an infinite periodicity in the in-plane and out-of-plane directions. However, with the introduction of a surface the periodicity breaks giving rise to a lattice which is semi-infinite in the out-of-plane direction with respect to the surface. Scattering is no longer isotropic and as a result tails of diffuse intensity appear perpendicular to the surface, passing through the bulk diffraction spots - Crystal Truncation Rods (CTRs).

The intensity distribution of these CTRs is strongly influenced by the surface structure i.e relaxations, reconstructions and roughness. This is visualised in Figure 2.6 [18]. Here it can be seen that an expansion of the first layer away from the bulk leads to an asymmetry in the intensity distribution in between the Bragg peaks and is heavily influenced by the amount the surface has relaxed by. As for a rough surface, the symmetry of the ideal-terminated surface remains. However, a substantial decrease in the intensity is seen in between the Bragg peaks which is due to the destructive interference arising from scattering between the layers.

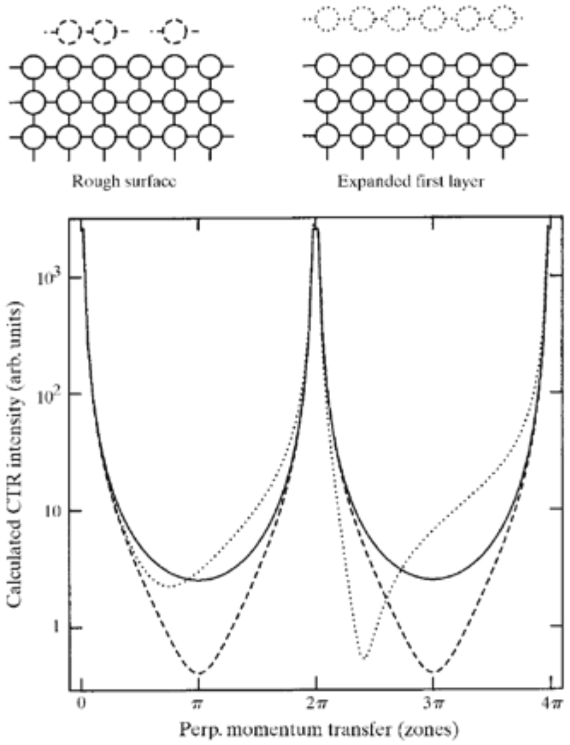

Figure 2.6: The effect of relaxations and surface roughness on the intensity distribution of a CTR. The filled line represents the perfect surface i.e an ideal-termination. The two dotted CTR profiles are calculated for a rough surface and for a surface where the top layer has relaxed away from the bulk. Taken from Ref [18].

Robinson [19] derived an expression for the intensity distribution of a CTR, where the scattered amplitudes from successive layers $A(\vec{Q})$ are assumed by a suitable phase factor. If the attenuation of x-rays by the sample is neglected then:

$$F^{CTR} = A(\vec{Q}) \sum_{j=0}^{\infty} e^{i\vec{Q_z} a_3 j} = \frac{A(\vec{Q})}{1 - e^{i\vec{Q_z} a_3}}, \tag{2.5.10}$$

where $A(\vec{Q})$ is the scattering amplitude. Q_z, the momentum transfer along the surface normal can be taken to be:

$$\vec{Q_z} = \frac{2\pi l}{a_3}, \tag{2.5.11}$$

So:

$$F^{CTR} = \frac{A(\vec{Q})}{1 - e^{i2\pi l}}, \tag{2.5.12}$$

The intensity distribution of the CTR is then given by:

$$I^{CTR} = |F^{CTR}|^2 = \frac{|A(\vec{Q})|^2}{1 - e^{i2\pi l}} = \frac{|A(\vec{Q})|^2}{4\sin^2(\pi l)}, \tag{2.5.13}$$

In the kinematic approximation, the total scattered amplitude can be given simply as the phase sum of bulk and surface scattering:

$$F_{hk}^{CTR}(l) = F_{hk}^{bulk}(l) + F_{hk}^{surf}(l), \tag{2.5.14}$$

where $F_{hk}^{surf}(l)$ is the sum of the scattering over the surface unit cell. At integer points, scattering intensity is contributed from both the bulk and surface structure but is dominated by the bulk contribution. Between integer points, the anti-Bragg condition, the region is more sensitive to surface structure as bulk scattering is largely out of phase [20]. In the case where the surface structure is different to the bulk i.e when the surface restructures to minimise free energy or from the adsorption of an overlayer, extra tails of diffuse intensity perpendicular to the surface arise in between the CTRs, termed Fractional Order Rods (FORs). When investigating overlayers/reconstructions, FORs are very useful as they give purely surface information.

2.5.4 Data Analysis

Data analysis was conducted using a modified version of ANA-AVE-ROD written by E. Vlieg [21]. The initial stages of analysis began with using the ANA program to convert the experimentally collected intensities to structure factors by integrating and applying correction factors. Next, AVE is used to average equivalent reflections to give the final data set. This is then imported to ROD where the data are compared to theoretically calculated data for possible models.

2.5.4.1 Data Integration and Correction Factors

Data integration can be done numerically where the background is estimated with approximately 5 points on either side of the peak. However, sometimes a fitting function form eg. Lorentzian or Gaussian is required to fit the peak when the background is difficult to estimate. This is more than often necessary for scans taken at the anti-Bragg positions of a CTR where the intensity is much less reduced. The integrated intensity and its associated error are given by [22]:

$$I_{int} = \sum_{i=1}^{N} S_i - \frac{N_s}{N_B} \sum_{j=1}^{N_B} B_j \tag{2.5.15}$$

$$\sigma_{I_{int}} = \sqrt{\sum_{i=1}^{N} S_i + \left(\frac{N_s}{N_B}\right)^2 \sum_{j=1}^{N_B} B_j} \tag{2.5.16}$$

Where S_i and B_j are the number of counts at each point in the peak and background, respectively. N_s and N_B are the number of points in the peak and background, respectively.

Performing and collecting X-ray data measurements requires the use of a diffractometer. Depending on which type, certain geometrical correction factors have to be applied to the data before any quantitative analysis. In the current work a six-circle diffractometer was used for which the correction factors were calculated by E. Vlieg [21]. Once the data has been integrated (I_{int}) it is necessary to apply these correction factors to convert the data into structure factors using:

$$F_{hkl} = \sqrt{\frac{I_{int}}{PLC_{rod}C_{area}}} \tag{2.5.17}$$

where P is the polarisation factor, L is the Lorentz factor, C_{rod} the correction for rod interception and C_{area} the correction factor for the active area. In the following sections each of the correction factors a briefly described.

2.5.4.2 Polarization Factor

All of the X-ray measurements in this body of work were conducted using synchrotron radiation and so only a horizontally polarized beam will be considered. The observed intensity is related to the sinus of the angle between the polarization direction and the detector:

$$P = \cos^2 \phi \tag{2.5.18}$$

where ϕ is the angle between incident and scattered beams in the horizontal plane. The position of the detector is determined by three angles with the incident beam, the incident angle α, the out-of-plane angle δ and the in-plane angle γ. The polarization factor is then simply expressed as:

$$P = 1 - \sin\alpha \cos\delta \cos\gamma + \sin\delta \cos\alpha^2 \tag{2.5.19}$$

2.5.4.3 Lorentz Factor

As mentioned above, the experimentally observed intensities are integrated to convert to structure factors. This integration takes place in reciprocal space and so take units of reciprocal space (r. l. u or 1/Å). As the measurements from the diffractometer are in real space there is a need to introduce a correction factor, the Lorentz factor, which converts from reciprocal space to units to real space units:

$$L = \frac{1}{\sin\delta \cos\beta_{in} \cos\delta} \tag{2.5.20}$$

2.5.4.4 Rod Interception

The detector resolution, determined by slits, along the rod to be measured changes with different l-positions due to the change of the detector angle δ, with the sample surface. This is implies that the Ewald sphere cuts the rod at different angles and the observed intensities must be corrected for this using the rod interception factor:

$$C_{rod} = \frac{2\cos\beta_{in}\cos\delta}{\cos\alpha\cos(\alpha - 2\beta_{in}) + \sin(2\alpha - 2\beta_{in})\sin\delta + 2\sin(\alpha - \beta_{in})^2\cos\delta\cos\gamma} \tag{2.5.21}$$

2.5.4.5 Active Area

The intensity measured by the detector is a contribution from the active surface area of the sample i.e not all of the surface may contribute. The illuminated or active area is defined by the lateral size of the incoming beam and the detector slit width. This is corrected for by using:

$$C_{area} = \frac{1}{\sin\delta\cos\alpha - \beta_{in}} \tag{2.5.22}$$

2.5.5 Averaging

Each measured intensity can have an associated systematic error due to small misalignments of the diffractometer, measuring different areas of the sample etc. By measuring symmetry equivalent reflections, an estimation of the systematic error can be made using the program AVE. For a set of equivalent reflections AVE calculates the weighted average structure factor (F'_{hkl}), its statistical error (σ') and the standard deviation (s). The agreement factor, ϵ_{hkl} is given by:

$$\epsilon_{hkl} = \frac{s}{F'_{hkl}} \tag{2.5.23}$$

The calculation of the agreement factor excludes poor quality data points, which are identified based upon whether its average is larger than twice its statistical error ($F'_{hkl} > 2\sigma'$) [22]. The average agreement factor over the whole data set is given by:

$$\epsilon' = \frac{1}{M}\sum_{data}\epsilon_{hkl} \tag{2.5.24}$$

Where M is the number of non-equivalent reflections. A value of 10% indicates a good quality data set. The final step that AVE performs is to write the structure factors with their associated errors to a file using:

$$\epsilon^{exp} = \sqrt{(\epsilon')^2(F')^2 + \sigma'} \tag{2.5.25}$$

2.5.6 Structure Determination

As the structure factor is a Fourier transform of the spatial distribution of the electron density, it is very difficult to determine a structure by simply calculating the inverse Fourier transform. This is because only the intensity of a wave can be measured experimentally and thus the complex information (phase) is lost, otherwise known as the missing phase problem. This can be overcome by comparing the experimental structure factors to theoretically calculated structure factors, with the better model giving a better fit to the data.

In the present work, the experimental data were analysed using a version of the program ROD [21] that utilises a least squares refinement procedure. The final goodness-of-fit between experiment and theory is given in terms of two commonly used parameters:

$$\chi^2 = \frac{1}{\sqrt{N-p}} \sum \left(\frac{|F_{hkl}^{calc}|^2 - |F_{hkl}^{exp}|^2}{\sigma_{hkl}} \right)^2, \tag{2.5.26}$$

$$R = \frac{\sum\limits_{hkl} ||F_{hkl}^{exp}| - |F_{hkl}^{calc}||}{\sum\limits_{hkl} |F_{hkl}^{exp}|}, \tag{2.5.27}$$

where N is the number of measured structure factors, p is the number of independent parameters used in the model, F_{hkl}^{calc} are the theoretically calculated structure factors, F_{hkl}^{exp} are the experimentally measured structure factors and σ_{hkl} corresponds to the experimental uncertainties.

A χ^2 value close to 1 indicates a good fit between experiment and theory. The error bars are calculated with a least-squares analysis [21] and corresponds to how much a parameter has to be changed while relaxing all others to cause an increase of χ^2 by a factor of $\frac{1}{N-p}$ from its minimum value [21]. As the χ^2 is very much dependent on the error bars of the experimental data one must take care when comparing different values. The R factor is a value that is independent of the error bars and checks the reflection-by-reflection agreement between the observations and the calculations and constitutes another indicator of the reliability of the model. A value close to 10% is considered a small value that would reinforce the reliability of the trial model [23].

2.5.6.1 β Roughness Parameter

Generally speaking, surface roughness leads to a decrease in diffracted intensity especially seen in the anti-Bragg regions of a CTR and can be expressed as a single roughness factor R_{beta} : $I_{corr} = R_{\beta} \times I_{calc}$. Incorporated within the ROD program is the approximate β roughness model, in which each terrace on a surface, n, has an associated occupancy, β^2. A formula that is often valid for roughness calculation is given by [24]:

$$R_{\beta} = (1-\beta)[(1-\beta)^2 + 4\beta \sin \pi (l - l_{Bragg})/N_{layers}^2 \tag{2.5.28}$$

Where N_{layers} is the number of layers in the unit cell and l_{Bragg} is the l-value for the nearest Bragg peak.

2.5.6.2 Analysis Procedure

Comparison of the experimental data and the theoretically calculated structure factors are performed in the ROD program. The model to be used is built up as a 'fit' file which contains geometric and non-geometric parameters and is displayed in Figure 2.7. This shows a typical fit file with the filename being located on the first line, the second line of the file contains the lattice parameters and angles for the system to be studied. The next set of lines are separated into columns, the most important of which are the atom label (yellow), the assigned geometric parameters in the x-direction (purple), y-direction (blue), and z-direction (orange). The red columns are the relative positions of the associated atom within the unit cell, which are usually the bulk positions. The final two columns represent the occupancy (green) and Debye-Waller factors (pink), respectively. After building up the model it can be read in ROD along with the data file for structural analysis.

The following section will attempt to list several strategies that have been found during the course of this work to ensure an adequate search of the parameter space and that the global minimum of the system has been reached:

1. As a first step, it is important to determine how many unit cells are needed in the out-of-plane direction. If there are too little then large displacements could be seen for atoms located near the bulk. Too many unit cells means unnecessarily adding to the number of parameters and hence increases the χ^2. Adding a unit cell in the out-of-plane direction to the fit file displayed in Figure 2.7 is done by simply adding on the same set of atoms but now adding one to the z-parameter, as shown in Figure 2.8.
2. Approaching the analysis systematically proved the best method overall i.e eliminating simple models and slowly increasing in complexity until a physical structure with the lowest χ^2 is found. This could include beginning with the clean/bulk terminated model, changing initial starting parameters, changing surface termination and adding adsorbates.
3. In this thesis, systems were investigated that required the addition and testing of adsorbates on particular surface sites. A key parameter to determine whether any particular surface atom is bonded to an adsorbate is the occupancy and its associated error. A method that generally worked was to add an adsorbate to the fit file that is bonded to a certain surface atom with 100% occupancy. After allowing all atoms in the model to displace, the occupancy parameter was then fitted and the value would give a good indication whether that particular site is occupied with the adsorbate atom.
4. On occasion, it is necessary to induce partial occupancies to surface atoms. This can sometimes lead to unphysical displacements and can be prevented with careful application of upper and lower limits to the displacement parameters forcing the optimisation of the structure.
5. Optimisation of parameters generally began with the scaling and roughness parameters. After which the z-displacements of all atoms would be optimised, followed by the x or y-displacements. It maybe necessary to optimise the parameters in different orders e.g. optimising the displacements nearest the surface first or individual parameters one at a time. The latter was generally avoided as it could increase the probability of finding a local minima however it can provide information regarding which parameters have more of an affect on reducing the χ^2.

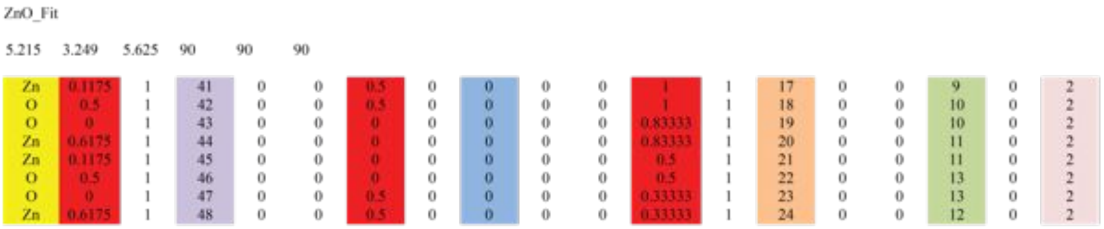

ZnO_Fit

5.215 3.249 5.625 90 90 90

Zn	0.1175	1	41	0	0	0.5	0	0	0	0	1	1	17	0	0	9	0	2
O	0.5	1	42	0	0	0.5	0	0	0	0	1	1	18	0	0	10	0	2
O	0	1	43	0	0	0	0	0	0	0	0.83333	1	19	0	0	10	0	2
Zn	0.6175	1	44	0	0	0	0	0	0	0	0.83333	1	20	0	0	11	0	2
Zn	0.1175	1	45	0	0	0	0	0	0	0	0.5	1	21	0	0	11	0	2
O	0.5	1	46	0	0	0	0	0	0	0	0.5	1	22	0	0	13	0	2
O	0	1	47	0	0	0.5	0	0	0	0	0.33333	1	23	0	0	13	0	2
Zn	0.6175	1	48	0	0	0.5	0	0	0	0	0.33333	1	24	0	0	12	0	2

Figure 2.7: A fit file representing the model to be analysed. The most important parameters are highlighted where those in yellow are the atom labels, purple are the parameters assigned to the x-displacement of the atom, blue are the parameters assigned to the y-displacement of the atom and orange are the parameters assigned to the z-displacement of the atom. The columns highlighted in red are the relative positions of the atom within the unit cell. Green highlighted parameters are the occupancies and the pink highlighted parameters are the Debye-Waller factors.

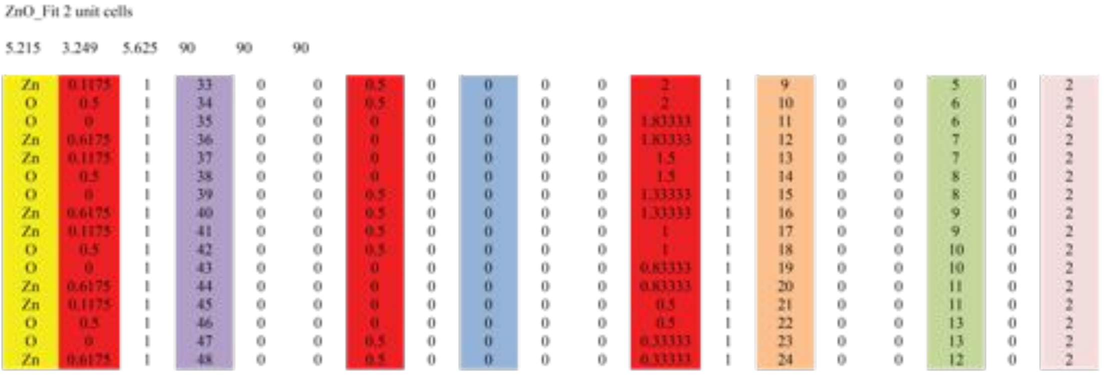

ZnO_Fit 2 unit cells

5.215 3.249 5.625 90 90 90

Zn	0.1175	1	33	0	0	0.5	0	0	0	0	2	1	9	0	0	5	0	2
O	0.5	1	34	0	0	0.5	0	0	0	0	2	1	10	0	0	6	0	2
O	0	1	35	0	0	0	0	0	0	0	1.83333	1	11	0	0	6	0	2
Zn	0.6175	1	36	0	0	0	0	0	0	0	1.83333	1	12	0	0	7	0	2
Zn	0.1175	1	37	0	0	0	0	0	0	0	1.5	1	13	0	0	7	0	2
O	0.5	1	38	0	0	0	0	0	0	0	1.5	1	14	0	0	8	0	2
O	0	1	39	0	0	0.5	0	0	0	0	1.33333	1	15	0	0	8	0	2
Zn	0.6175	1	40	0	0	0.5	0	0	0	0	1.33333	1	16	0	0	9	0	2
Zn	0.1175	1	41	0	0	0.5	0	0	0	0	1	1	17	0	0	9	0	2
O	0.5	1	42	0	0	0.5	0	0	0	0	1	1	18	0	0	10	0	2
O	0	1	43	0	0	0	0	0	0	0	0.83333	1	19	0	0	10	0	2
Zn	0.6175	1	44	0	0	0	0	0	0	0	0.83333	1	20	0	0	11	0	2
Zn	0.1175	1	45	0	0	0	0	0	0	0	0.5	1	21	0	0	11	0	2
O	0.5	1	46	0	0	0	0	0	0	0	0.5	1	22	0	0	13	0	2
O	0	1	47	0	0	0.5	0	0	0	0	0.33333	1	23	0	0	13	0	2
Zn	0.6175	1	48	0	0	0.5	0	0	0	0	0.33333	1	24	0	0	12	0	2

Figure 2.8: A fit file representing the model to be analysed with an additional unit cell from Figure 2.7. The colour scheme is that same as Figure 2.7.

References

[1] G. Attard, C. Barnes, Surfaces (Oxford Chemistry Primers, 2004)

[2] G. Binnig, H. Rohrer, C. Gerber, E. Weibel, Appl. Phys. Lett., 40, 178, (1982)

[3] G. Binnig, H. Rohrer, C. Gerber, E. Weibel, Phys. Rev. Lett., 49, 57, (1982)

[4] U. Diebold, Surf. Sci. Rep., 48, 53, (2003)

[5] C. Woll, Prog. Surf. Sci., 82, 55-120, (2007)

[6] J. Tersoff, D. Hamann, Phys. Rev. Lett., 50, 25, (1983)

[7] J. Tersoff, D. Hamann, Phys. Rev. B., 31, 805, (1985)

[8] C. J. Chen, Phys. Rev. Lett., 64, 448, (1990)

[9] N. D. Lang, Phys. Rev. Lett., 55, 230, (1985)

[10] N. D. Lang, Phys. Rev. Lett., 56, 1164, (1986)

[11] A. Davisson, H. Gerner, Phys. Rep., 30, 705, (1927)

[12] G. Attard and C. Barnes Surfaces, Oxford Chemistry Primer No. 59 (1998) (Oxford Science Publications)

[13] D. P. Woodruff and T.A. Delchar, Modern Techniques of Surface Science, (2001) (OUP)

[14] P. Eisenberger, W. C. Marra, Phys. Rev. Lett., 46, 1081, (1981)

[15] W. C. Marra, P. Eisenberger, A. Y. Cho, J. Appl. Phys., 50, 6927, (1979)

[16] J. Als-Nielsen, D. McMorrow, Elements of Modern X-ray Physics, Wiley, (2001)

[17] B. E. Warren, X-ray Diffraction, Dover Publications, Inc. (1990)

[18] I. K. Robinson, Acta. Cryst, A54, 772, (1998)

[19] I. K. Robinson, D. J. Tweet, Rep. Prog. Phys., 55, 599, (1992)

[20] D. B. Howes, The Formation of Gold - semiconductor Interfaces Determined by SXRD, PhD Thesis, University of Leicester, (1993)

[21] E. Vlieg, J. App Crys., 33, 401, (2000)

[22] I. K. Robinson, Handbook of Synchrotron Radiation (North Holland, Amsterdam, 1991) Vol. 3.

[23] R. Feidenhansl, Surf. Sci. Rep., 10, 105, (1989)

[24] I. K. Robinson, Phys. Rev. B., 33, 3830 - 3836 (1986)

Chapter 3

Instrumentation

The experimental surface scientist is ever looking for ways to improve the accuracy and reliability of data collection and perhaps the limiting factor is the instrumentation employed. This is especially the case for the advanced techniques and systems theoretically described in Chapter 2. This chapter discusses the practical aspects of their use and will begin with describing the Ultra High Vacuum (UHV) systems used. Focus will primarily be given to the Scanning Probe Microscopes (SPM) and components of Beamline ID32 of the European Synchrotron Radiation facility (ESRF). However other surface characterisation techniques, such as LEED and AES, will also be discussed as well as the instrumentation used to perform certain aspects of the investigations described in later chapters.

3.1 UHV Systems

The three UHV systems used in this work are displayed in Figures 3.1, 3.2 and 3.3 which are named the variable temperature STM (VT-STM), combined atomic force microscope and STM (AFM-STM) and R2P2, respectively. All the systems employ many similar parts however the designs are very different; the systems in Figures 3.1 and 3.2 are composed of two main UHV chambers, the analysis chamber which houses the LEED/AES optics as well as the STM stage, and the preparation chamber, which contains sample preparation facilities such as an ion gun. In these particular systems a manual gate valve is placed between the two chambers in order to facilitate the higher pressures needed for sample preparation without contaminating the analysis chamber (see Figures 3.4 and 3.5 for a schematic representation). The system in Figure 3.3 is a multi-component UHV system which consists of one main chamber, called the R2P2, containing a manipulator transfer arm in order to access the various smaller chambers attached for sample preparation (preparation chamber), storage (storage carousel) and characterisation (LEED/AES and STM chambers). Each chamber is separated by a manual gate valve to ensure minimal contamination of the R2P2 which has a base pressure in the 10^{-10} mbar range (see Figure 3.6 for a schematic representation).

In order to obtain and maintain UHV, a combination of pumps are used. These include rotary pumps which are first used to bring the pressure from atmosphere (1013.25 mbar) to $\sim10^{-2}$ mbar region and serve as a backing for turbo molecular pumps that can handle the high gas loads and further bring the pressure down to $\sim10^{-8}$ mbar region. This is particularly useful in

Figure 3.1: Omicron UHV VT-STM.

the preparation chambers where a significant volume of gas (typically argon) after preparation needs removing. To achieve UHV pressures it is necessary to 'bake' the system by heating to ∼400K for ∼24 hours to remove gas molecules, the most abundant within the residual are usually water molecules and hydrocarbons such as CO, which are desorbed from the inner walls of the chamber. After the bake, UHV pressure is routinely achieved via the use of ion pumps and titanium sublimation pumps (TSP).

Very useful for any vacuum system is the load lock. This allows the transfer of samples or STM tips in the chamber without breaking UHV conditions in the main chambers as it is isolated via a gate valve and equipped with a turbo molecular pump. A gas line system is attached to the

Figure 3.2: Omicron UHV AFM-STM system.

preparation chambers of each system to allow the introduction of gases via a high precision leak valve. It is extremely important to be able to measure the pressure within the system. For high pressures, Pirani gauges are used, allowing measurements from atmosphere (1013.25 mbar) to $\sim 10^{-2}$ mbar. Lower gas pressures are measured by a hot or cold cathode ion gauge allowing measurements down to 10^{-11}. A schematic view of the VT-STM, AFM-STM and R2P2 are shown in Figures 3.4, 3.5 and 3.6, illustrating the various components described above.

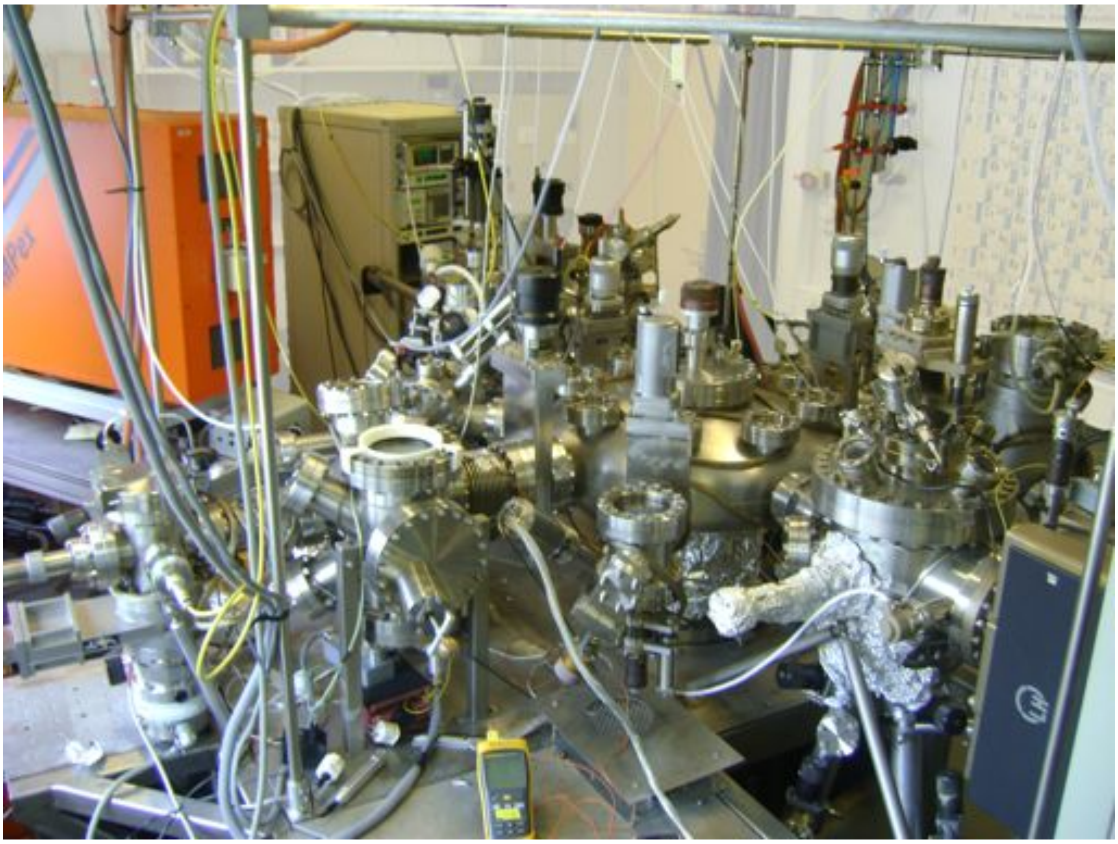

Figure 3.3: Multi-component Omicron R2P2 UHV system.

3.2 STM

All experiments conducted in this work (See Chapter 4 onwards) were carried out using STM's attached to the UHV systems described above. The usual approach was to use the Omicron UHV VT-STM and Omicron UHV AFM-STM to characterise a sample before it would be taken to the ESRF, where further preparation and characterisation are done using the multi-component R2P2 system. Measurements were then made with X-rays. All microscopes are capable of regularly achieving atomic resolution at room temperature.

The VT-STM and R2P2 have similar methods during scanning mode; when approaching the tip to the sample it is the sample that is in a fixed position and the tip is moved whereas for the AFM-STM the sample is approached to the tip. In order for correct positioning the tip/sample is mounted on a piezoelectric crystal which changes length as a result of applying an electric field.

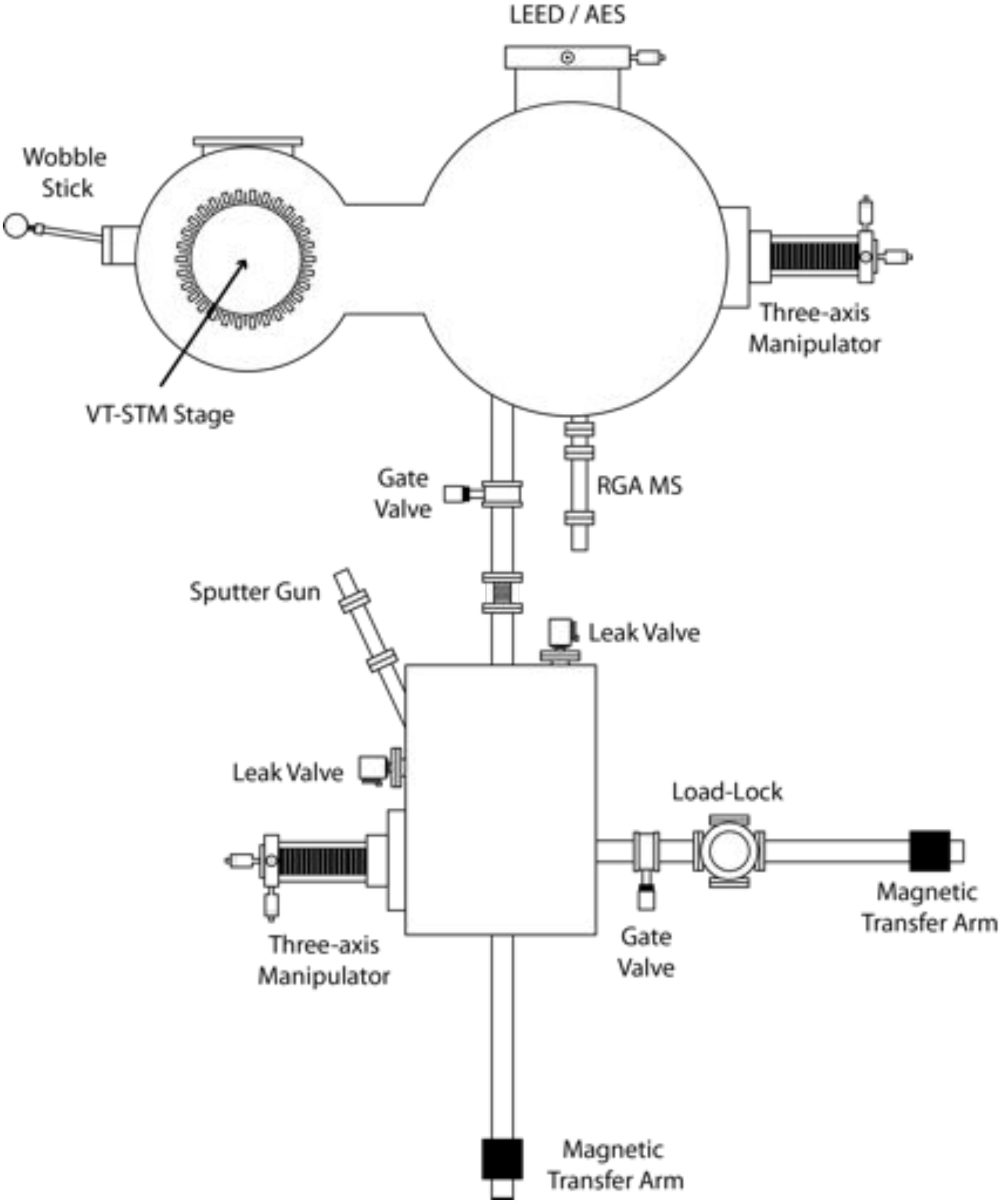

Figure 3.4: Schematic view of VT-STM UHV system.

This allows motion in the z-direction (i.e towards/away from the tip/sample) on the millimetre scale. Usually, two separate piezoelectric tubes are mounted to allow movement in the x and y

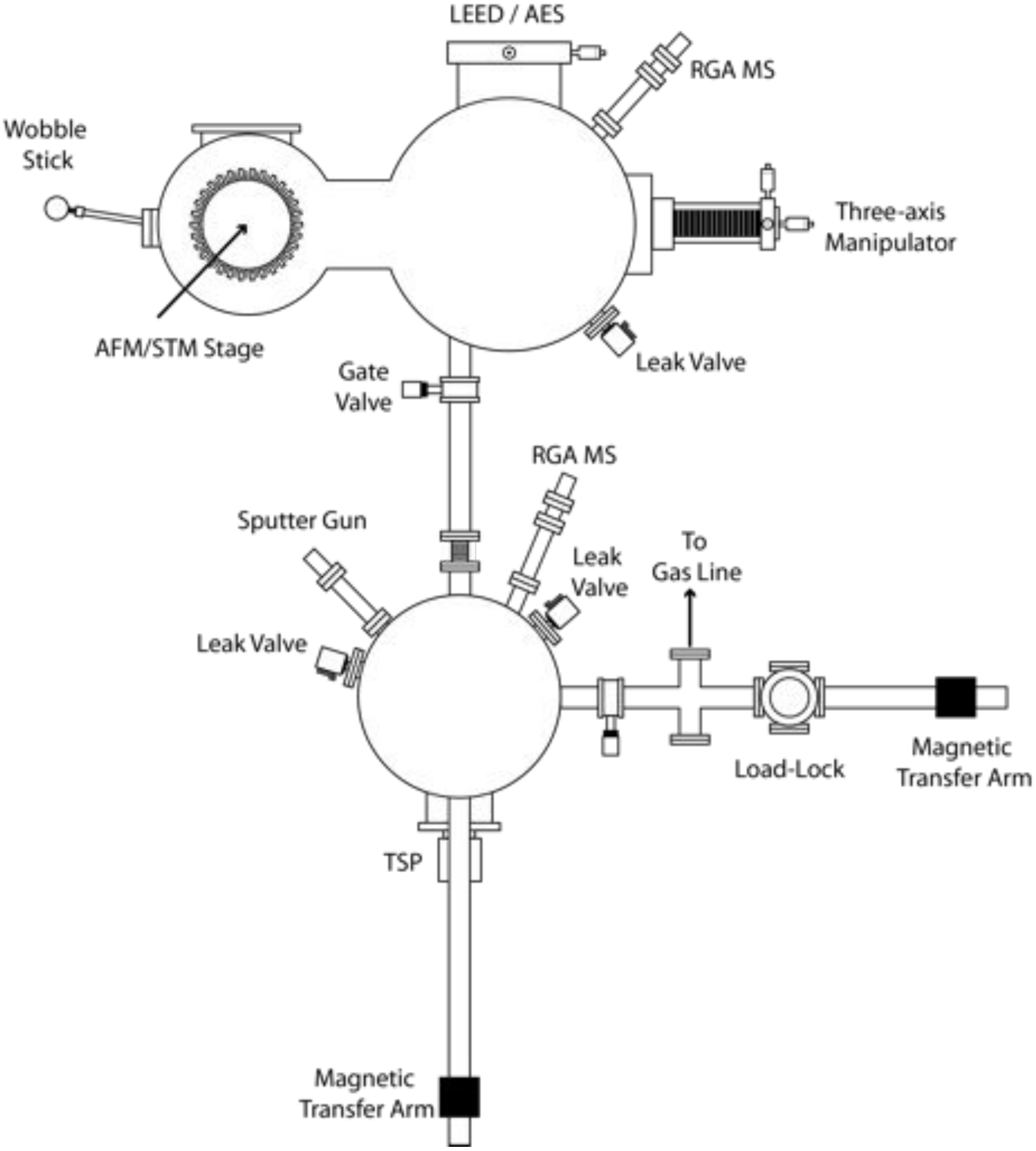

Figure 3.5: Schematic view of AFM-STM UHV system.

directions however the VT-STM is a single tube scanner. A scan is achieved by rastering the tip across the sample.

It is essential for atomic resolution that a carefully designed mechanical isolation system is employed to reduce the effects of vibrations and thermal drift. The biggest difference between

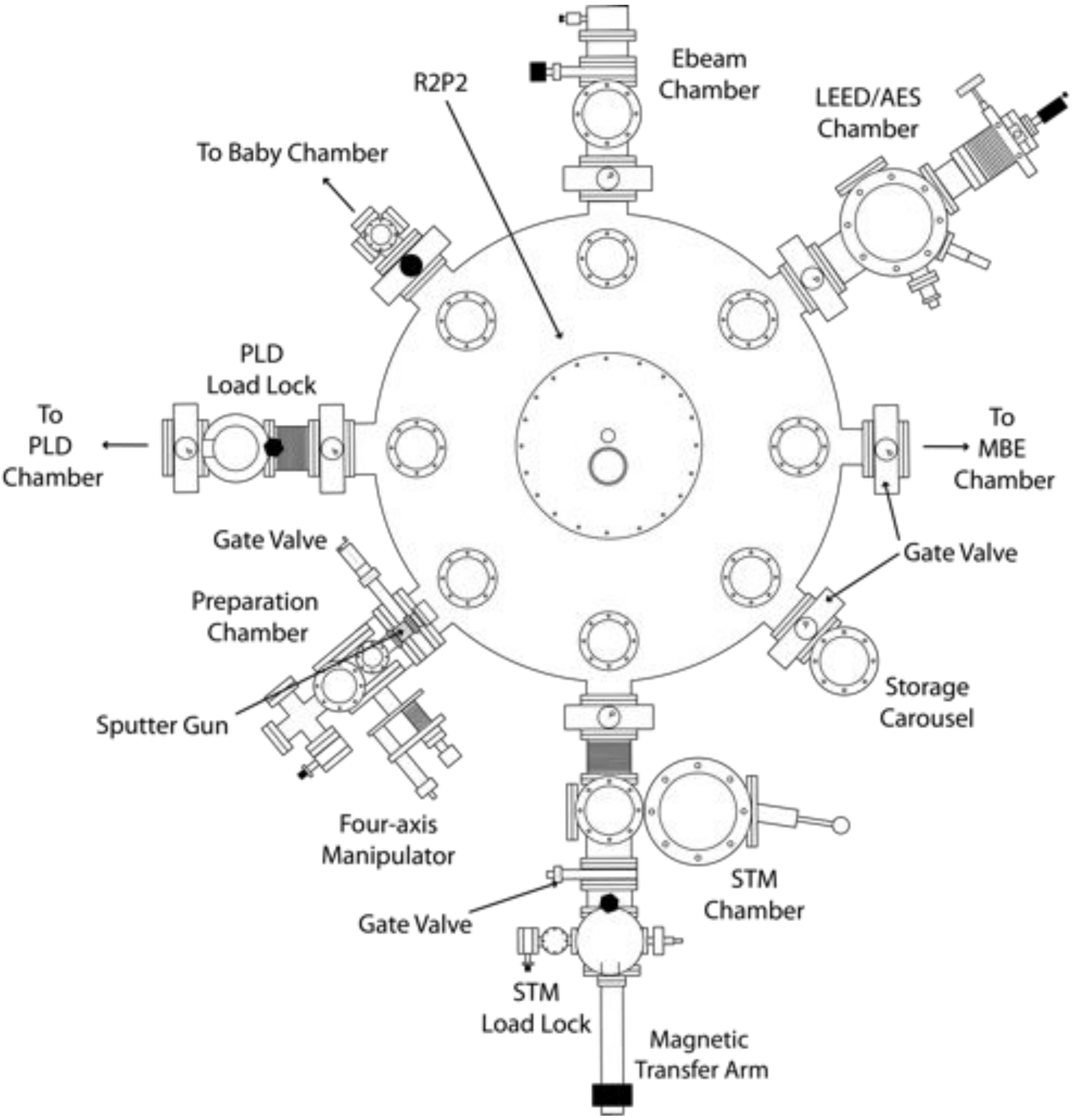

Figure 3.6: Schematic view of R2P2 UHV system.

the UHV systems located in UCL, London (VT-STM and AFM-STM) and the ESRF (R2P2) is the vibrational damping apparatus. The VT-STM and AFM-STM isolates only the STM stage whereas the R2P2 isolates the entire table. During scanning mode the VT-STM and AFM-STM stages are suspended by vertical springs and an eddy damping system, which consists of copper fins and permanent magnets. These were used to reduce vibrational noise. The R2P2, on the other hand, uses four 'legs' to provide pneumatic vibration suspension isolating the entire table from the floor. Furthermore, other sources of vibrational noise (i.e Turbo molecular pumps, backing pumps, cooling fans etc...) must be located and turned off to ensure atomic resolution.

3.2.1 STM Modes

STM images are acquired by scanning an atomically sharp tip across a conducting or semiconducting surface whilst recording a signal which allows its use as a probe of the surface structure. There are two common modes of operating the STM, constant current mode and constant height mode. In constant height mode the tip-surface separation is kept constant during scanning and the image is formed by the variation in the tunnelling current. This method allows for very fast accumulation of images however is limited to use on atomically flat surfaces as there is a high probability of the tip crashing into the surface. In constant current mode (Figure 3.7), the method mainly used in this work, a feedback circuit is used to adjust the tip-surface separation to keep the tunnelling current constant and now the voltage applied to the z-piezo is recorded.

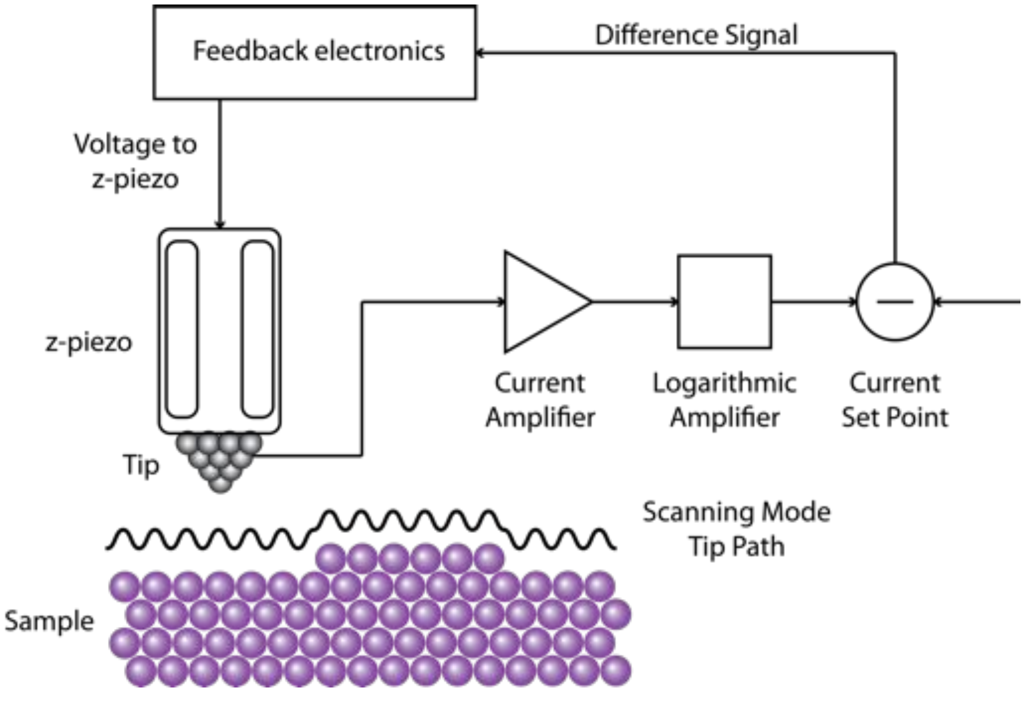

Figure 3.7: Schematic illustration of the STM feedback mechanism in constant current mode.

3.2.2 Tip Fabrication

As mentioned above, a necessary requirement for atomically resolved STM imaging is the use of an atomically sharp tip. A number of methods have been reported [1, 2] and in the present work, tips were fabricated via electrochemical etching of a tungsten wire. This is illustrated in Figure 3.8. The tungsten wire of varying thickness (0.25 mm - 0.38 mm) is suspended such that it is partially immersed in a 2 M solution of NaOH. By attaching a power supply to a metal ring, which acts as the cathode and the tip acts as the anode with the NaOH as the electrolyte, etching of the tip occurs at the air-electrolyte interface. When partially immersed, a neck is formed where eventually the immersed portion will drop off, producing a sharp tip. Tip quality is checked with an optical microscope after which it is thoroughly rinsed with ultra pure water and then placed into the UHV system via the load lock. The tip then undergoes a degassing stage where it is annealed to approximately 450 K to ensure removal of any adsorbates/contaminants.

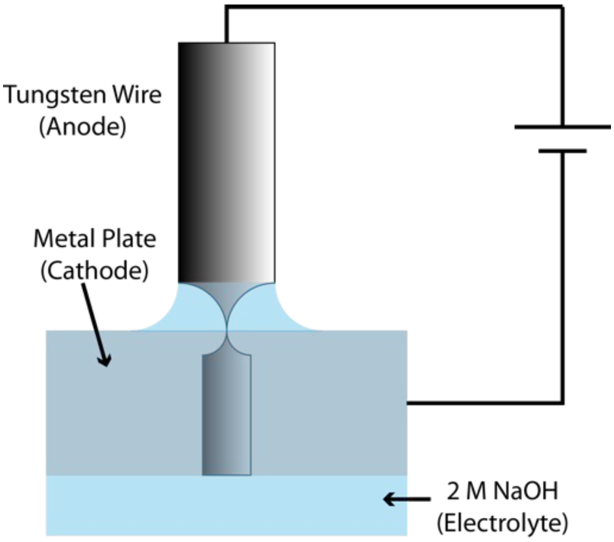

Figure 3.8: Illustration of the electrochemical tip etching instrumentation.

3.3 Surface Preparation

3.3.1 Argon Ion Bombardment

In the present work, adsorbates or surface contamination are removed by sputtering. The method employed utilises an ion gun that generates a beam of electrons ionising an inert gas (Argon), which has been leaked into the chamber, typically at a partial pressure in the 10^{-5} mbar region (See Figures 3.4, 3.5 and 3.6). This beam of ions, incident at 45°to the sample surface with an energy range between 500 - 1500 eV, has enough energy to remove surface atoms and thus creating an unwanted rough surface. Another unwanted outcome of this method is the embedding of Argon ions, in order to remove these and flatten the surface the sample is annealed at high temperatures in UHV or in an oxygen atmosphere.

3.3.2 Sample Annealing and Manipulation

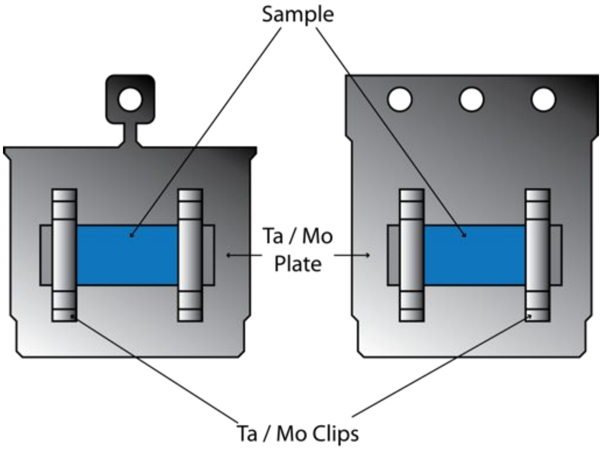

Figure 3.9: Illustration of the sample plates used in (a) the VT-STM and AFM-STM UHV systems and (b) the R2P2 UHV system.

Figure 3.9 shows the different sample plates used for (a) the VT-STM and AFM-STM UHV systems and (b) the R2P2 UHV system. Samples were attached to tantalum or molybdenum plates via spot-welding tantalum or molybdenum clips on either side. An important point to note is that each sample had purposely created steps on the sides where mounting would take place to ensure that the sample surface was at the highest point, avoiding shadowing effects during

X-ray measurements. Once mounted, the sample would be introduced into the systems and manipulated via the magnetic transfer arms, as shown in Figures 3.4, 3.5 and 3.6. Each chamber equipped with a sample manipulator allows the sample to be moved in all three axis as well as rotated 360°. In Figures 3.4 and 3.5, each manipulator can be used to heat the sample via electron bombardment up to approximately 1500 K. For the chamber shown in Figure 3.6, the sample must be manipulated to the Sputter Chamber and the Ebeam Chamber for UHV annealing or the PLD Chamber for annealing in an oxygen atmosphere. This method of heating involves passing a current through a tungsten filament, which then emits electrons that accelerate towards the back of the sample plate, which is held under positive bias. The temperature is monitored with a thermocouple and an infrared pyrometer.

3.4 Preliminary Characterisation

3.4.1 Low Energy Electron Diffraction (LEED)

In the present work, LEED is used to gain qualitative information only i.e the two-dimensional periodicity of the surface unit cell and any variations of the unit cell due to adsorbates. Prior to any investigation with STM, LEED would be used to obtain sharp, intense diffraction spots with a low background to ensure a well ordered clean surface. In the LEED system, used in all UHV systems and schematically shown in Figure 3.10, a monochromatic beam of electrons are generated by an electron gun, whose energy can be varied (typically between 0 - 1000eV). To avoid charging problems, the beam is incident upon an earthed sample where electrons undergo diffraction and those that are backscattered from the periodic surface travel towards a series of grids (G1 - G4). The outer grids (G1 and G4) are earthed to ensure the electrons travel in a field free region. The inner pair of grids (G2 and G3) serve as a filter, which are held at a negative potential ($-E_p + \triangle V$), where $\triangle V$ is typically between 0 - 10V, to ensure only elastically scattered electrons reach the phosphor screen (S). S is biased at a high positive voltage ($\sim$6 keV) to accelerate the transmitted electrons towards the phosphor screen with enough energy to cause light emission. A pattern consisting of bright spots on a dark background arises, which reflect the symmetry and crystalline order of the surface.

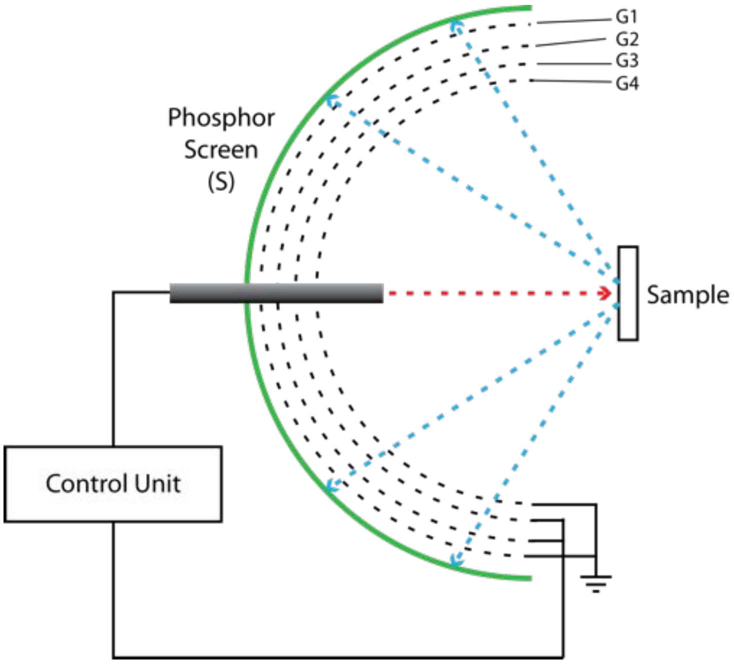

Figure 3.10: Schematic representation of the LEED optics

3.4.2 Auger Electron Spectroscopy (AES)

AES is a widely used technique to examine the cleanliness of surfaces. In all three UHV systems used in this work, the LEED optics were used in retarding field analyser (RFA) mode to perform AES. The inner pair of grids (G2 and G3) serve as a high-pass filter, which are held at a negative potential, the screen acts as a current collector and a lock-in amplifier is used to retrieve the Auger spectra.

3.5 Surface X-ray Diffraction (SXRD)

All of the Surface X-ray Diffraction (SXRD) experiments (Chapters 4, 5 and 6) conducted in this work were carried out at the ID32 Beamline in the European Synchrotron Radiation Facility (ESRF). The following sections will begin with a description of the beamline and its components, highlighting the need for such high precision instrumentation when dealing with fundamental surface science. Later, details will be given about the baby chamber, a portable ion-pumped UHV chamber which acts as a transfer from the off-line UHV laboratory (Figure 3.6) to the beamline. It is installed on the six-circle diffractometer for X-ray measurements. Two different baby chambers were used in this work. Lastly, a brief description of the detector used and data collection methods will be discussed.

3.5.1 Beamline ID32

The ID32 Beamline, a beamline dedicated to investigations for surface and interface studies, is capable of supporting several X-ray based techniques including SXRD, Hard X-ray Photoelectron Spectroscopy (HaXPES), Extended X-ray Absorption Fine Structure (EXAFS) and X-ray Standing Waves (XSW). The setup includes two optical hutches and two experimental hutches however in the current work only one experiment hutch is used. Interested readers of the finer details of this experimental hutch and the whole beamline are referred to Ref [3], a recent detailed review of the setup of the beamline. A schematic representation of the beamline is shown in Figure 3.11.

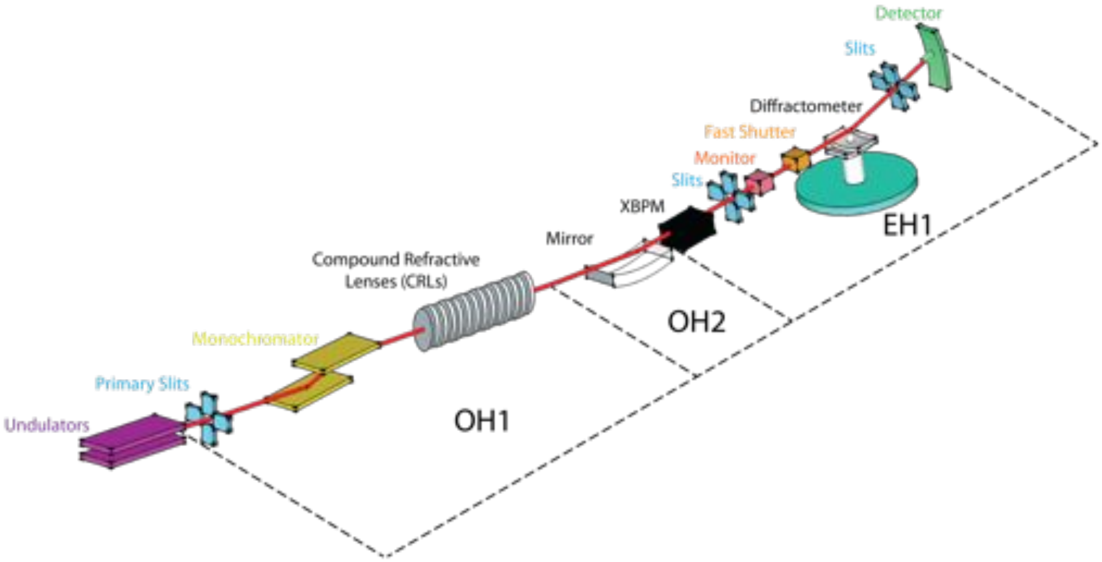

Figure 3.11: Schematic representation of the ID32 Beamline as used in this work.

To create the intense radiation, two undulators are situated in the Storage Ring (SR) which help achieve a maximum photon flux of about $\sim 10^{15}$ $photons\ s^{-1}\ mm^{-2}$ at 20 keV (bandwidth 0.1%). The x-ray beam travels under UHV throughout the entire beamline to the sample located in Experimental Hutch 1 (EH1). From the undulators a white beam is created which passes through a monochromator located in Optics Hutch 1 (OH1). The monochromator consists of a pair of perfect Si(111) crystals which are liquid N_2 cooled to counter the high heat load transferred from the white beam. The monochromatic beam then passes a set of up to 15 two dimensional parabolic beryllium compound refractive lenses (CRL) allowing focussing of the beam. Located in Optics Hutch 2 (OH2) is an x-ray mirror coated with SiO_2, Ni and Pd stripes which act as a low pass filter for higher harmonics transmitted by the monochromator. An important apparatus installed in EH1 is the X-ray Beam Positioning Monitor (XBPM) which helps avoid beam drift from the thermal load of the optics by a feedback loop connected with the monochromator's vertical and horizontal angle piezos. Horizontal (Hg) and Vertical (Vg) slits are used to define the width and angular divergence of the beam incident on the sample. In between the slits are located a monitor, which allows the measurement of the incident intensity, and a fast shutter that facilitates the blocking of the beam during times when measurements are not being taken. The former is useful as it allows the diffracted intensity collected by the detector to be normalised and the latter is perhaps more useful as it not only protects the detector but also reduces any possible beam damage of the sample. In the present work an X-ray beam of 17.7 keV ($\lambda = 0.7$ Å) was used which was focused with all 15 CRLs using the Pd coated mirror. A Hg slit size of 300 μm and a Vg slit size of 20 μm ensured there was enough intensity and the sample was illuminated fully with the beam which was incident at a fixed angle of 0.3°.

3.5.2 Six Circle Diffractometer

The experiments conducted in this work utilised a computer controlled (SPEC [4]) six-circle diffractometer with an attached HUBER tower located in EH1. A schematic representation of the six degrees of freedom used on the diffractometer as well as the motors used on the HUBER tower are illustrated in Figure 3.12.

As mentioned above, the incidence angle of the X-ray beam was fixed at 0.3°. This is achieved using the α circle to tilt the entire diffractometer. Sample alignment is achieved by using the χ, ϕ and θ circles which align the beam to the surface normal. Care must be taken so that the incidence angle remains the same when θ is rotated, in order to ensure the sample normal is always perpendicular to the incident beam the ϕ and χ circles are optimised for different angles of θ. Circles δ and γ are for positioning the detector in and out-of-plane, respectively. Additional degrees of freedom for sample alignment are provided by the HUBER tower allowing the sample to be positioned in the x (trx), y (try) and z (try) directions with respect to the beam.

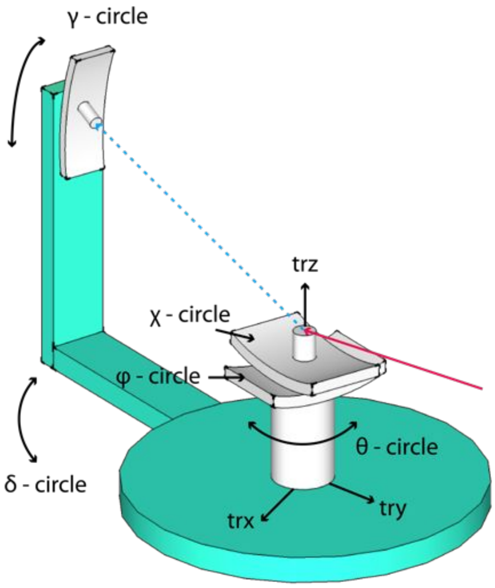

Figure 3.12: Schematic representation of the six-circle diffractometer used in this work.

3.5.3 Baby Chamber

A 'baby' chamber is a portable UHV chamber pumped by a battery powered ion pump. It allows the safe transfer of a UHV prepared sample from the off-line R2P2 system (See Figure 3.6) to the six-circle diffractometer, where it is mounted via a bracket on the HUBER tower. Once mounted the sample can be aligned as described above and measurements of the as-prepared surface can be taken. This is only possible with the use of a beryllium X-ray window which allows the incident X-ray beam to penetrate with little absorption losses. ID32 housed two different types of 'baby' chamber; dome and cylindrical shaped.

3.5.3.1 Dome Shaped

Figure 3.13 displays a photograph of the dome shaped baby chamber attached to the R2P2 UHV system. The chamber consists of a CF38 cross piece in which the sample is housed. The front port of this cross piece has attached a hand valve which is connected to the R2P2 system. After transferring the sample in the baby chamber the valve can be closed to maintain UHV and then transferred to the beamline. On the left hand port is the battery powered ion pump and on the right hand port is a precision leak valve, which for this particular work was used to leak ultra

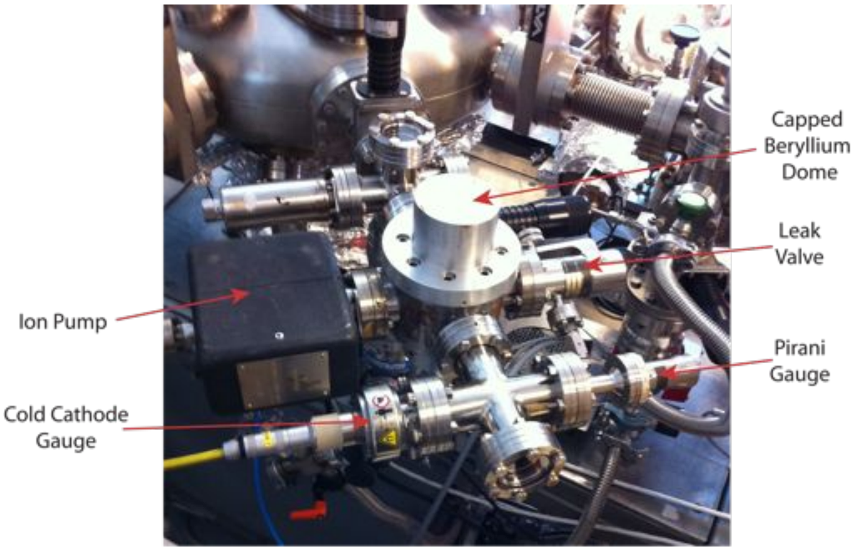

Figure 3.13: A photograph of the dome shaped baby chamber attached to the R2P2 UHV system.

pure water into the chamber. Lastly, another CF38 cross piece is attached to the back port which itself has two vacuum gauges connected, a cold cathode and Pirani gauge located on the left and right ports respectively. The only degree of freedom the sample stage has within the first cross piece is in the z-direction via the use of a butterfly corkscrew attached on the underside. Care must be taken to attach the baby chamber level with the R2P2 system otherwise difficulties may arise during sample transfer. This particular setup was used for the experiments presented in Chapters 4 and 5.

3.5.3.2 Cylindrical Shaped - Electrochemical Droplet Cell (EDC)

The principle behind the cylindrical baby chamber is the same as the dome shaped baby chamber. However, it has been designed specifically to perform electrochemical experiments. Through the top CF38 port an electrochemical droplet cell (EDC) can be attached to perform in-situ electrochemical experiments without exposing the sample/electrolyte interface to ambient air, see Figure 3.14. Details pertaining to the design and use are given in Ref [5]. In the present work, the EDC comprised of a $\sim$ 20 cm long glass capillary tube with a diameter of $\sim$ 2 mm connected to a glass cross piece. Figure 3.15 illustrates the setup of the EDC together with the cylindrical baby chamber. Inlet and outlet tubes, made of PTFE, were connected to the left and right ports of the glass cross piece, respectively. The inlet tube is fed through the glass

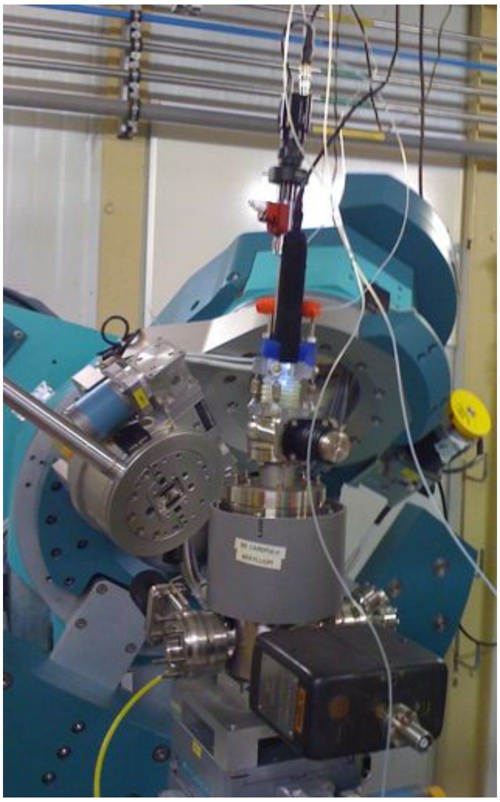

Figure 3.14: A photograph of the electrochemical droplet cell installed on the diffractometer.

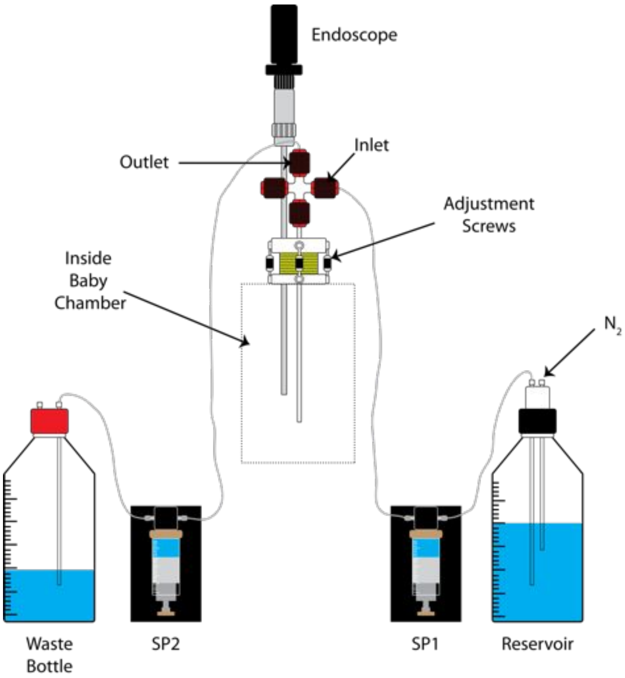

Figure 3.15: An illustration showing the setup of the electrochemical droplet cell used in this work.

capillary, leaving a gap of ~ 2 mm from the end, which allowed a small droplet to be created and thus creating a meniscus with the sample surface. The inlet and outlet tubes are connected to a computer controlled syringe pumping system, where the syringe pump 1 (SP1) draws ultra pure deaerated water from the reservoir and pumps it into the inlet tube. Syringe pump 2 (SP2) is used to empty the capillary tube and glass cross piece and then depositing the unwanted liquid into a waste bottle. During the experiment the position of the capillary tube and water droplet are monitored with an endoscope. A photograph of the $TiO_2(110)$ surface in contact with ultra pure water is shown in Figure 3.16. Fine adjustment of the apparatus is done via adjustment screws connected to the bellow which allow movement in the x, y and z directions.

Figure 3.16: A photograph showing the contact of ultra pure water with the $TiO_2(110)$ surface.

3.5.4 X-ray Detector

In the present work the diffracted intensity was measured with a Cyberstar scintillation detector, which comprises a standard NaI scintillator head, placed $\sim$ 1 m away from the sample. Attached to the detector is a flight tube, having an aperture size of 1×5 mm^2 at the front end, which reduces diffuse scattering that can contribute the background intensity. To determine the detector resolution a pair of horizontal and vertical slits are placed directly in front and can have a range of 0.5 mm to 5 mm in aperture size. The experiments detailed in later chapters use a 2 mm×2 mm aperture size. An analyser crystal, made of graphite, is positioned before the detector to eradicate fluorescent X-rays emitted from the sample.

3.5.5 Data Collection

Two types of scans in reciprocal space were used to collect data; a θ scan and an L scan. In a θ scan the geometry of the apparatus is such that the detector is fixed at a certain l value and the sample is rotated via the θ motor, hence the name θ scan. As the rods are continuous in the out-of-plane direction, the scan will only measure a portion of the rod as determined by the slits in front of the detector. After measuring this portion, the detector is then moved into a higher l value, which is given in reciprocal lattice units (r.l.u), and θ is rotated once more. For this work, the highest l value achieved was 7. An L scan, although much quicker is less accurate as the detector moves along l for a particular rod as the θ motor is rotated.

References

[1] Z. Q. Yu, C. M. Wang, Y. Du, S. Thevuthasan, I. Lyubinetsky, Ultramicroscopy., 108, 873, (2008)

[2] C. Zhang, B. Gao, L. G. Chen, Q. S. Meng, H. Yang, R. Zhang, X. Tao, H. Y. Gao, Y. Liao, Z. C. Dong, Rev. Sci. Instrum., 82, 083101, (2011)

[3] J. Zegenhagen, B. Detlefs, T. L. Lee, S. Thiess, H. Isern, L. Petit, L. Andre, J. Roy, Y. Mi, I. Jourmard., J. Electron Spectrosc. Relat. Phenom., 178, 258, (2010)

[4] G. Swislow, CSS Certified Scientific Software, SPEC X-Ray Diffraction Software and Documentation, Cambridge, MA 02139, USA.

[5] F. U. Renner, Y. Grunder, J. Zegenhagen, Rev. Sci. Instrum., 78, 033903, (2007)

Chapter 4

An Investigation of the H_2O / $TiO_2(110)$ interface using SXRD

4.1 Introduction

Ever since Fujishima and Honda‘s discovery in 1972 that titania (TiO_2) splits water into hydrogen and oxygen in a photoelectrochemical cell [1], there has been tremendous interest in the interaction of H_2O with TiO_2. Effort to gain atomic scale insight into this system has been dominated by studies involving the single crystal rutile TiO_2(110)(1 x 1) surface [2] (see Figure 4.1 for a ball and stick model). This work has resulted in significant breakthroughs in understanding, including the elucidation of the role of oxygen vacancies in substrate induced dissociation of H_2O [3–11]. To date, however, almost all experimental data have been acquired following exposure of TiO_2(110)(1 x 1) to H_2O in near ultra high vacuum (UHV) conditions. Further studies are required to explore the nanoscale details of the TiO_2(110)(1 x 1)-H_2O interface under more technologically pertinent conditions.

SXRD data have recently been acquired from the TiO_2(110)-$H_2O_{(l)}$ interface by Zhang *et al* [12]. Briefly, they conclude that a simple (1 x 1) surface termination is maintained in the presence of $H_2O_{(l)}$, with a mixture of OH and H_2O species bound to the 5-fold coordinated surface titanium. They also detect the presence of a hydration layer. Notably, however, surface preparation for this work was not conducted in ultra high vacuum (UHV), but instead consisted of wet chemical treatments. Furthermore, no surface characterisation was undertaken prior to exposure to $H_2O_{(l)}$ and the potential for significant contamination is high. As a consequence, this approach and the ensuing structural conclusions are potentially questionable. Here, to negate such concern, we rigorously prepare and characterise the TiO_2(110) surface in UHV before exposing to water vapour or immersion in $H_2O_{(l)}$.

To this end, we have quantitatively determined the interfacial geometry of TiO_2(110)(1 x 1) using surface X-ray diffraction (SXRD). The surface immersed in liquid phase water ($H_2O_{(l)}$) has been studied as well as that exposed to water vapour pressures ($H_2O_{(g)}$) ranging from 10^{-6} to 10 mbar. Ancillary measurements were made using scanning tunnelling microscopy (STM).

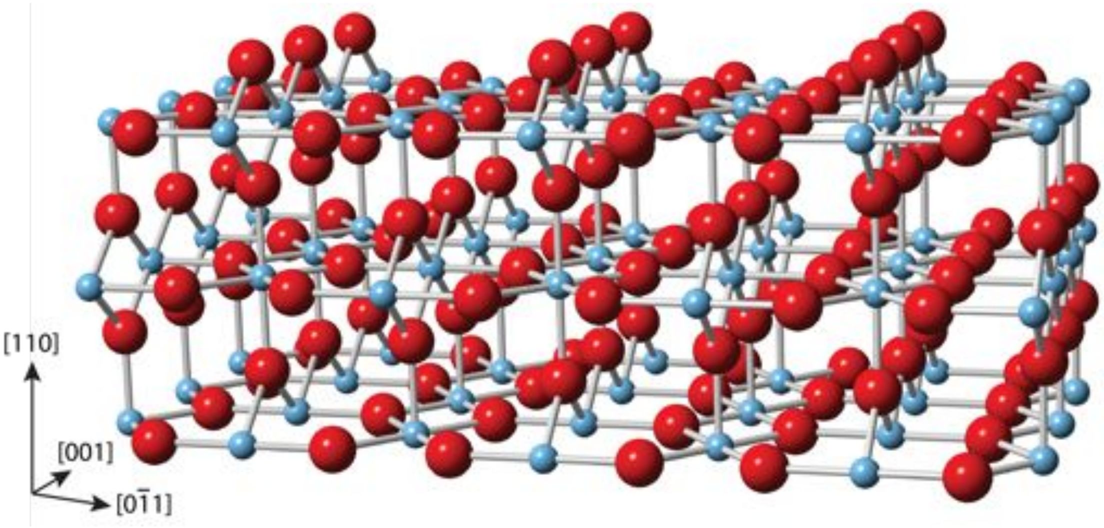

Figure 4.1: A model of the TiO_2(110)(1 x 1) surface consisting of rows of five-fold coordinated titanium atoms (TI_{5c}) and bridging oxygens (O_{br}). Large red and small blue spheres are oxygen and titanium atoms respectively.

4.2 Experimental Procedure

4.2.1 Scanning Tunnelling Microscopy

4.2.1.1 Water Partial Pressure Experiment

STM images were recorded with an Omicron UHV STM/AFM consisting of a preparation and analysis chamber both having a base pressure of ~1 x 10^{-10} mbar (see Chapter 3.1). All images were recorded in constant current mode with the sample positively biased with respect to the tip. A sample bias of 1.0 - 1.5 V and a tunnelling current of 0.1 - 0.25 nA were used to record all the images described in this chapter. Initially, repeated cycles of Ar^+ bombardment and annealing to 1000 K were undertaken to prepare the TiO_2(110) sample (Pi-Kem) in UHV to produce a clean and well-ordered (1 x 1) surface. Later, the annealing temperature was increased to 1150 K resulting in a mixed (1 x 1) / (1 x 2) surface [13]. Data from Auger electron spectroscopy (AES), low energy electron diffraction (LEED), and STM were used to ensure clean and well-ordered surfaces.

The sample surface was exposed to H_2O vapour via a leak valve attached to the analysis chamber, after several freeze-pump-thaw cycles to further purify the ultra-pure liquid. An *in-situ* mass spectrometer was used to ensure that the H_2O vapour was free of contaminants.

4.2.1.2 Water Dip Experiment

STM images were recorded by Tom Woolcot with an Omicron UHV VT-STM (see Chapter 3.1), consisting of a preparation and analysis chamber both having a base pressure of $\sim$1 x 10^{-10} mbar. Sample preparation, similar to that of the partial pressure experiment, produced a clean, well-ordered (1 x 1) surface.

The sample was dipped in ultra pure, deoxygenated H_2O for a range of volumes and times. Surface contamination was avoided by purging the load lock with nitrogen and any possible UV-induced modification was avoided via the use of a red light. Immediately after the dip, the sample was reintroduced into UHV where it was transferred to the analysis chamber for STM measurements.

4.2.2 Surface X-ray Diffraction

SXRD measurements were carried out on ID32 at the European Synchrotron Radiation Facility (ESRF), employing UHV facilities located in the Surface Characterisation Laboratory for sample preparation. Repeated cycles of Ar^+ bombardment and annealing to 1000 K were undertaken to prepare the TiO_2(110) sample (Pi-Kem) in UHV. Data from Auger electron spectroscopy (AES), low energy electron diffraction (LEED), and STM indicated that a clean and well-ordered (1 x 1) surface was produced. We note that the sample colour was translucent green-blue, indicating a relatively low level of bulk reduction, and that no other phases associated with more highly reduced samples were apparent in STM [13]. Once prepared, the samples were transferred under UHV to a bespoke, portable baby chamber (see Chapter 3.5.3), which permits SXRD from surfaces in vacuum, controlled gas atmosphere, and liquid environments [14].

To facilitate diffraction measurements, the baby chambers were mounted on a six-circle diffractometer, located on ID32, with the sample surface in the horizontal plane. Data were primarily collected using rocking scans in which the sample is rotated about its surface normal while scattered X-ray intensity is measured. For selected (h,k) such scans were conducted as a function of l, and then integrated and corrected [15], to enable plots of structure factor versus perpendicular momentum transfer to be produced for various crystal truncation rods (CTRs). Additional scans in h and k at small l (∼0) demonstrated that the surface periodicity remained (1 x 1) throughout all of the measurements. A photon energy of 17.7 keV was employed for these SXRD measurements, which were all conducted with the sample at room temperature.

To systematically study the impact of H_2O on the geometry of $TiO_2(110)(1 \text{ x } 1)$, SXRD measurements were performed with the sample in three different environments. Initially, in order to ensure the integrity of the surface preparation, data were acquired from the substrate in UHV, i.e. the $TiO_2(110)(1 \text{ x } 1)$-UHV interface.

4.2.2.1 Water Droplet - $H_2O_{(l)-droplet}$

Subsequently, a dataset was recorded from $TiO_2(110)(1 \text{ x } 1)$-$H_2O_{(l)}$. To achieve exposure to $H_2O_{(l)}$, the sample chamber was vented to pure dry nitrogen, a glass/teflon tubular liquid delivery system inserted, and a $H_2O_{(l)}$ droplet ($H_2O_{(l)-droplet}$) (de-aerated, 18.2 MΩ cm, total organic content < 2 ppm) delivered to the sample surface using two syringe pumps (see Chapter 3.5.3.2). Datasets consisting of 550 and 1450 non-equivalent reflections were obtained from $TiO_2(110)(1 \text{ x } 1)$-UHV and $H_2O_{(l)-droplet}$, respectively.

4.2.2.2 Water Dip - $H_2O_{(l)-dip}$

After preparation and characterisation by STM and LEED (no SXRD characterisation of the clean UHV surface was performed, but our experience in preparing these samples ensures its integrity), the sample was dipped in ∼20 ml of ultra-pure, deoxygenated H_2O for approximately 15 seconds. To avoid surface contamination/UV-induced modication this procedure was performed in a glove bag filled with argon, illuminated only by red light. Immediately after the dip the sample was re-introduced into UHV where it was transferred to the beamline via a baby chamber that was directly mounted onto a six-circle diffractometer. A large data set of 20 CTRs that, after corrections, comprised of 835 non-equivalent reflections.

4.2.2.3 Water Partial Pressure - $H_2O_{(g)}$

The clean surface was measured first and then H_2O vapour was admitted to the chamber and further diffraction data were recorded at a series of H_2O partial pressures. Water partial pressure was increased incrementally from $\sim 10^{-6}$ mbar to 1 mbar after which the chamber was pumped down and measurements were taken at a pressure of $\sim 10^{-6}$ mbar. Water was then re-introduced first to a partial pressure of ~5 mbar and then to ~10 mbar. Diffraction intensity along three CTRs was acquired (i.e. (0,1,l), (2,1,l), (1,2,l)).

The data are indexed with reference to the (1 x 1) unit cell of the (110) surface, described by lattice vectors (a_1, a_2, a_3), which are parallel to the [$1\bar{1}0$], [001], and [110] directions, respectively, where $a_1 = a_3 = a\sqrt{2}$, and $a_2 = c$ (a = 4.593 Åand c = 2.958 Å are the lattice constants of the tetragonal rutile crystal structure [16]). The coordinates of the corresponding reciprocal lattice vectors are denoted by h, k, l.

4.3 Results and Discussion

4.3.1 Scanning Tunnelling Microscopy

4.3.1.1 Partial Pressure Experiment - (2 x 1) Overlayer

STM images of the clean $TiO_2(110)$-(1 x 1) surface recorded at room temperature show very good agreement with the literature [13, 17], see Figure 4.2a. They consist of bright and dark rows in the [001] direction assigned to the five-fold coordinated Ti atoms (Ti_{5c}) and bridging O atoms (O_{br}), respectively. Bright features seen on the dark rows are O_{br} vacancies (O_{br-v}) and brighter features are bridging hydroxyls (OH_{br}). No features were seen to be present on the bright rows, usually physisorbed water molecules (H_2O_t), which are located atop of the Ti_{5c} and are more commonly present at lower temperatures [18] or on the 'perfect' $TiO_2(110)$-(1 x 1) surface [19]. A representative STM image of $TiO_2(110)$ after *in-situ* exposure to a constant partial pressure of 1 x 10^{-6} mbar H_2O for ∼3 h (∼103 L) is shown in Figure 4.2b. It shows an ordered overlayer consisting of bright features. Line profiles (Figures 4.2c and 4.2d) indicate that it is of (2 x 1) periodicity; a doubling of the unit cell in the [001] direction making the surface unit cell size ∼6 Å x 6 Å. However, it is unclear from this image where the overlayer is situated with respect to the surface.

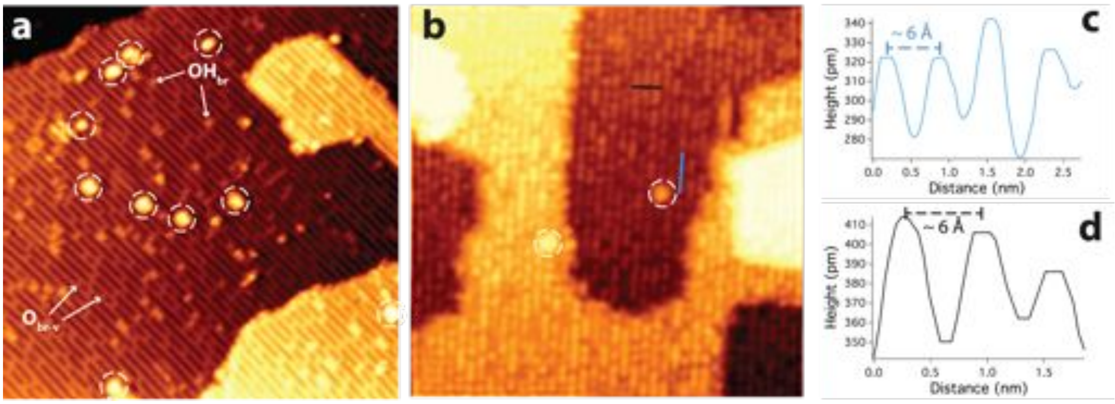

Figure 4.2: Representative STM images of (a) UHV as-prepared $TiO_2(110)(1 \times 1)$ surface. Bright and dark rows are Ti_{5c} and O_{br} rows, respectively. Features present on O_{br} rows are bridging oxygen vacancies (O_{br-v}) and bridging hydroxyls (OH_{br}) (b) (2 x 1) water overlayer after subjecting surface to 1 x 10^{-6} mbar H_2O for ∼3 h. Dotted circles in (a) and (b) show a small coverage of (1 x 2) reconstruction (c) Line profile along the [001] direction showing a doubling of the unit cell length to ∼6 Å (d) Line profile along the [0$\bar{1}$1] direction showing unit cell length remains ∼6 Å.

It is well known that annealing $TiO_2(110)$ surfaces to higher temperatures induces a reconstruction that has (1 x 2) symmetry, with a doubling of the periodicity along the [1$\bar{1}$0] direction [13]. There is still some controversy surrounding the exact structure of this reconstruction with several models, such as the ‘missing row [20], ‘added Ti_2O_3 row [21] and ‘added row [22] models, presented in the literature. However, the interest of this reconstruction here lies in the registry of the (1 x 2) strands with the Ti_{5c} rows of the substrate making it a suitable marker, as shown in Figure 4.3a. This phenomenon is confirmed by superimposing a grid (green lines) so that it can be clearly seen that the reconstruction is indeed in registry with the Ti_{5c} rows.

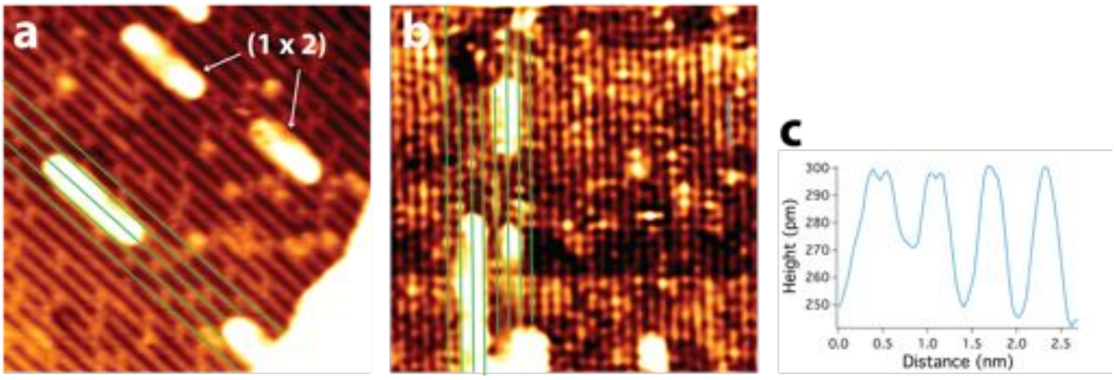

Figure 4.3: Representative STM images of (a) UHV as-prepared $TiO_2(110)$-(1 x 1)-(1 x 2) surface (b) (2 x 1) water overlayer after subjecting surface to 1 x 10^{-6} mbar H_2O for ∼3 h (c) Line profile along the [001] direction showing a doubling of the unit cell to ∼6 Å. Large bright features are strands associated with reduced (1 x 2) phase of $TiO_2(110)$. Green lines illustrate (1 x 2) strands are in registry with bight Ti_{5c} rows.

Figure 4.3b displays an STM image after exposing the $TiO_2(110)$-(1 x 2) surface to a constant partial pressure of 1 x 10^{-6} mbar H_2O for ∼3 h (∼103 L). As before, an ordered overlayer is formed with (2 x 1) periodicity (Figure 4.3c) and at first glance the (1 x 2) reconstruction seems to have had no structural effect on the overlayer. Using a similar grid as the one in Figure 4.3a, we can see that the overlayer is in registry with the strands of (1 x 2) reconstruction. This is strong evidence to suggest that the overlayer seen by STM is bound to the Ti_{5c} rows.

A series of H_2O partial pressure experiments at different coverages were dosed on the $TiO_2(110)$-(1 x 2) surface as shown in Figure 4.4. Even at the highest dosage of 1 x 10^{-7} mbar for 100 L a very hydroxylated surface comprising of OH_{br}'s is formed and no sign of OH_t's. This suggests the (2 x 1) overlayer is only formed at very high dosages of H_2O.

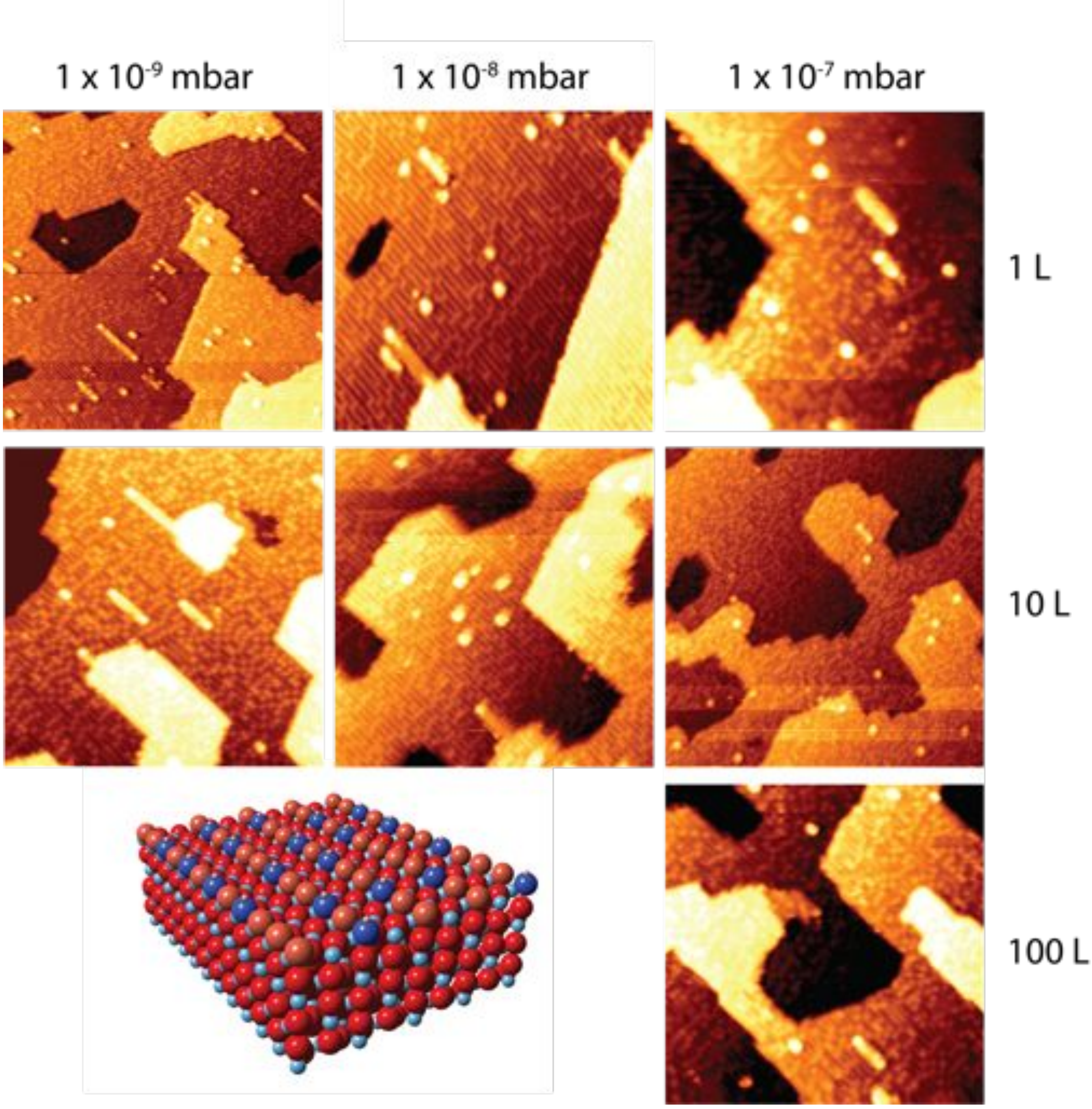

Figure 4.4: Representative STM images of the $TiO_2(110)$-(1 x 1)-(1 x 2) surface after exposing to 1 x 10^{-9} mbar, 1 x 10^{-8} mbar and 1 x 10^{-7} mbar of H_2O for 1 L, 10 L and 100 L coverage. At these relatively low coverage's a (2 x 1) overlayer did not form instead an increase of surface OH_{br}'s results, as illustrated in the ball and stick model.

4.3.1.2 Scanning Tunnelling Microscopy and Photoelectron Spectroscopy - Water Dip (2 x 1) Overlayer [23]

Previous work [23] by Tom Woolcot in the group using STM has shown that after dipping the as-prepared $TiO_2(110)(1 \times 1)$ sample in $H_2O_{(l)}$, an ordered (2 x 1) overlayer is formed (see Figure 4.5). Sample preparation and the dipping procedure were similar to $H_2O_{(l)-dip}$, described above. However, in Ref [23] experiments were performed for a range of $H_2O_{(l)}$ volumes (10 mL - 1 L) and durations (0.5 - 120 mins), as well as for samples with different levels of bulk reduction (7.3% and 10.2% O_{br-v}). All the conditions measured, except for longer durations, produced a similar (2 x 1) overlayer as the STM experiments in this work. They found that having different O_{br-v} concentrations did not affect the (2 x 1) superstructure.

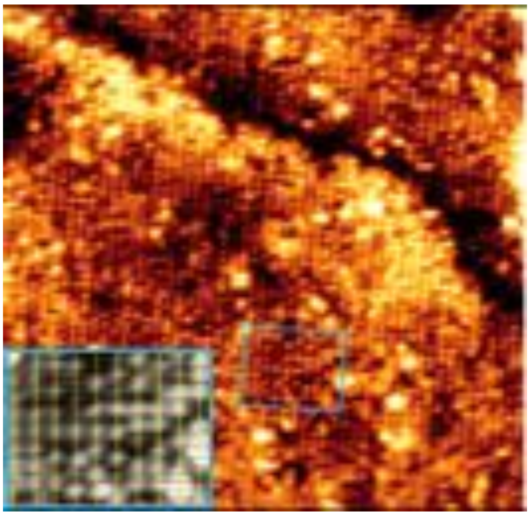

Figure 4.5: Representative STM image of the $TiO_2(110)(1 \times 1)$ surface after dipping in H_2O. The (2 x 1) overlayer is shown using a unit cell grid of an enlarged region (highlighted in blue). Reproduced from Ref [23].

To gain an understanding of the chemical nature of the superstructure, in Ref [23] an investigation on the dipped surface using photoelectron spectroscopy (PES) was performed. It was concluded that the (2 x 1) overlayer is comprised solely of OH due to the presence of a two state spectrum, as opposed to a three state spectrum characteristic of adsorbed H_2O. The valence band measurements of the as-prepared and dipped $TiO_2(110)(1 \times 1)$ surface, as well as a spectrum of adsorption of $H_2O_{(g)}$ at low temperature from the literature [5], are shown in Figure 6a. Figure 6b is a difference spectrum that illustrates the two characteristic states, 1π and 3σ, of chemisorbed OH.

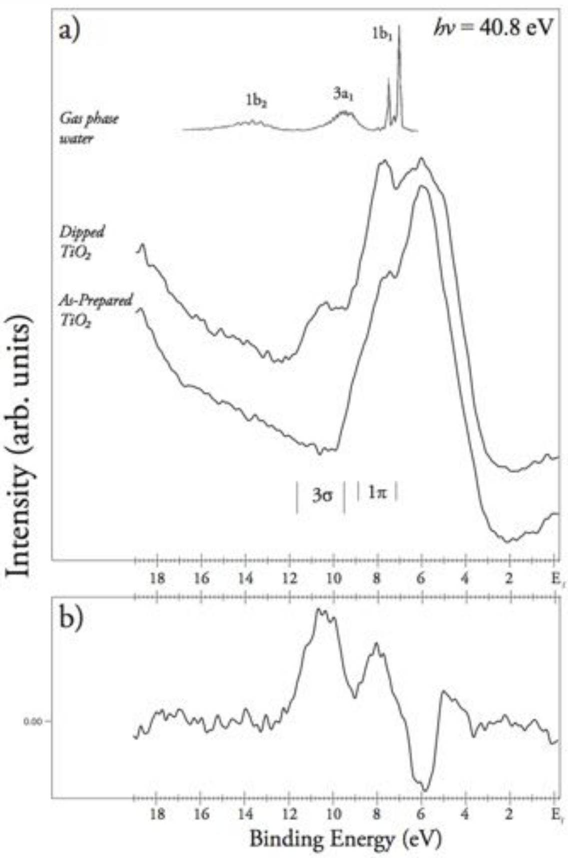

Figure 4.6: (a) Normal emission PES valence band spectra of the as-prepared and dipped $TiO_2(110)(1 \text{ x } 1)$ surfaces. Also shown is a spectrum of the adsorption of $H_2O_{(g)}$ at low temperature from the literature [5] b) Difference spectra illustrating the two states, 1π and 3σ associated with chemisorbed OH. Reproduced from Ref [23].

Although the question of where the overlayer lies with respect to the surface and its chemical nature have been answered, other questions still remain; how exactly is the terminal OH, OH_t, bonded to the Ti_{5c} and what effect does the overlayer/water adsorption have on the $TiO_2(110)$ substrate. To gain this much needed information, SXRD experiments to examine the structures resulting from several partial pressures of water above the surface ($H_2O_{(g)}$), as well as the sample dipped in water ($H_2O_{(l)-dip}$) and liquid water in contact with the surface ($H_2O_{(l)-droplet}$).

4.3.2 Surface X-ray Diffraction

4.3.2.1 UHV as-prepared surfaces (Prior to water partial pressure and water droplet measurements)

Application of the preparation methodology to TiO_2(110)-UHV, using a parameter space identical to that adopted in a previous SXRD study of this system [24], resulted in an optimised geometry that is essentially equivalent to that obtained previously (see Table 4.1). Non-structural parameters were also very similar to those given in Ref [24]. During the fitting procedure of the clean surface (water model, vapour pressure), 51 (71, 49) parameters were optimised; 35 (47, 36) atomic displacements, 12 (17, 14) DW factors, a roughness parameter, surface fraction parameter and a scaling factor.

For $H_2O_{(l)-droplet}$ and $H_2O_{(g)}$, the best fits obtained for the UHV as-prepared surfaces produced a χ^2 of 1.0, which represents a very good agreement between experiment and theory as well as previous work [24]. All non-structural parameters adopted reasonable values; the surface fraction parameter was 93%, indicating that model represents most of the surface with the rest arising from defects. The structural model for both experiments comprises of a single terrace consisting of three unit cells in the out-of-plane direction where all atoms considered in the fitting procedure were fully occupied.

4.3.2.2 Water Dip - $H_2O_{(l)-dip}$

Figure 4.7 illustrates a ball and stick model representing the trial (2 x 1) overlayer with an atop OH bonded to every other Ti_{5c} atom (OH_t model). The best fit model, with a χ^2 of 1.4, contained a total of 53 free-fitting parameters during the analysis; 38 atomic displacements corresponding to a total of 3 unit cells (17 layers) in the out-of-plane direction, 12 in-plane Debye-Waller parameters, a roughness parameter and a scaling parameter. The STM work described above [23] show very little change to the morphology of the surface after dipping in H_2O. As we are trying to simulate a near perfect model the occupancies of all atoms were not considered i.e. they were fixed to 1, except that of the OH molecule which was found to be 0.5. This is as expected for a (2 x 1) overlayer. When fixing the occupancy of the OH molecule to 1, such that it is fully occupied and similar to models presented in the literature [12] for the air-annealed surface, the χ^2 worsens to a value of 1.6. No water molecules were present above the OH_t in agreement with he STM result [23]. Representation of a water molecule or hydroxyl in the analysis is in the form of an oxygen atom only due to the low X-ray scattering contribution from the hydrogen.

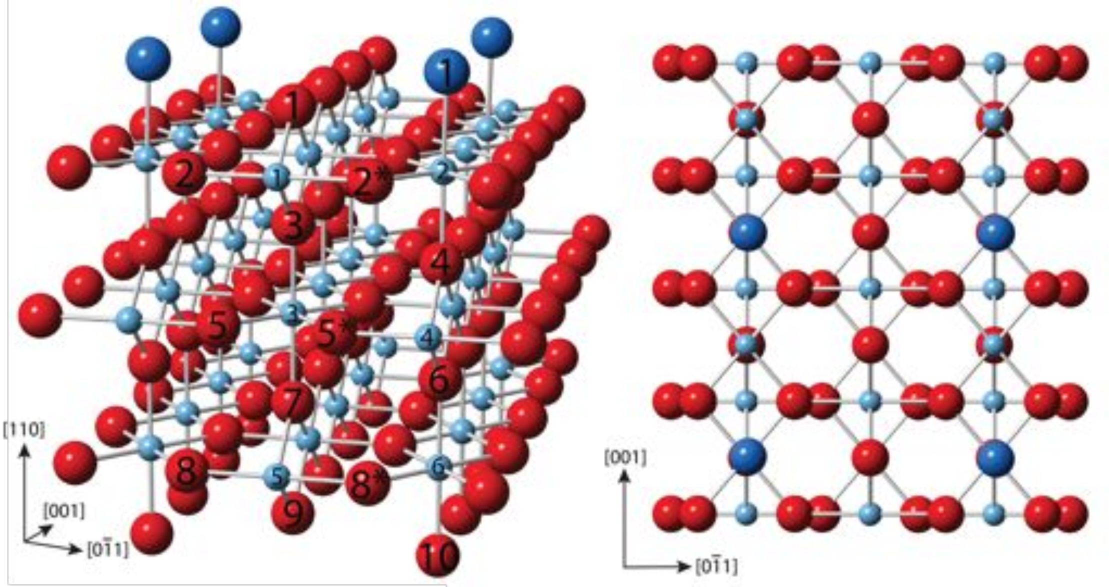

Figure 4.7: A cross-section view and top view of the best-fit ball and stick model of the $TiO_2(110)(1 \times 1)$ - H_2O interface. Large red spheres are oxygen atoms, small blue spheres are titanium atoms and large dark blue spheres are OH molecules. Arrows represent direction and magnitude of atomic displacements away from the bulk structure. OH(1) was found to have an occupancy of 50% thus representing the (2 x 1) overlayer seen by STM. The overlayer is formed by terminal OHs (OH_t) bonded to every other Ti atom in the [001] direction. Hydrogen atoms are purposely left out due to their low scattering contribution from X-rays. The numerical labelling of the atoms is employed in Table 4.1 for identification purposes. Symmetry-paired atoms are denoted as 2^*, 5^* and 8^*.

Figure 4.8 displays a comparison between the calculated structure factors of the OH_t model shown in Figure 4.7 (red line) and the experimental data (black error bars) for the CTRs collected and shows good agreement between experiment and theory. The bond distance between OH(1) and Ti(2) is 1.95 ± 0.02 Å in good agreement with the literature value of 1.85 ± 0.08 Å [18]. Comparing the atomic displacements in the out-of-plane direction for the OH_t model and TiO_2(110)-UHV [24] reveal that the structure has become more bulk-like (see Table 4.1). This is especially the case for the outermost atoms where the cations, Ti(1) and Ti(2), in UHV have displacements of 0.25 ± 0.01 Å and -0.11 ± 0.01 Å and after dipping have relaxed to 0.07 ± 0.01 Å and 0.03 ± 0.01 Å, respectively. Similarly, the anions, O(1) and O(2) in UHV have displacements of 0.10 ± 0.04 Å and 0.17 ± 0.03 Å and after dipping have relaxed to 0.03 ± 0.03 Å and 0.06 ± 0.03 Å, respectively.

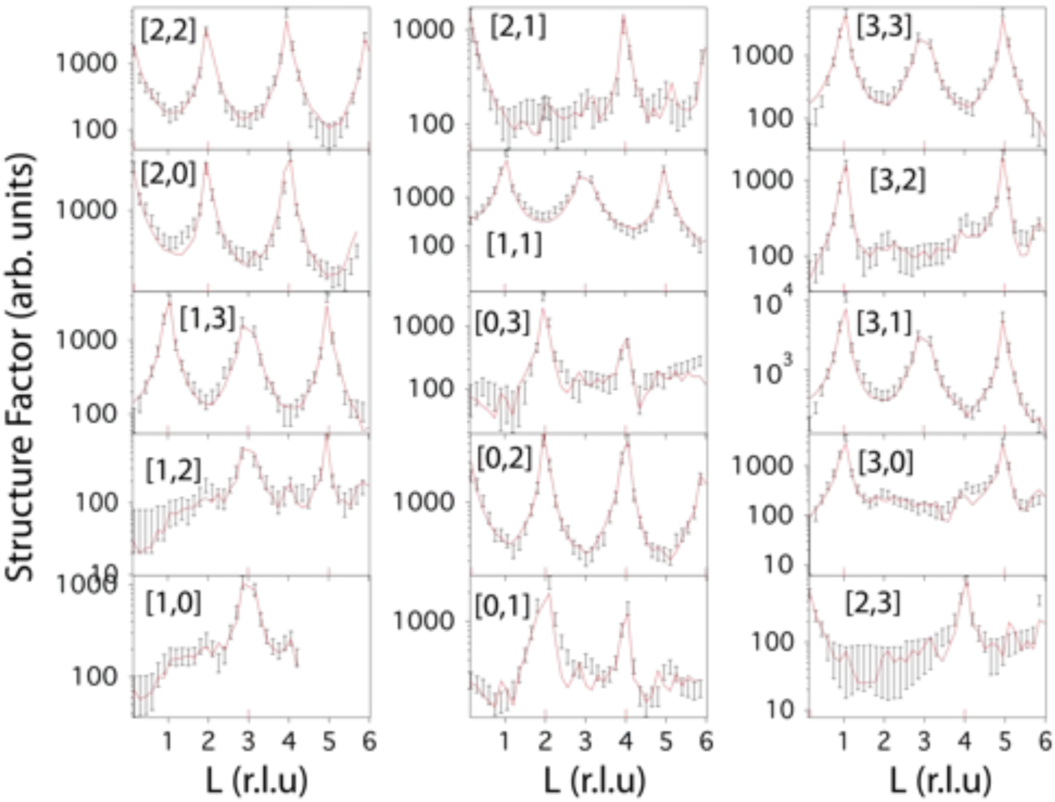

Figure 4.8: Several representative CTRs measured after the $TiO_2(110)(1 \times 1)$ surface was dipped in ~20 ml of H_2O for ~15 s. Black error bars and solid red line are the experimental data and theoretically calculated data, respectively. Bulk Bragg peaks are indicated by red markers on the horizontal axis.

As for the non-structural parameters, the surface fraction parameter was found to be 0.86, which indicates that most of the surface is explained by the model with the remainder arising from defects or areas of disorder. The surface roughness, calculated using the approximate beta model [25], was found to be 0.20 indicating that the illuminated area measured with X-rays is a fairly rough surface.

4.3.2.3 Water Droplet - $H_2O_{(l)-droplet}$

Exposing the $TiO_2(110)$-(1 x 1) surface to liquid water and taking measurements in-situ using the electrochemical cell baby chamber (see Chapter 3.5.3.2) produces a best-fit model ($\chi^2 = 1.7$) that reveals the presence of a hydration layer above the OH_t (Figure 4.9). Comparison between the calculated structure factors and experimental data are illustrated in Figure 4.10. The contact layer was found to be similar to that found for $H_2O_{(l)-dip}$ i.e every other surface Ti_{5c} site is occupied with an OH_t. Evidence for this particular site being occupied with an OH and not a H_2O molecule is given by the bond distance between OH(1) and Ti(2) which was found to be 1.95 ± 0.02 Å and forcibly changing to a larger value increases the χ^2 to a value of 2.0. As for the second water layer, all atoms considered in this layer were given the freedom to displace in the [001], [$0\bar{1}1$] and [110] crystallographic directions during the fitting procedure. The resulting best-fit model, see Figure 4.9, is similar to that found in Ref [12]; their model, $\chi^2 = 3.9$, suggests that a simple (1 x 1) surface termination is maintained in the presence of $H_2O_{(l)}$, with a mixture of OH and H_2O species bound to the Ti_{5c} showing a difference in the contact layer from our model. However, similar to our work they also detect the presence of a hydration layer in the form of three distinct adsorption sites, $H_2O(1)$ located above the O_{br} and $H_2O(2)$ and $H_2O(3)$ located in a bridging site between OH_t and O_{br}. The occupancy of $H_2O(1)$ was found to be 1.0 ± 0.06 and 0.5 ± 0.06 for $H_2O(2)$ and $H_2O(3)$. The bond distance between O(1) and $H_2O(1)$ is 2.53 ± 0.04 Å, the $H_2O(2)$ OH(1) bond distance is 2.70 ± 0.04 Å and the $H_2O(3)$ OH(1) bond distance is 2.70 ± 0.04 Å.

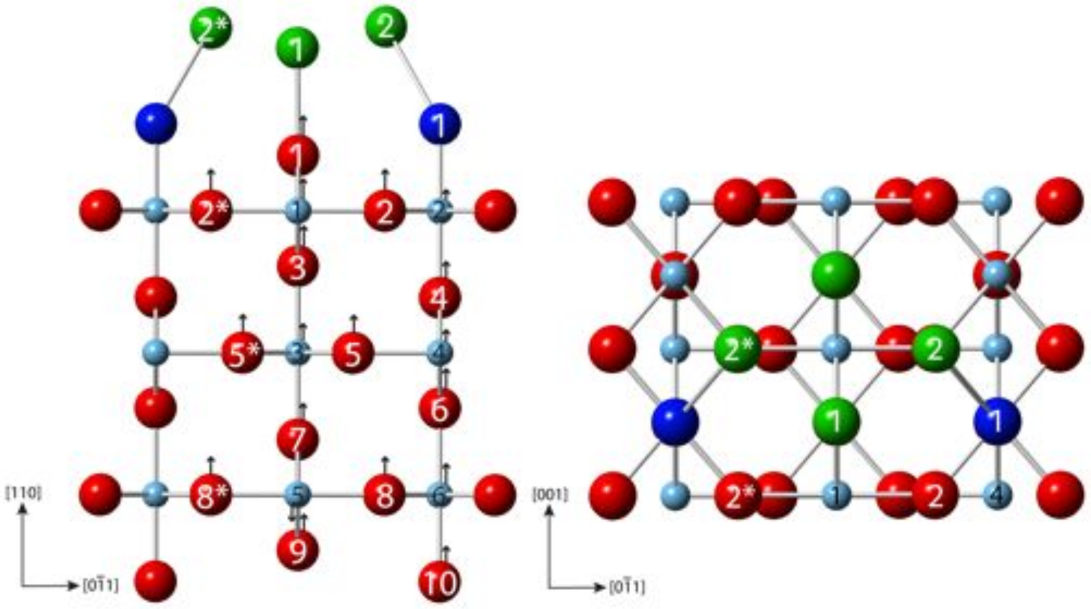

Figure 4.9: A cross-section view and top view of the best-fit ball and stick model of the TiO_2(110)(1 x 1) surface in contact with liquid water via the use of an electrochemical cell. Large red spheres are oxygen atoms, small blue spheres are titanium atoms, large dark blue spheres are OH molecules of the contact layer and large green spheres are H_2O molecules of the hydration layer. Arrows represent direction and magnitude of atomic displacements away from the bulk structure. The OH(1) - Ti(2) bond distance is 1.95 ± 0.02 Å, the H_2O(1) O(1) bond distance is 2.53 ± 0.04 Å, the H_2O(2) - OH(1) bond distance is 2.70 ± 0.04 Å and the H_2O(3) - OH(1) bond distance is 2.70 ± 0.04 Å. All OH/H_2O molecules were found to have occupancies of 50%. Hydrogen atoms are purposely left out due to their low scattering contribution from X-rays. The numerical labelling of the atoms is employed in Table 4.1 for identification purposes. Symmetry-paired atoms are denoted as 2^*, 5^* and 8^*.

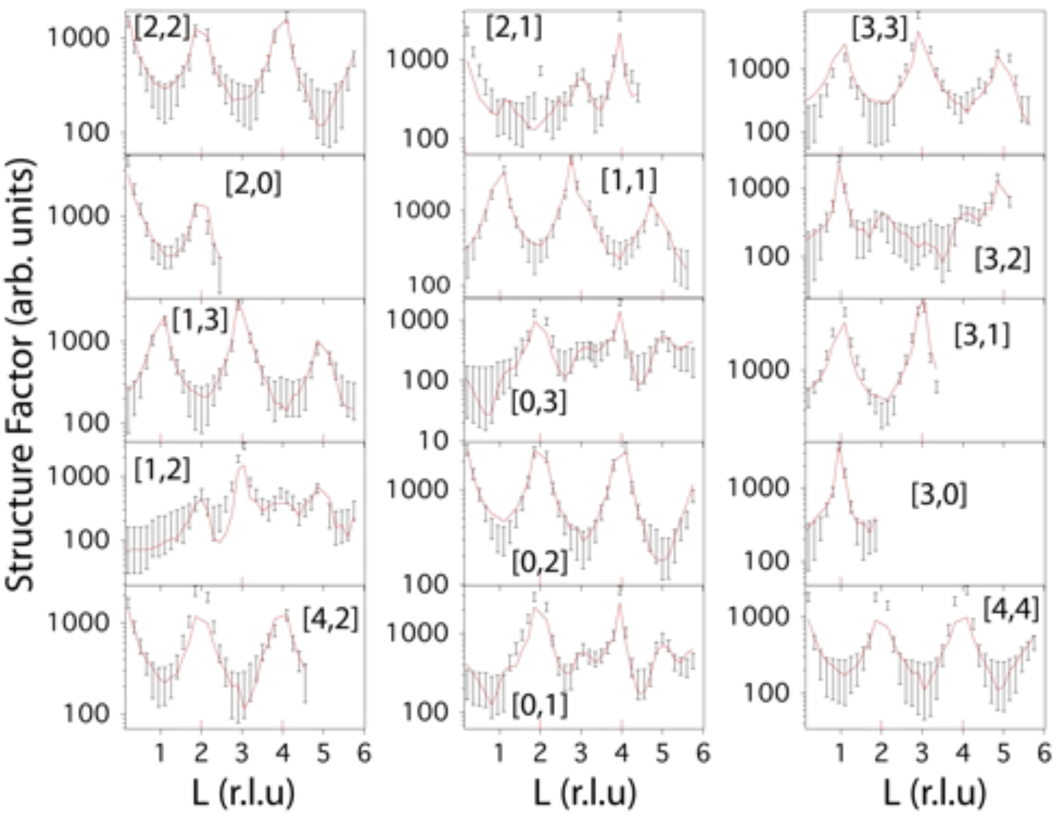

Figure 4.10: Several representative CTRs measured after exposure of the $TiO_2(110)(1 \times 1)$ surface to liquid H_2O via the use of an electrochemical cell. Black error bars and solid red line are the experimental data and theoretically calculated data, respectively. Bulk Bragg peaks are indicated by red markers on the horizontal axis.

Considerable changes to the optimised TiO_2(110)(1 x 1)-UHV geometry were required to achieve this fit. Most notably the cations of the first two layers, Ti(1)-(4), which have displaced such that they have become more bulk-like, a similar result to $H_2O_{(l)-dip}$, see Table 4.1. A closer comparison of the displacements between this experiment and $H_2O_{(l)-dip}$ show that nearly all the displacements listed in Table 4.1 are in quantitative agreement with each other. The close similarity of these structures is further represented in Figure 4.11 which displays the experimental structure factors of the (0,1,l) and (1,2,l) and (2,1,l) CTRs for the $H_2O_{(l)-droplet}$ (red error bars), $H_2O_{(l)-dip}$ (blue error bars) and the TiO_2(110)(1 x 1)-UHV surface (black error bars) [24]. It can be clearly seen that the modulations of both the $H_2O_{(l)-dip}$ and $H_2O_{(l)-droplet}$ are significantly less intense when compared to the $TiO_2(110)(1 \times 1)$-UHV surface however differences are present within the profiles of $H_2O_{(l)-dip}$ and $H_2O_{(l)-droplet}$ themselves. These were attributed to the hydration layer found for the $H_2O_{(l)-droplet}$ best-fit.

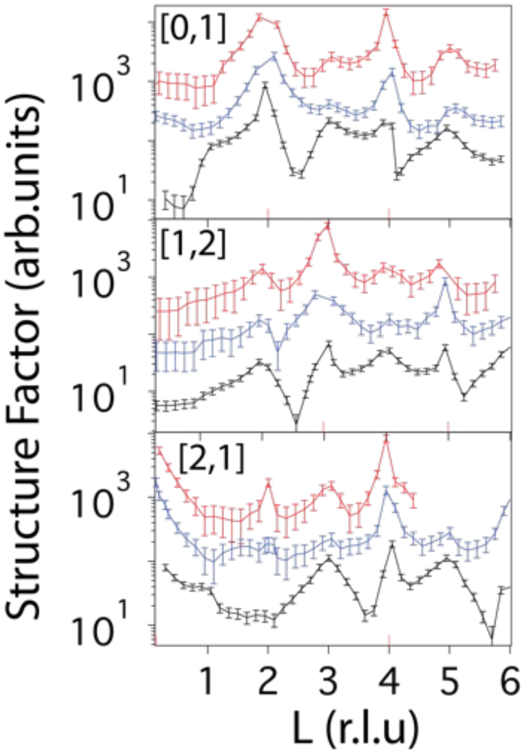

Figure 4.11: A comparison of the experimental structure factors of the $TiO_2(110)(1 \times 1)$ H_2O interface for the (0,1,l), (1,2,l) and (2,1,l) CTRs. Black, blue and red error bars represent the $TiO_2(110)(1 \times 1)$-UHV [24], $H_2O_{(l)-dip}$ and $H_2O_{(l)-droplet}$ surfaces, respectively. Bulk Bragg peaks are indicated by red markers on the horizontal axis. Profiles are offset for clarity.

Listed in Table 4.1 are the atomic displacements for the $TiO_2(110)(1 \times 1)$ / $H_2O_{(l)}$ best fit model of Ref [12]. It can be clearly seen that the atomic displacements for all atoms listed are significantly less displaced from their ideal bulk positions than the $H_2O_{(l)-dip}$ and $H_2O_{(l)-droplet}$ of this work. This, as well as the difference in the contact layer with H_2O, could be attributed to their surface preparation which was not conducted in UHV but instead consisted of wet chemical treatments, including hydrothermal reaction with water, and annealing in air at 1373 K. Furthermore, no surface characterisation was undertaken prior to exposure to $H_2O_{(l)}$. Given that spectroscopy data from similarly non-UHV prepared $TiO_2(110)$ surfaces indicate the potential for significant contamination [26], it is very likely that the surface is saturated with a layer of disordered carbon and thus reducing the distortions in the selvedge.

4.3.2.4 Water Partial Pressure - $H_2O_{(g)}$

All H_2O partial pressures measured, ranging from $\sim 10^{-6}$ mbar to ~ 10 mbar, can be described using the model displayed in Figure 4.7. This structure, similar to the structure found for $H_2O_{(l)-dip}$, produced a best-fit χ^2 range from 1.3 - 1.9, which represents a good agreement between experiment and theory. All non-structural parameters adopted reasonable values; the roughness parameter, although considered in the fit always tended towards zero and the surface fraction parameter was always above 90%.

Shown in Figure 4.12 are the experimental and theoretically calculated structure factors for the (0,1,l), (1,2,l) and (2,1,l) CTRs. No significant changes in the profiles are seen after exposing the surface to more than 1×10^{-6} mbar partial pressure of H_2O which suggests the average structure is the same. For all conditions of $H_2O_{(g)}$ measurements, the occupancy of OH(1) was 0.5 and the bond distance between it and Ti(2) was 1.95 ± 0.02 Å, representative of the (2 x 1) overlayer seen in $H_2O_{(l)-dip}$ and the contact layer of $H_2O_{(l)-droplet}$. However, at the higher partial pressures of water no hydration layer was observed. Relative humidity [27] studies have shown that exposing the $TiO_2(110)(1 \times 1)$ surface to ~ 10 mbar partial pressure of H_2O results in a coverage of ~ 3 ML and so it was expected that the structure would be similar to $H_2O_{(l)-droplet}$. A a possible reason for the insensitivity of the hydration layer can be due to a combination of the low scattering factor of oxygen atoms and the lack of experimental data points. This indeed was determined to be the case; after limiting the dataset of $H_2O_{(l)-droplet}$ to the three CTRs measured in $H_2O_{(g)}$, the hydration layer, ($H_2O(1)$, $H_2O(2)$, $H_2O(3)$), had an occupancy of 0 thus highlighting the importance of a large dataset. For the same reason a full quantitative structural analysis could not be performed due to the large calculated error bars for the atomic displacements.

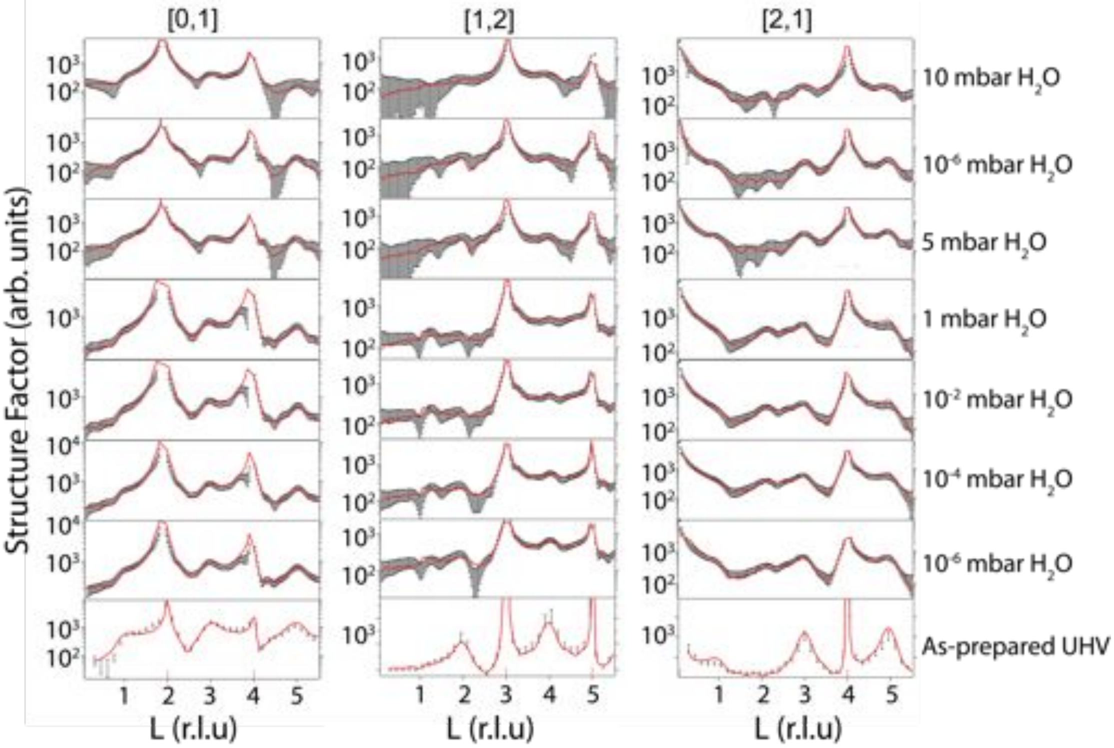

Figure 4.12: Representative CTRs measured after exposure of the TiO_2(110)(1 x 1) surface to several partial pressures of H_2O ranging from the UHV up to 10 mbar. Black error bars and solid red line are the experimental data and theoretically calculated data respectively. Bulk Bragg peaks are indicated by red markers on the horizontal axis.

4.4 Conclusions

We have investigated the interaction of H_2O with the rutile TiO_2(110) surface using STM and SXRD. After exposing the surface to 1 x 10^{-6} mbar partial pressure of H_2O for ∼3 h a (2 x 1) overlayer is produced as seen with STM. Previous work in the group has shown the overlayer also forms after dipping the surface in ultra pure deaerated liquid H_2O and PES measurements suggest that the overlayer is comprised of hydroxyls only.

To gain insight into the registry of the (2 x 1) overlayer with respect to the surface the sample was further reduced to produce distinctive strands of (1 x 2) reconstruction. These proved excellent

Table 4.1: Atomic displacements away from the bulk-terminated structure of $TiO_2(110)(1 \times 1)$-UHV ($H_2O_{(l)-droplet}$ and -$H_2O_{(g)}$) and $H_2O_{(l)}$ interface ($H_2O_{(l)-dip}$ and $H_2O_{(l)-droplet}$) resulting from analysis of the SXRD data. Also listed are values obtained from previous SXRD measurements of $TiO_2(110)(1 \times 1)$-UHV [24] and $H_2O_{(l)}$ [12]. Figures 4.7 and 4.9 provide a key to the identity of the atoms. A negative value indicates that the atom moves towards the bulk for a displacement perpendicular to the surface plane and in the $[1\bar{1}0]$ direction for a lateral displacement.

Atom	UHV (Å)			Liquid H_2O (Å)		
	[24]	$H_2O_{(l)-droplet}$	$H_2O_{(g)}$	$H_2O_{(l)-dip}$	$H_2O_{(l)-droplet}$	[12]
Ti(1)	0.25 ± 0.01	0.17 ± 0.01	0.15 ± 0.01	0.07 ± 0.01	0.09 ± 0.01	-0.002 ± 0.004
Ti(2)	-0.11 ± 0.01	-0.06 ± 0.01	0.03 ± 0.01	0.03 ± 0.01	0.03 ± 0.01	-0.051 ± 0.004
Ti(3)	-0.08 ± 0.01	-0.02 ± 0.01	0.05 ± 0.01	0.07 ± 0.01	0.06 ± 0.01	0.021± 0.004
Ti(4)	0.19 ± 0.01	0.12 ± 0.01	0.14 ± 0.01	0.01 ± 0.01	0.04 ± 0.01	-0.016 ± 0.004
O(1)	0.10 ± 0.04	0.10 ± 0.04	0.13 ± 0.03	0.03 ± 0.03	0.08 ± 0.04	0.004 ± 0.009
O(2)	0.17 ± 0.03	0.13 ± 0.03	0.09 ± 0.04	0.06 ± 0.03	0.08 ± 0.03	-0.09 ± 0.006
O(3)	0.07 ± 0.04	0.07 ± 0.04	0.10 ± 0.04	0.04 ± 0.03	0.07 ± 0.03	0.008 ± 0.007
O(4)	0.00 ± 0.03	0.02 ± 0.03	0.04 ± 0.04	0.05 ± 0.03	0.05 ± 0.05	-0.012 ± 0.008
O(5)	0.04 ± 0.03	0.03 ± 0.03	0.10 ± 0.03	0.01 ± 0.03	0.06 ± 0.03	-0.05 ± 0.012
O(6)	0.01 ± 0.04	0.04 ± 0.04	-0.04 ± 0.03	0.04 ± 0.03	0.08 ± 0.05	0.005 ± 0.017
O(7)	0.01 ± 0.04	0.01 ± 0.04	0.06 ± 0.03	0.02 ± 0.03	0.06 ± 0.05	-0.002 ± 0.013
O(8)	0.01 ± 0.05	0.01 ± 0.05	0.02 ± 0.04	-0.06 ± 0.05	0.05 ± 0.03	-
Ti(5)	0.08 ± 0.01	0.05 ± 0.01	0.06 ± 0.01	0.01 ± 0.01	-0.04 ± 0.01	0.013 ± 0.003
Ti(6)	-0.04 ± 0.01	-0.02 ± 0.01	0.01 ± 0.01	0.05 ± 0.01	0.08 ± 0.01	-0.01 ± 0.003
O(9)	0.02 ± 0.04	0.03 ± 0.04	0.01 ± 0.04	0.01 ± 0.03	0.04 ± 0.04	-
O(10)	-0.02 ± 0.04	-0.01 ± 0.04	-0.05 ± 0.04	0.03 ± 0.03	0.03 ± 0.03	-

markers for the registry of the surface as they centre on the Ti_{5c} rows. Exposing this surface to 1 x 10^{-6} mbar partial pressure of H_2O for 3 h reproduced the (2 x 1) overlayer where it was shown the rows of OH lie in registry with the Ti_{5c} rows.

These findings are supported by SXRD measurements that show every other surface Ti atom in the [001] direction is occupied with an OH in an atop position. The same average structure was found after exposing the surface to several partial pressures of H_2O ranging from 1 x 10^{-6} mbar up to 10 mbar and after the dipping the surface in ∼20 ml ultra pure deaerated liquid H_2O for ∼15 s. Furthermore, SXRD measurements were also collected for in-situ immersion of liquid via the use of an electrochemical cell. The results revealed the presence of a hydration layer described by three water adsorption sites.

There is clearly still a need for further work on the water/TiO_2(110) system. To build upon the work presented, immediate interest should be focussed on performing theoretical simulations to determine if the proposed (2 x 1) OH overlayer is correct. Combining experimental and theoretical techniques has proved to be a successful recipe for many systems in the past and will help to deepen our understanding of how and why this (2 x 1) ordered overlayer forms. One key question that is of particular interest that could be answered from this combination is at what coverage/exposure of water does the 'switch' from bridging hydroxyls, that has been widely reported at low coverages, to hydroxyls that are bonded atop titanium occur? Another possible investigation of this system could include repeating the above experiments for a highly reduced TiO_2 (110)(1 x 2) surface.

The work in this chapter is by no means a finished article and should not be treated as such by interested readers. Instead it should be thought of as a stepping stone for further development and understanding of the system that is so important in many technological applications. Of the many applications, heterogenous photocatalysis has been shown to be the most promising, particularly when used for degradation of organic compounds and water and air purification. Much of the research has concentrated on enhancing photocatalytic performance by manipulating surface properties (eg. chemical composition, surface defects, surface area etc...) of the substrate as many of the photocatalytic reactions occur at the liquid/solid interface and recently, another avenue to increase the performance has opened up; ionic liquids (IL). These are typically comprised of organic cations and large anions and have started to receive considerable attention due to their unique properties (eg. high ionic conductivity, low volatility, ability to dissolve well etc...). It has been suggested that ILs play an important role in accelerating charge transfer and that the photocatalytic ability of TiO_2 can be improved due to the accelerated separation of photogenerated electrons and holes. It is clear that knowing the structure after water adsorption on the TiO_2 surface, particularly the ordered hydration layer as reported in this chapter, is of direct significance to the improvement of the photocatalytic ability of TiO_2.

References

[1] A. Fujishima, K. Honda, Nature, 238, 37, (1972)

[2] R. L. Kurtz, R. Stockbauer, T. E. Madey, E. Roman, J. L. de Segovia, Surf. Sci., 218, 178, (1989)

[3] L. E. Walle, A. Borg, P. Uvdal, A. Sandell, Phys. Rev. B, 80, 235436, (2009)

[4] M. A. Henderson, Surf. Sci., 355, 151, (1996)

[5] I. M Brookes, C. A. Muryn, G. Thornton, Phys. Rev. Lett., 87, 266103, (2001)

[6] O. Bikondoa, C. L. Pang, R. Ithnin, C.A. Muryn, H. Onishi, G. Thornton, Nat. Mater., 5, 189, (2006)

[7] Z. Zhang, O. Bondarchuk, B. D. Kay, J. M. White, Z. Dohnalek, J. Phys. Chem. B, 110, 21840, (2006)

[8] C. L. Pang, A. Sasahara, H. Onishi, Q. Chen, G. Thornton, Phys. Rev. B, 74, 073411, (2006)

[9] M. A. Henderson, Surf. Sci. Reports, 66, 185, (2011)

[10] L. M. Liu, C. Zhang, G. Thornton, A. Michaelides, Phys. Rev. B, 161415, (2010)

[11] D. Dohnlek, I. Lyubinetsky, R. Rousseau, Prog. Surf. Sci, 85, 161, (2010)

[12] Z. Zhang, P. Fenter, N. C. Sturchio, M. J. Bedzyk, M. L. Machesky, D. J. Wesolowski, Surf. Sci, 601, 1129, (2007)

[13] U. Diebold, Surf. Sci. Rep, 48, 53, (2003)

[14] F. U. Renner, Y. Grnder and J. Zegenhagen, Rev. Sci. Instrum, 78, 033903, (2007)

[15] E. Vlieg, J. App. Cryst., 33, 401, (2000)

[16] A. F. Wells, Structural Inorganic Chemistry (Oxford University Press, New York, 1984)

[17] C. L. Pang, R. Lindsay, G. Thornton, Chem. Soc. Rev., 37, 2328, (2008)

[18] D. A. Duncan, F. Allegretti, D. P. Woodruff, Phys. Rev. B, 86, 045411, (2012)

[19] E. L. Walle, A. Borg, P. Uvdal, A. Sandell, Phys. Rev. B, 80, 235436, (2009)

[20] P.J. Mller, M. C. Wu, Surf. Sci., 224, 265, (1989)

[21] H. Onishi, K. I. Fukui, Y. Iwasawa, Bull. Chem. Soc. Jpn., 68, 2447, (1995)

[22] C. L. Pang, S.A. Haycock, H. Raza, P.W. Murray, G. Thornton, O. Gulseren, R. J ames, D.W. Bullett, Phys. Rev. B, 58, 1586, (1998)

[23] Tom Woolcot, Thesis Chapter Liquid Water Sorbtion on TiO_2(110), UCL, London

[24] G. Cabailh, X. Torrelles, R. Lindsay, O. Bikondoa, I. Joumard, J. Zegenhagen, G. Thornton, Phys. Rev. B, 75, 241403, (2007)

[25] I. K. Robinson, Phys. Rev. B, 33, 6, 3830, (1986)

[26] R. Shimizu, T. Hitosugi, K.S. Nakayama, T. Sakurai, M. Shiraiwa, T. Hasegawa, T. Hashizume, Jpn. J. Appl. Phys., 48, 125506, (2009)

[27] G. Ketteler, S. Yamamoto, H. Bluhm, K. Andersson, D. E. Starr, D. F. Ogletree, H. Ogasawara, A. Nilsson, and M. Salmeron, J. Phys. Chem. C, 111, 8278, (2007)

Chapter 5

An SXRD study of H_2O adsorption on ZnO $(10\bar{1}0)$: From Monolayer to Beyond Monolayer Coverage

5.1 Introduction

Zinc Oxide (ZnO) in recent years has received much attention due its importance in many technological applications such as catalysis for methanol synthesis [1], as a gas sensor [2] and more recently, as a transparent conductor in dye-sensitised solar cells [3, 4]. In many of these applications water is present and so it is vital to have a deep understanding between the interactions of the molecule with the surface at different coverages.

ZnO crystallises into a hexagonal wurtzite structure which comprises four low Miller index surfaces; the polar (0001) and ($000\bar{1}$) and the non-polar mix terminated ($11\bar{2}0$) and ($10\bar{1}0$) surfaces. The mixed terminated ($10\bar{1}0$) surface, the most energetically favourable surface, consists of an equal number of anions and cations terminated by ZnO 'dimers' separated by trenches. This termination, for which the bulk-truncated surface is shown in Figure 5.1, has been the focus of a number of theoretical [5–7] and experimental [8–10] investigations (see Table 5.1 for summary of results). Unlike other metal oxide surfaces, such as TiO_2 (110), the ZnO ($10\bar{1}0$) surface is virtually defect free, based on STM measurements [11]. In contrast, however, a grazing incidence x-ray diffraction study [8] of the clean ZnO ($10\bar{1}0$) surface, prepared via argon ion sputtering and annealing up to 930°C, found Zn-O vacancies present in the top two layers of the substrate. Furthermore, a large inward relaxation of the surface O was reported such that it occupies a site closer to the bulk than the surface Zn atom. This result is unique to this earlier SXRD study of ZnO ($10\bar{1}0$) and has not been found for any other ($10\bar{1}0$) wurtzite or (110) zinc blende surface structure [5].

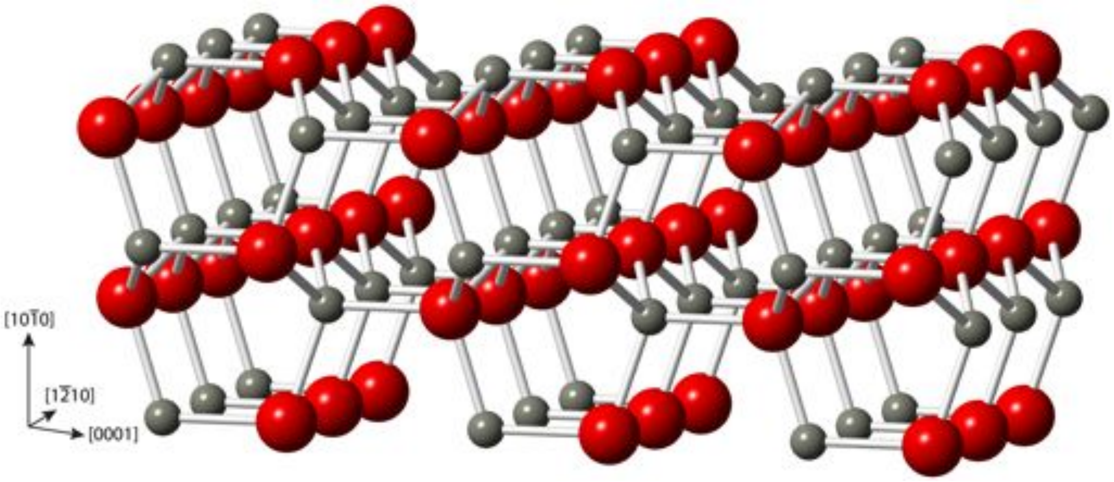

Figure 5.1: Bulk-truncated ZnO(10$\bar{1}$0) surface which consists of an equal number of anions and cations terminated by Zn-O 'dimers' separated by trenches. Large red sphere and small grey spheres are oxygen and zinc atoms respectively.

Table 5.1: A summary of the experimental and theoretical literature investigations on the ZnO(10$\bar{1}$0) surface.

Ref	Techniques	Results
[5]	DFT-LDA, DFT-GGA	Dimer tilt such that Zn atom in uppermost ZnO dimer relaxes closer to bulk than O atom. Significant deviations from bulk structure are seen as deep as five or six layers.
[6]	STM, STS	ZnO dimer vacancies predicted to be the thermodynamically favoured defect type on non-polar (10$\bar{1}$0) surface.
[7]	DFT	First layer O vacancies more stable than second layer O vacancies.
[8]	SXRD	Partial occupancies in top two ZnO layers. Dimer tilt such that O atom in uppermost ZnO dimer relaxes closer to the bulk than Zn atom.
[9]	STM	Well defined rectangular terraces formed. Zn and O atoms form dimer rows running along [1$\bar{2}$10] direction.

An interesting question arises regarding the stability of the ZnO $(10\bar{1}0)$ surface is the interaction of water with the surface. The nature of the interaction has been found to be coverage dependent. A model proposed by Meyer *et al* [12] suggests that at monolayer coverage the surface consists of alternating molecular and dissociated water forming an ordered (2 x 1) superstructure which they termed the mixed half dissociated model, see Figure 5.2. The mechanism of dissociation was concluded to be a self-activating process whereby a neighbouring water molecule would trigger dissociation via hydrogen bonding [12]. Further evidence for partial dissociation is shown in a high-resolution electron energy loss spectroscopy (HREELS) study by Wang *et al* [13]; new losses were seen in the HREELS spectrum when dosing the clean surface with 0.1 L H_2O at 300 K. At a lower coverage of water it has been found that the adsorption can be molecular in nature [14]. This follows from the fact that the water molecules are isolated enough that the trigger for dissociation is not effective. However the authors do conclude that dissociation can occur even at low coverage at elevated temperatures due to the very low adsorption energy differences between molecular and dissociative adsorption. These studies [12–14] suggest that the adsorbed water molecule bonds to the surface Zn atom not in an atop position but slightly shifted to a bridging position such that there is a hydrogen bond between a surface O atom and the H atom of the water molecule. Investigations going beyond monolayer coverage of H_2O on the ZnO $(10\bar{1}0)$ surface are scarce [15, 16]. Raymand *et al* [15], using a ReaxFF reactive force field (FF) and molecular dynamics (MD), found higher surface hydroxylation levels when compared to monolayer coverage. They concluded that this was due to the increased possibility of triggering dissociation from the water phase outside the first monolayer.

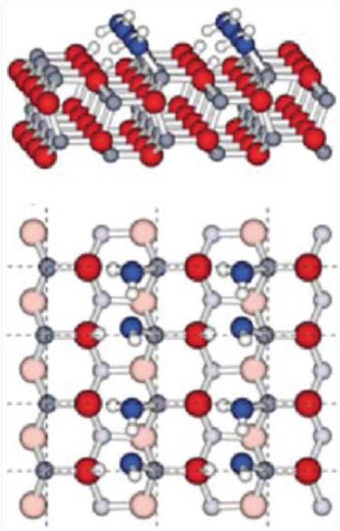

Figure 5.2: A ball and stick representation of the mixed half dissociated model for the ZnO (10$\bar{1}$0) / H_2O interface at monolayer coverage. (a) Perspective view and (b) top view. Large red spheres are oxygen ions, small grey spheres are zinc ions and large dark blue spheres are H_2O/OH molecules. Figure taken from Ref [12].

Although much has been published on the interaction of water with the ZnO (10$\bar{1}$0) surface there is still a need for a full quantitative structural analysis. In order for complete understanding of the water interaction one must ask what influence adsorption, at different coverages, has on the local structure. In this study we investigate the structures of adsorbing water at monolayer and beyond monolayer coverage using scanning tunnelling microscopy (STM) and surface x-ray diffraction (SXRD).

5.2 Experimental Procedure

The ZnO(10$\bar{1}$0) (Pikem) surface (10 mm x 10 mm x 1 mm) was prepared in Ultra High Vacuum (UHV) (base pressure of 10^{-10} mbar) by repeated cycles of argon ion sputtering (5 - 20 min, 1 keV, 45°) and annealing up to 1000°C until a sharp (1 x 1) Low Energy Electron Diffraction (LEED) pattern and characteristic STM images were obtained. Auger Electron Spectroscopy (AES) showed no signs of contamination within the detection limits (Figure 5.3). Not unlike titanium dioxide (TiO_2), the conductivity of ZnO can be qualitatively deduced by its colour. The stoichiometric ZnO($10\bar{1}0$) surface is clear/transparent in colour. However, after heating the sample in UHV it changes to a yellowish colour indicating an increase in conductivity due to the evaporation of oxygen ions.

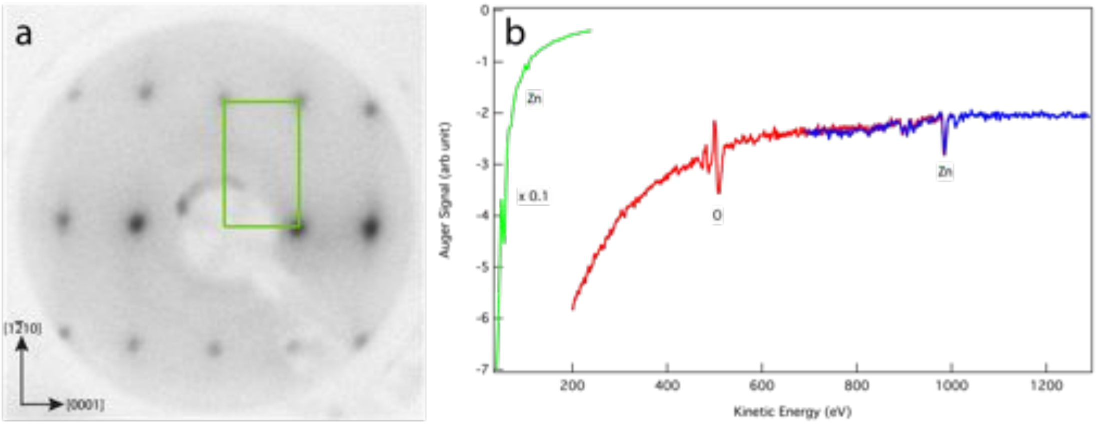

Figure 5.3: (a) LEED image taken at 72.3 eV. Reciprocal unit cell is indicated by green rectangle. Slight streaking the in the [$1\bar{2}10$] crystallographic direction is present (b) AES spectra showing no contamination (C, Ca, K or Ar) within the detection limits.

Initial characterisation of the sample was undertaken at UCL by C. M. Yim using the VT-STM (See Chapter 3.1) where the sample, after being subjected to the cleaning procedure described above, was transferred to the STM chamber (base pressure ~1 x 10^{-10} mbar) and left to cool down to room temperature for ~60 min. A large-area STM image (Figure 5.4a) surface reveals multiple well-defined terraces running along both the [0001] and [$1\bar{2}10$] crystallographic directions. The line profile (Figure 5.4b), which runs along 5 terraces shows step heights of ~1.8 Å and ~3.6 Å corresponding to single and double layer step heights respectively, as illustrated in the ball and stick model in Figure 5.4e. Atomically resolved images were obtained for this surface, showing bright rows in the [$1\bar{2}10$] direction which are assigned to Zn atoms [17]. A unit cell size of 5.2 Å and 3.3 Å was found in the [0001] and [$1\bar{2}10$] direction, respectively (Figure 5.4d, with the model in Figure 5.4f), which is in good agreement with that in the literature [17].

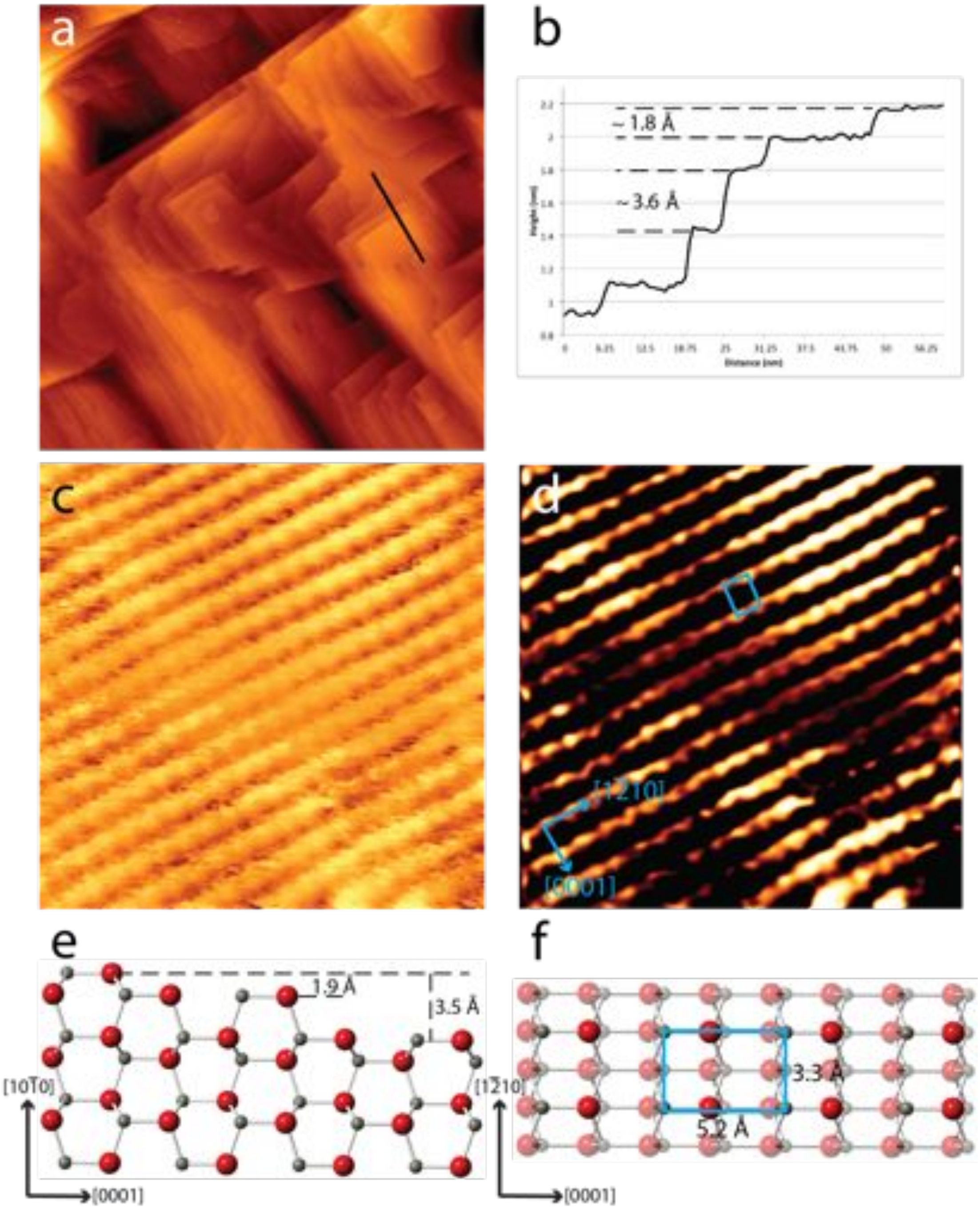

Figure 5.4: STM micrographs of the clean, as-prepared ZnO (10$\bar{1}$0) surface. (a) Large scale STM image (250 nm x 250 nm, V = 2.8 V, I = 0.2 nA). (b) Line profile in the [0001] direction illustrating a range of step heights. (c) Unfiltered atomically resolved STM image. (d) Filtered atomically resolved STM image (5 nm x 5 nm, V = 2.5 V, I = 0.05 nA). Bright rows are assigned to Zn atoms where the unit cell is highlighted by blue rectangle. (e) Cross-section view ball and stick model visualising the terraces represented in (b). (f) Top view ball and stick model showing unit cell of 5.2 Å and 3.3 Å in the [0001] and [1$\bar{2}$10] directions, respectively.

Figure 5.5a displays an atomically resolved STM image of the surface after being exposed to 10 L (5 x 10^{-8} mbar for 200 s) of water. At this coverage (∼1 ML) the water forms well-ordered two-dimensional domains that are of (2 x 1) periodicity. The image in Figure 5.5a is similar to that published in earlier work [12]. The line profile (Figure 5.5b) in the $[1\bar{2}10]$ crystallographic direction shows a doubling of the unit cell to 6.6 Å [12]. It is expected that a (2 x 1) superstructure seen in STM will most likely be equivalent to half monolayer coverage i.e. the water will adsorb on every other Zn site. However, a quantitative XPS study and Car-Parinello molecular dynamics simulations [12] have shown, to the contrary, that water adsorbs to every surface Zn ion and half of the water molecules are dissociated. This is illustrated in Figure 5.5c that shows a top view ball and stick model on the $(10\bar{1}0)$ substrate with alternating rows of associated and dissociated water in the $[1\bar{2}10]$ direction. The authors of the previous work [12] argue that the bright features seen in the STM image with the (2 x 1) overlayer arise from the OH species, more specifically, the direction in which the associated hydrogen atoms point.

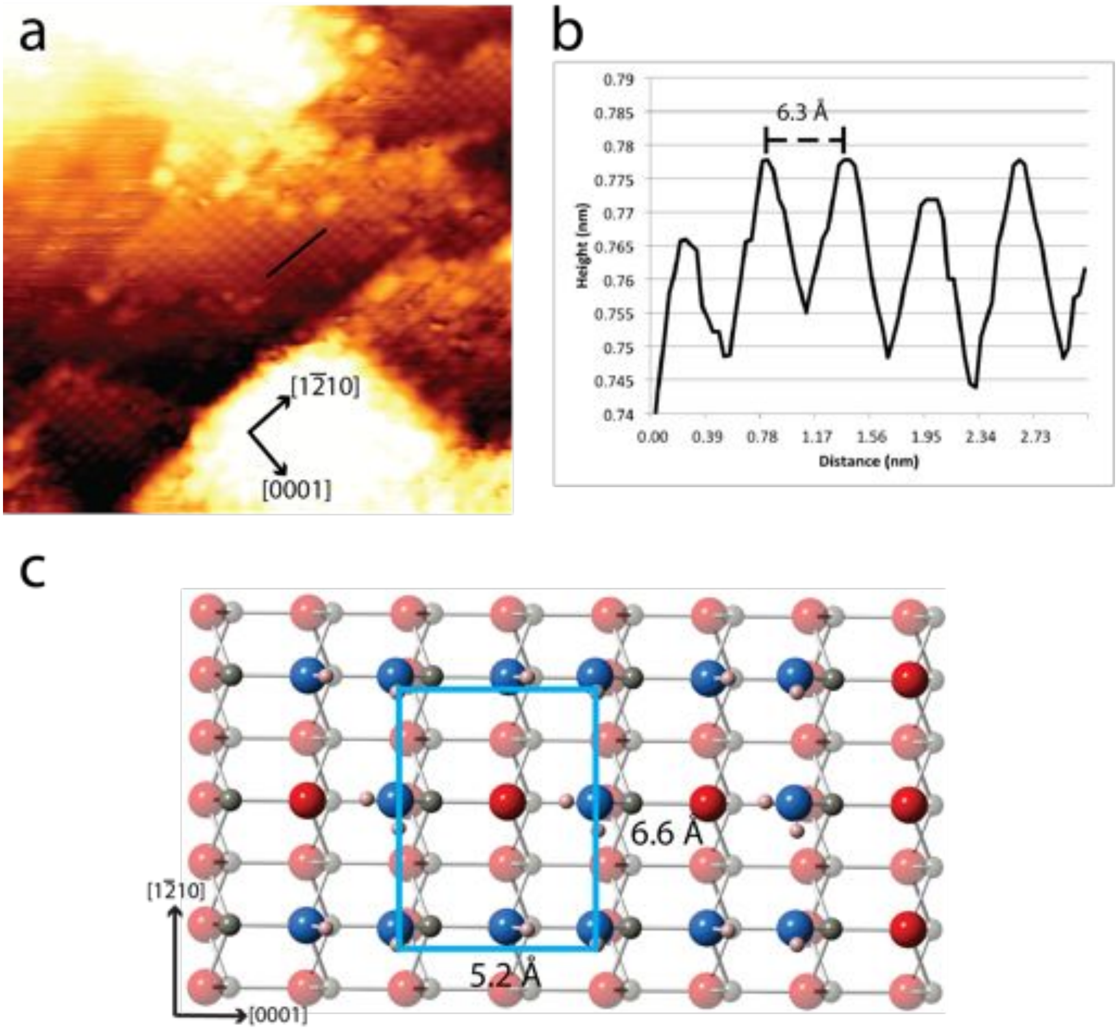

Figure 5.5: STM micrographs of the ZnO $(10\bar{1}0)$ surface after exposure to 10 L of H_2O. (a) Atomically resolved STM image (20 nm x 20 nm, V = 2.5 V, I = 0.2 nA). (b) Line profile in the $[1\bar{2}10]$ direction illustrating the doubling of the unit cell to 6.3 Å. (c) Top view ball and stick model adapted from Ref [12] showing the mixed dissociated (2 x 1) overlayer.

The SXRD experiment was carried out at the ID32 beamline of the European Synchrotron Radiation Facility (ESRF) (See Chapter 3.5.1). Using a similar preparation procedure as described above, characteristic STM images were obtained using the R2P2 UHV system (see Chapter 3.1), see Figure 5.6. After preparation the sample was transferred to a portable, ion pumped, UHV chamber incorporating a beryllium dome shaped window with a base pressure in the 10^{-9} mbar range (see Chapter 3.5.3.1). This was taken to the experimental hutch and directly mounted on the six-circle diffractometer (see Chapter 3.5.2) where SXRD measurements were performed at room temperature, employing a photon energy of 17.7 keV (λ = 0.7 Å). The data are indexed with reference to the (1 x 1) unit cell of the (10$\bar{1}$0) surface, described by lattice vectors (a_1, a_2, a_3), which are parallel to the [1$\bar{2}$10], [0001], and [10$\bar{1}$0] directions, respectively, where $a_1 = c$, $a_2 = a$ and $a_3 = a\sqrt{3}$ (a = 3.249 Å and c = 5.207 Å are the lattice constants of the hexagonal unit cell [18]).

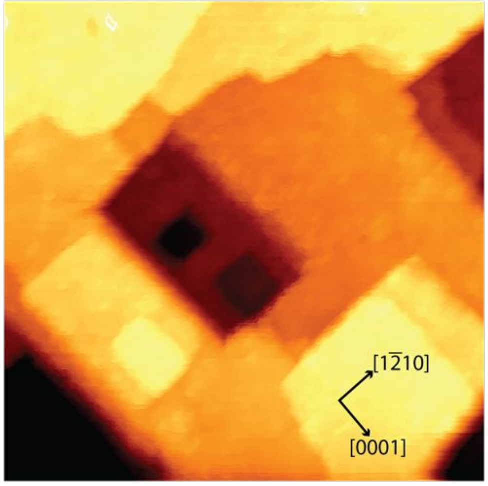

Figure 5.6: An STM image (50 nm x 50 nm, V = 2.8 V, I = 0.2 nA) of ZnO(10$\bar{1}$0) surface taken from the R2P2 UHV system (base pressure = 1 x 10^{-10} mbar) at the ESRF.

The experimental data were collected by measuring the scattered intensities obtained upon rotating the surface around its normal, otherwise known as rocking scans. These data were then integrated and corrected in order to evaluate the structure factors of the different (h,k,l) reflections which when represented versus perpendicular momentum transfer are known as Crystal Truncation Rods (CTRs) [19]. The angle of incidence of the X-rays with respect to the surface was kept constant at 0.3° for all measurements, with 2 x 2 mm^2 slits in front of the detector.

Initially, a large data set of 23 CTRs corresponding to 1087 reflections were collected, which reduced to 818 non-equivalent reflections. These data were collected under nominally UHV conditions, with a base pressure of ~5 x 10^{-9} mbar. Since the background pressure was predominantly H_2O, as measured using an in-situ residual gas analyser, we expect adsorption to arise from the residual water within the vacuum chamber. Next, further diffraction data were recorded for two partial pressures of water, 5 x 10^{-7} mbar and 8 mbar where 10 CTRs and 6 CTRs were collected, respectively. It should be noted that Fractional Order Rods (FORs) were also measured for each condition. Prior to exposure, the ultra pure water went through several freeze-pump-thaw cycles to ensure a contaminant free liquid. An estimation of the water coverage on the ZnO($10\bar{1}0$) surface at high partial pressures of water can be made using the relative humidity (RH); keeping the sample in a constant partial pressure of 8 mbar results in a coverage of ~3 ML [20].

The standard deviations $\sigma_{h,k,l}$ of the structure factor amplitudes $|F_{h,k,l}|$ were evaluated by the squared sum of a systematic error, stated from the measurements of several equivalent reflections to be close to 15% [21]. The analysis of the symmetry-equivalent reflections shows a *pm* plane group symmetry for the measured data. By considering a mirror plane parallel to the a-axis of the unit cell, as experimentally observed from the symmetry analysis between equivalent reflections, a total of 65 parameters were used for the analysis; 48 atomic displacements corresponding to a total of 3 unit cells (12 layers) in the out-of-plane direction, 13 in-plane Debye-Waller parameters, a roughness parameter and a scaling parameter. As we are trying to simulate a near perfect model the occupancies of all atoms were not considered i.e. they were fixed to 1. Representation of a water molecule or hydroxyl in the analysis is in the form of an oxygen atom only due to the low X-ray scattering contribution from hydrogen.

5.3 Results and Discussion

5.3.1 UHV (5 x 10^{-9} mbar)

Initially, structure determination from the SXRD data began with the generally accepted model for clean ZnO ($10\bar{1}0$) (Figure 5.1) to determine whether water adsorption had occurred or not [22]. The best-fit obtained, following the refinement of atomic co-ordinates and the non-structural parameters mentioned above, produced a χ^2 of 1.4. Table 5.2 summarises a comparison of the atomic displacements for the top dimer of the ZnO ($10\bar{1}0$) surface for this experiment and the theoretical calculations in the literature. It was found that the Zn ion of the dimer remains essentially bulk-like with displacements of -0.05 ± 0.01 Å and -0.01 ± 0.01 Å in the out-of-plane and in-plane directions, respectively. However, the O ion experiences a relatively large displacement of 0.10 ± 0.03 Å out-of-plane and 0.10 ± 0.04 Å in-plane. This corresponds to a dimer distance of 2.13 ± 0.04 Å, a 7% expansion from the bulk bond distance (1.99 Å). Clear differences can be seen between this model and that of the theoretical calculations. The latter do not predict an expansion of the dimer bond distance nor do they show that the Zn ion position remains bulk-like.

Table 5.2: A comparison of the atomic displacements in the $[10\bar{1}0]$ direction of the atoms within the uppermost ZnO 'dimer' for the UHV sample with theory for the clean surface. Also shown are the dimer bond distances (d). A positive displacement indicates atom is moving away from the bulk.

Ref/Model	$Zn_\perp$ (Å)	$O_\perp$ (Å)	d (Å)
This work	-0.05 ± 0.01	0.1 ± 0.03	2.13 ± 0.04
[23]	-0.21	0.1	1.864
[24]	-0.33	-0.05	1.83
[25]	-0.255	-0.083	1.905
[26]	-0.32	-0.2	1.83

The next model we used attempted to replicate the best-fit model from the SXRD study in Ref [8]. The first and second layer partial occupancies of the substrate were fixed to 0.77 and 0.90, respectively. As there is no mention of using a roughness parameter or finite Debye-Waller factors in Ref [8] these were set to 0. The best-fit produced a χ^2 of 1.4. An important point to note is that during the analysis it was recognised that the partial occupancies of the top two layers employed in Refcite8 serve in the simulation as a proxy for the high density of steps of the substrate. As a test, all occupancies were fixed to 1 and the roughness parameter was allowed to be free during the fitting procedure. This method produced the same χ^2 of 1.4 and is similar to the clean surface model.

As the clean surface models could not describe the surface, an alternative solution was sought. As described above, the baby chamber had a pressure in the 10^{-9} mbar range and it was shown that the constituents within the chamber mostly comprised of water. It was thus expected that within the time period of beam alignment and measurements the residual water within the chamber would adsorb on the surface. Some evidence to support this argument can be seen in Figure 5.7 which displays ten scans of a reference reflection, (2,0,0.5), measured after each CTR measurement. During data acquisition, the fluctuations in intensity of the reference reflection are the same within the error margins, indicating that the sample had already adsorbed water from the residual in the chamber prior to recording a CTR.

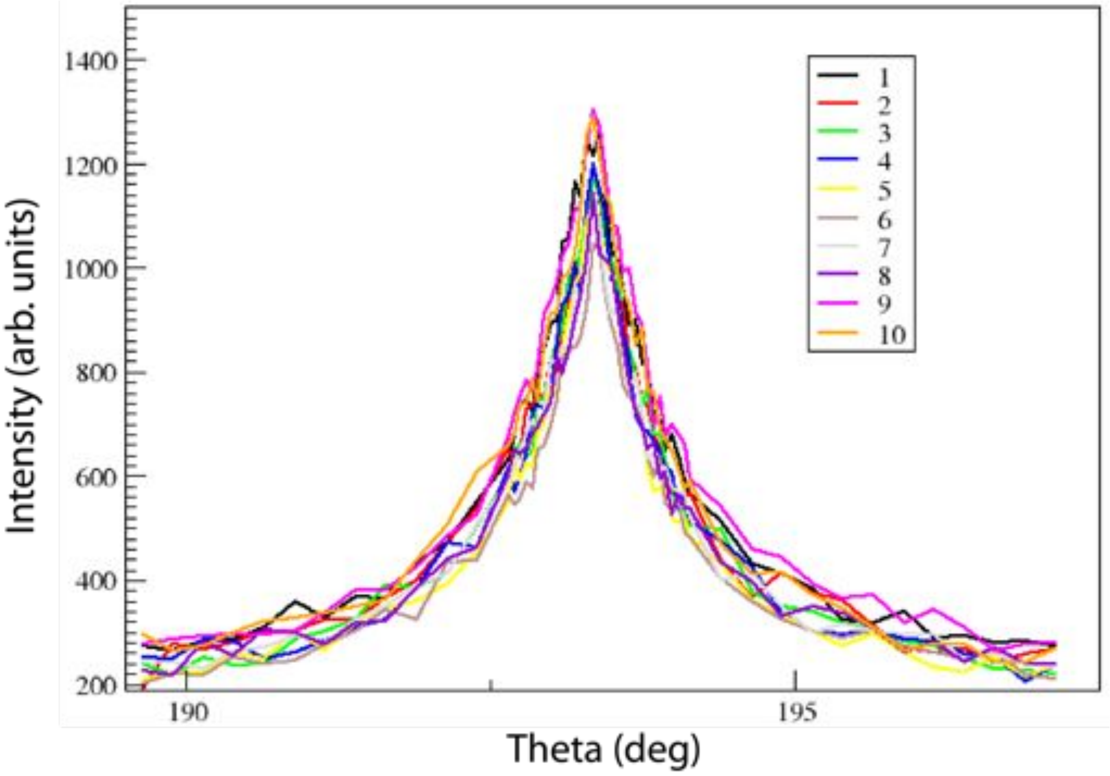

Figure 5.7: Reference scan (2,0,0.5). Only slight changes in intensity are shown between the ten reference scans measured thus showing little to no change occurring during measurements. This gives evidence towards adsorption of water on the sample from the residual in the vacuum chamber.

As mentioned above, STM measurements at ~ML coverage revealed a (2 x 1) ordered overlayer (see Figure 5.5), reproducing the results from Ref [12]. The simplest way to model this superstructure is to assume every other Zn atom in the [1$\bar{2}$10] direction is occupied with an OH/H_2O i.e fixing the occupancy of the OH/H_2O molecule to 0.5. The resulting χ^2 again was found to be

1.4 showing no improvement to the clean surface models. Naturally, the next stage of analysis is to model the mixed part dissociated model deduced from STM measurements [12]. This (1 x 1) model, illustrated in Figure 5.8 produced a χ^2 of 1.2 and an R factor of 20%, a significant improvement from the previous models. This improvement of the χ^2 means that there is a much better agreement between experiment and theory as is visually evidenced in Figure 5.9. It shows the experimental data along with the calculated fits for the CTRs where the black error bars and the solid red line represent the experimental data and the (1 x 1) model, respectively. The differences from the clean surface model are particularly highlighted in the surface dimer where Zn(1) now experiences an outward atomic displacement of 0.04 ± 0.01 Å in the out-of-plane direction and has an in-plane atomic displacement of -0.01 ± 0.01 Å. Similarly, O(1) has atomic displacements of -0.01 ± 0.02 Å and 0.13 ± 0.04 Å in the out-of-plane and in-plane directions, respectively. The location of the H_2O/OH molecule (O(6) in Figure 5.8) is in a slightly shifted atop site bonded to the surface Zn ion with a bond distance of 2.30 ± 0.04 Å and was found to be fully occupied. The dimer distance is 2.13 ± 0.03 Å, with no change from the clean surface model. This expansion of the surface dimer with respect to the bulk, and therefore difference with the literature, can be explained with the electrostatic repulsion between the two negatively charged oxygen ions; one of the surface dimer and one from the adsorbed H_2O/OH molecule.

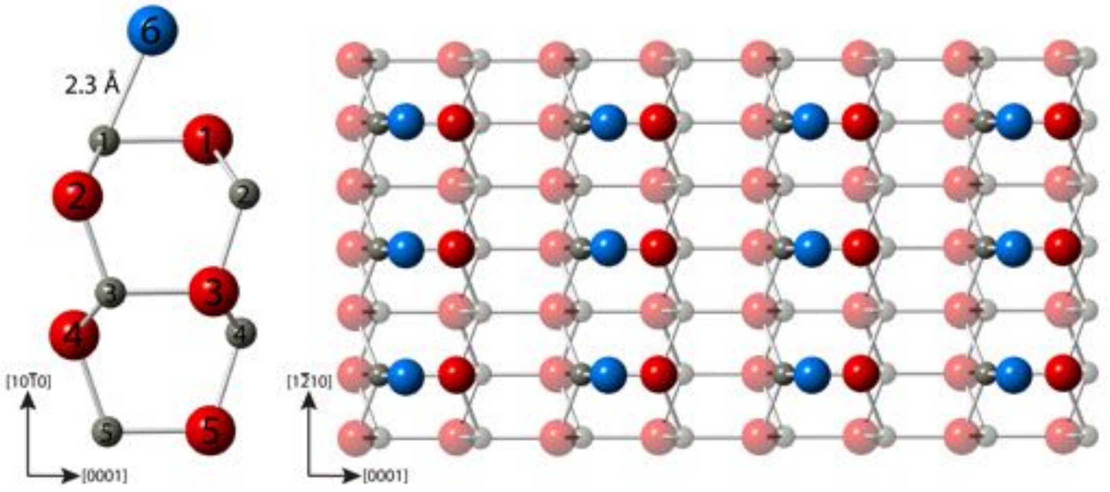

Figure 5.8: A cross-section view and top view of the best-fit ball and stick model of the ZnO (10$\bar{1}$0) surface measured in UHV (5 x 10^{-9} mbar). Large red spheres are oxygen atoms, small grey spheres are zinc atoms and large dark blue are H_2O/OH molecules. O(6) was found to be fully occupied i.e. Every Zn atom is bonded to a H_2O/OH molecule thus representing monolayer coverage. Hydrogen atoms are purposely left out due to their low scattering contribution from X-rays The numbers correspond to atomic displacements listed in Table 5.3.

In a SXRD experiment it is difficult to differentiate between H_2O, OH and the O on the ZnO surface due to the low scattering contribution from hydrogen. Nonetheless, in some cases indirect evidence in the form of bond distances can show whether oxygen is in its atomic, protonated or doubly protonated form. However, in this case we are unable to provide chemical information due to the large error bars associated with the atomic displacements of atom O(6).

It should be noted that the (1 x 1) model is not exactly the same as that presented by Ref [12]. In their model the oxygen of the H_2O/OH molecule is located in the same site as a substrate oxygen would be if the lattice was extended. However, in our model we suggest that the H_2O/OH molecule shifts towards the site bridging between the Zn and O of the surface dimer. Several starting positions for the H_2O/OH molecule were tried and each time this particular site was favoured and produced the best fit. Our model should still produce an STM image characteristic of a (2 x 1) water overlayer.

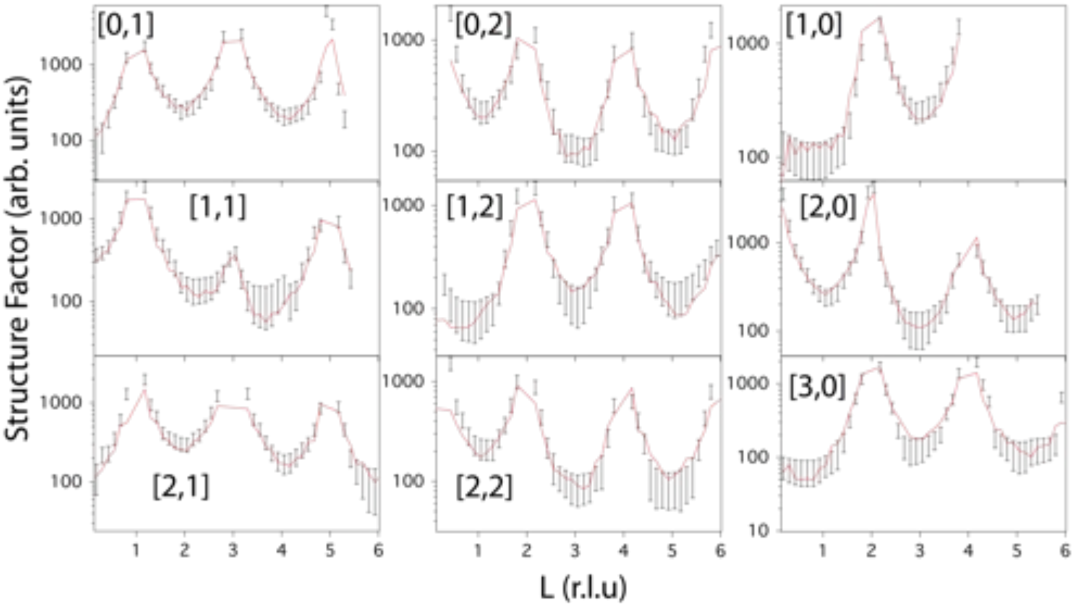

Figure 5.9: Several representative CTRs from the total number of 1087 non-equivalent reflections measured in UHV (5 x 10^{-9} mbar). Black error bars and solid red line are the experimental data and the structure factors calculated for the best fit to the data, respectively.

5.3.2 5 x 10^{-7} mbar H_2O

If SXRD is measured in a background of 5 x 10^{-7} mbar H_2O, we detect a change in the structure of the water overlayer. An atomic site, O(7) (see Figure 5.10), suspected to be a water molecule is now present that has an occupancy of 33 ± 10% and is H-bonded to atom O(6) in some configuration giving a bond distance of 2.50 ± 0.04 Å. Atom O(6) remains unchanged in a slightly shifted atop position from the surface Zn(1) atom, his was anticipated from the experimental CTRs, which are similar to those in UHV, suggesting that the models are similar (see Figure 5.11). Listed in Table 5.3 are the atomic displacements of the top unit cell of the substrate for each of the conditions measured in this investigation. Many of the displacements are in quantitative agreement with that of the measurements made in UHV, however the largest structural change experienced is in the top dimer i.e. Atoms Zn(1) and O(1), where Zn(1) displaces in the same direction but with a larger magnitude when compared to the low coverage condition and O(1) experiences a significant change experiencing both a change in direction and magnitude. As a result, the dimer bond distance has contracted slightly to 2.00 ± 0.03 Å . The best fit for this condition produced a χ^2 of 1.8 and an R factor of 22%.

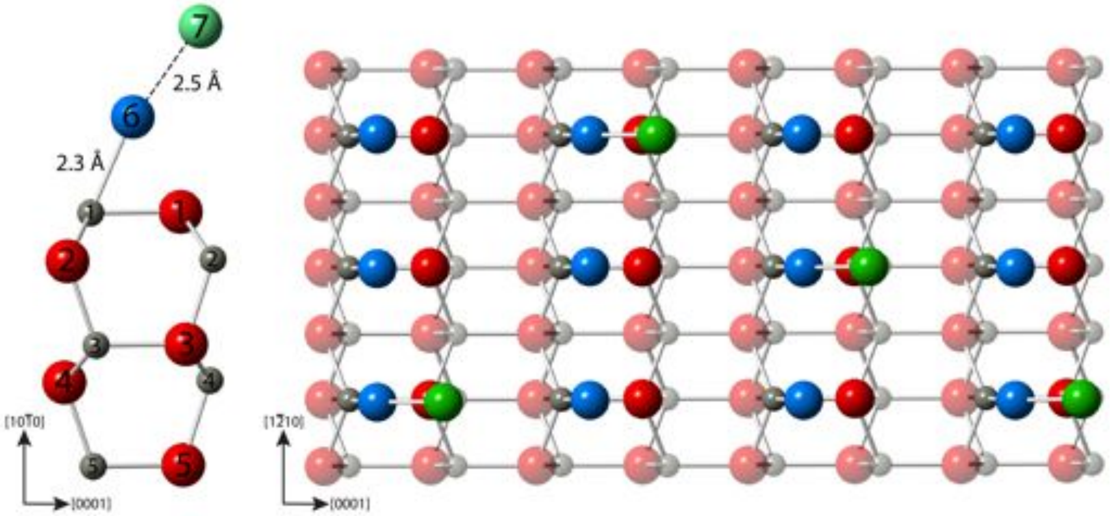

Figure 5.10: A cross-section view and top view of the best-fit ball and stick model of the ZnO (10$\bar{1}$0) / H_2O interface at 5 x 10^{-7} mbar partial pressure. Large red spheres are oxygen atoms, small grey spheres are zinc atoms and large dark blue and green spheres are H_2O/OH molecules. O(6) has the same occupancy and site location as O(6) of the optimised structure found in UHV. O(7) was found to have an occupancy of 33 ± 10%. The numbers correspond to atomic displacements listed in Table 5.3.

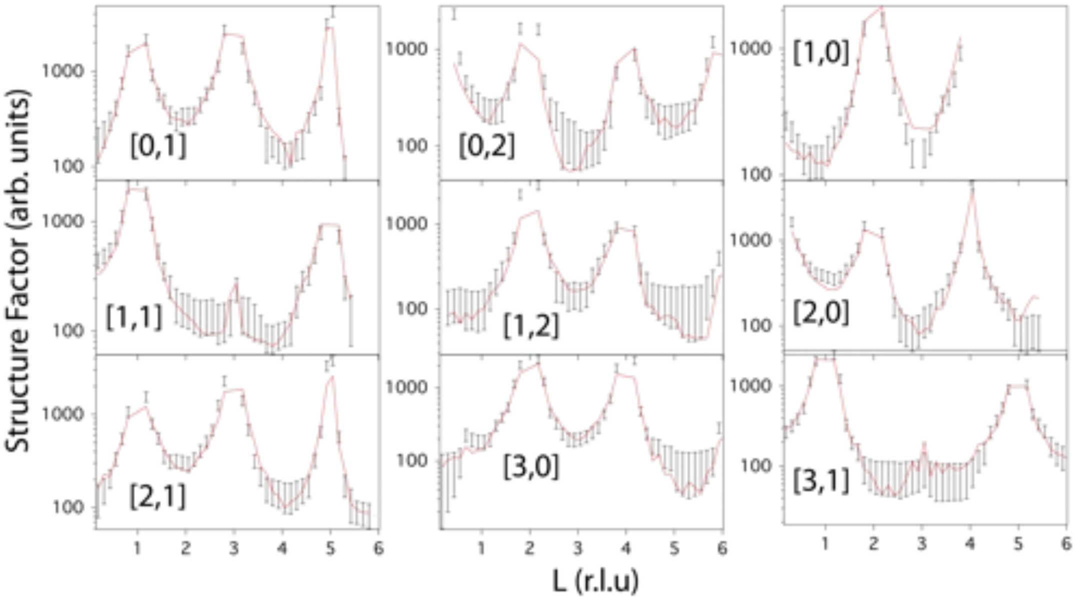

Figure 5.11: Several representative CTRs measured in a constant partial pressure of 5 x 10^{-7} mbar of H_2O. Black error bars and solid red line are the experimental data and the structure factors calculated for the best fit to the data, respectively.

5.3.3 8 mbar H_2O

The best-fit model obtained after exposing the surface to a constant partial pressure of 8 mbar produced a χ^2 of 2.1 and an R factor of 34%. It is illustrated in Figure 5.12 and the CTRs are shown in Figure 5.13. A significant change in the water overlayer is found when compared to the previous conditions; atom O(6) fully occupies a site that is atop of Zn(1) producing a bond distance of 1.9 ± 0.03 Å and atom O(7) has displaced towards the bulk slightly increasing the bond distance between itself and O(6) to 2.6 ± 0.04 Å. Atom O(7) is now fully occupied. As for the substrate atoms, Zn(1) now displaces 0.13 ± 0.02 Å and 0.13 ± 0.04 Å in the out-of-plane and in-plane directions respectively. This represents an increase in magnitude when compared to the previous condition where O(1) displaces -0.10 ± 0.11 Å in the out-of-plane direction and 0.13 ± 0.16 Å in the in-plane direction.

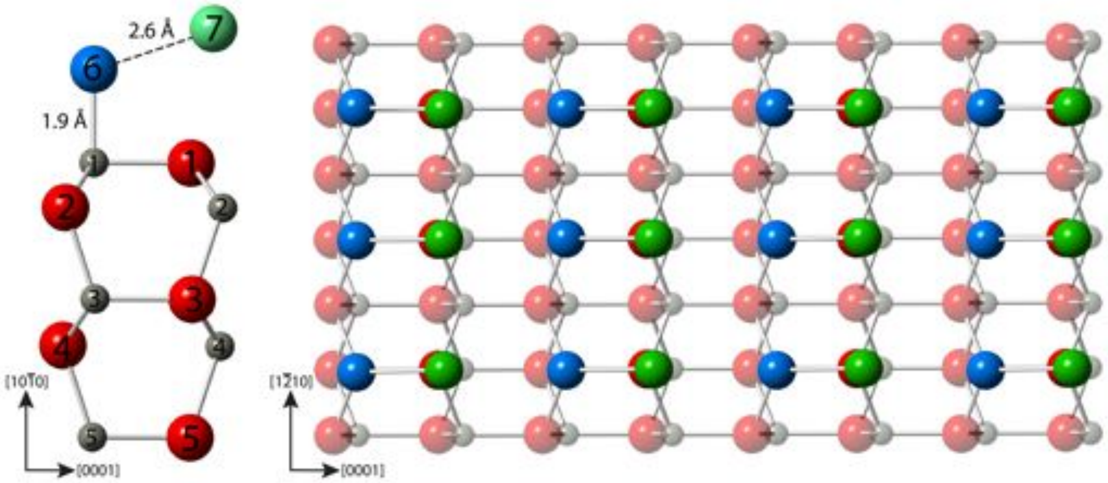

Figure 5.12: A cross-section view and top view of the best-fit ball and stick model of the ZnO (10$\bar{1}$0) / H_2O interface at 8 mbar partial pressure. Large red spheres are oxygen atoms, small grey spheres are zinc atoms and large dark blue and green spheres are H_2O/OH molecules. Atom O(6) has shifted from a bridging position (Figure 5.10) to an atop position above atom Zn(1) and is fully occupied. Atom O(7) is now fully occupied. The numbers correspond to atomic displacements listed in Table 5.3.

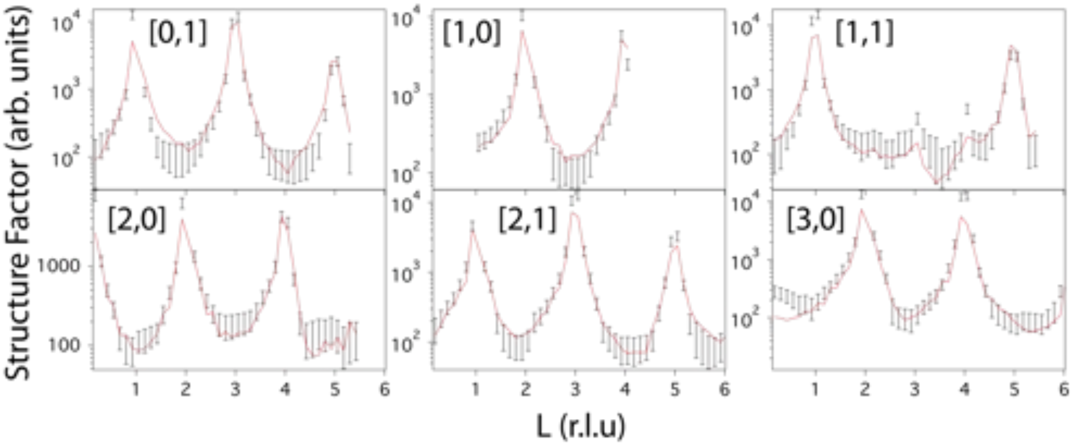

Figure 5.13: Several representative CTRs measured in a constant partial pressure of 8 mbar of H_2O. Black error bars and solid red line are the experimental data and the structure factors calculated for the best fit to the data, respectively.

As mentioned in the introduction, the work described in Ref [15] involved an FF and MD study to investigate multilayer water adsorption and concluded that higher levels of surface hydroxylation occur in the first water layer i.e. the layer that directly adsorbs to the substrate. It is possible that the structural changes found in the present study are a reflection of higher levels of surface hydroxylation at higher partial pressure of H_2O.

Table 5.3: The experimentally determined atomic displacements in the $[10\bar{1}0]$ direction ($d_\perp$) and [0001] direction ($d_{||}$) i.e. normal and parallel to the surface respectively, for UHV and water partial pressures of 5 x 10^{-7} mbar and 8 mbar surface on the ZnO $(10\bar{1}0)$ surface. The atom labels correspond with those seen in Figures 5.8, 5.10 and 5.12. A positive displacement indicates atom is moving away from the bulk.

Atom	UHV (5 x 10^{-9} mbar)		5 x 10^{-7} mbar		8 mbar	
	$d_\perp$(Å)	$d_{\|\|}$ (Å)	$d_\perp$(Å)	$d_{\|\|}$ (Å)	$d_\perp$(Å)	$d_{\|\|}$ (Å)
Zn 1	0.04 ± 0.01	-0.01 ± 0.01	0.08 ± 0.01	0.07 ± 0.01	0.13 ± 0.02	0.13 ± 0.04
O 1	-0.01 ± 0.02	0.13 ± 0.05	0.03 ± 0.05	0.10 ± 0.06	-0.10 ± 0.11	0.13 ± 0.16
O 2	-0.04 ± 0.02	0.12 ± 0.04	0.04 ± 0.05	0.13 ± 0.06	0.04 ± 0.11	0.13 ± 0.18
Zn 2	0.04 ± 0.01	-0.01 ± 0.01	0.03 ± 0.01	0.01 ± 0.01	0.11 ± 0.02	-0.06 ± 0.03
Zn 3	0.05 ± 0.01	-0.02 ± 0.01	0.05 ± 0.01	0.03 ± 0.01	0.04 ± 0.02	0.03 ± 0.03
O 3	0.07 ± 0.03	0.13 ± 0.05	0.06 ± 0.05	0.05 ± 0.07	0.15 ± 0.10	0.13 ± 0.16
O 4	0.07 ± 0.03	-0.10 ± 0.05	0.15 ± 0.07	-0.13 ± 0.07	-0.01 ± 0.08	-0.01 ± 0.16
Zn 4	0.03 ± 0.01	-0.01 ± 0.01	0.01 ± 0.01	0.05 ± 0.01	0.09 ± 0.02	0.01 ± 0.03
Zn 5	0.06 ± 0.01	0.01 ± 0.01	0.03 ± 0.01	0.03 ± 0.01	0.08 ± 0.02	0.07 ± 0.03
O 5	0.01 ± 0.03	0.09 ± 0.04	0.10 ± 0.07	0.10 ± 0.07	-0.02 ± 0.10	0.13 ± 0.17

During the analysis a surface roughness parameter was calculated using the approximated beta model [27]. For the UHV surface, the roughness was found to be 0.5 suggestive of a very rough surface and agrees well with the large scale STM image shown in Figure 5.4a. This increased for the 5 x 10^{-7} mbar condition to 0.6 and a further increase to 0.8 was found after increasing the pressure to 8 mbar partial pressure of water. It is believed that the increase in roughness is not due to a change in the substrate but is a manifestation of the dynamic nature via thermal vibrations of the water overlayer. The increase in disorder is reflected in the error bars associated with the atomic displacements and continuous increase of the R-factor.

5.4 Conclusions

The interaction of H_2O with the ZnO $(10\bar{1}0)$ surface has been investigated as a function of water coverage from monolayer to the multilayer regime. We found that adsorption of water from the residual vacuum produces a (1 x 1) structure consisting of an overlayer that consists of H_2O/OH adsorbates bonded in off tetrahedral sites. Chemical information (H_2O versus OH) could not be obtained due to relatively large error bars on the atomic positions. After exposing the surface to a constant partial pressure of 5×10^{-7} mbar, a second water layer was detected with partial occupancy. Significant changes occurred when exposing the surface to 8 mbar partial pressure of H_2O. The results revealed that the slightly shifted H_2O/OH molecule displaces to a position that is atop of the surface Zn and the second water layer is now fully occupied. Accompanying the increase in water coverage is an increase in surface disorder, partly due to the rough nature of the ZnO $(10\bar{1}0)$ surface and partly because of the dynamic nature of the water overlayer.

Very few experimental studies have been performed on multilayer water adsorption on the ZnO$(10\bar{1}0)$ surface, in stark contrast to sub-monolayer to monolayer water adsorption. The main avenue of future research in this area will be to further investigate multilayer adsorption of water on the surface using experimental techniques such as ambient pressure XPS. This technique up until recently was restricted to studies in/near UHV but was partially overcome by the development of a differentially pumped electron analyser and so ideal for gaining rich chemical information of surfaces in environments similar to the applications in which the material is used in. The technique is well suited to furthering the research reported in this chapter; chemical information, which could not be obtained here, can be gained in the water contact layer to confirm the partial dissociation of water molecules but more importantly may be able to identify if the contact layer changes at higher partial pressures of water. Furthermore, similar experiments reported for the water/$TiO_2(110)$ system could be applied to the ZnO$(10\bar{1}0)$ surface i.e liquid water adsorption. It would be interesting to see if the structures remain the same as in the case of $TiO_2(110)$.

References

[1] M. Behrens, F. Studt, I. Kasatkin, S. Khl, M. Havecker, F. Abild-Pedersen, et al., Science. 336, 893, (2012)

[2] L. Wang, Y. Kang, X. Liu, S. Zhang, W. Huang, S. Wang, Sensors Actuators B Chem. 162, 237, (2012)

[3] J.A. Anta, E. Guillen, R. Tena-Zaera, J. Phys. Chem. C., 116, 11413, (2012)

[4] J. Chen, R. E. Ruther, Y. Tan, L. M. Bishop, R. J. Hamers, Langmuir., 28, 10437, (2012)

[5] B. Meyer, D. Marx, Phys. Rev. B., 67, 035403, (2003)

[6] R. Kovacik, B. Meyer, D. Marx, Angew. Chem. Int. Ed., 46, 4894, (2007)

[7] A. Wander, N. M. Harrison, Surf. Sci., 529, L281, (2003)

[8] N. Jedrecy, S. Gallini, M. Sauvage-Simkin, R. Pinchaux, Surf. Sci., 460, 136, (2000)

[9] O. Dulub, L. Boatner, U. Diebold, Surf. Sci., 519, 201, (2002)

[10] W. A. Tisdale, M. Muntwiler, D. J. Norris, E. S. Aydil, X. Y. Zhu, J. Phys. Chem. C., 112, 14682, (2008)

[11] T. M. Parker, N. G. Condon, R. Lindsay, F. M. Leibsle, G. Thornton, Surf. Sci., 415, L1046, (1998)

[12] B. Meyer, D. Marx, O. Dulub, U. Diebold, M. Kunat, D. Langenberg, C. Woll, Angew. Chem. Int. Ed., 43, 6641, (2004)

[13] Y. Wang, M. Muhler, C. Woll, Phys. Chem. Chem. Phys., 8, 1521, (2006)

[14] Y. Yan, M. M. Al-Jassim, Phys. Rev. B., 72, 235406, (2005)

[15] D. Raymand, A. C. T. van Duin, W. A. Goddard, K. Hermansson, D. Spangberg, J. Phys. Chem. C., 115, 8573, (2011)

[16] D. Raymand, T. Edvinsson, D. Spangberg, A. van Duin, K. Hermansson, Proc. Spie., 7044, 70440E, (2008)

[17] X. L. Yin, A. Birkner, K. Hanel, T. Lober, U. Kohler, C. Woll, Phys. Chem. Chem. Phys., 8, 1477, (2006)

[18] V. A. Coleman and C. Jagadish, Zinc Oxide Bulk, Thin Films and Nanostructures: Processing, Properties and Applications (Chapter 1, 2011)

[19] E. Vlieg, J. Appl. Crystallogr. 30, 532, (1997)

[20] G. Ketteler, S. Yamamoto, H. Bluhm, K. Andersson, D. E. Starr, D.F. Ogletree, H. Ogasawara, A. Nilsson, M. Salmeron., J. Phys. Chem. C., 111, 8278, (2007)

[21] I. K. Robinson, Handbook of Synchrotron Radiation (North Holland, Amsterdam, (1991) Vol. 3.

[22] C. Woll, Prog. Surf. Sci., 82, 55, (2007)

[23] M. J. S. Spencer, K. W. J. Wong, I. Yarovsky, Mater. Chem. Phys. 119, 505, (2010)

[24] D. J. Cooke, A. Marmier, S. C. Parker, J. Phys. Chem. B., 110, 7985, (2006)

[25] A. Wander, N. M. Harrison, Surf. Sci., 457, L342, (2000)

[26] P. Schroer, P. Kruger, J. Pollmann, Phys. Rev. B., 49, 17092, (1994)

[27] I. K. Robinson, Phys. Rev. B., 33, 3830, (1986)

Chapter 6

A Quantitative Structural Investigation of the H_2O / 0.1 wt% Nb-$SrTiO_3$ (001) Interface

6.1 Introduction

$SrTiO_3$ (STO) has received much attention over the years because of its importance in many applications such as photocatalysis [1], as a gas sensor [2] and as an anode for solid oxide fuel cells [3]. Water is arguably the most important adsorbate to investigate as in many applications of STO it is either purposely or inadvertently exposed to the surface. Even in controlled conditions (such as Ultra High Vacuum (UHV)) water is usually one of the most abundant constituent in the residual and so a great deal of importance is placed on understanding its interactions with the STO surface. Hence it has been the subject of a number of investigations [4-6]. STO crystallizes into the cubic perovskite structure that is made up of alternating layers of TiO_2 and SrO, as shown in Figure 6.1. Depending on the preparation procedure, a mixed terminated or a singly terminated surface can be achieved for the (001) orientation. The general consensus of the literature is that water dissociates on the SrO termination whereas molecular adsorption is preferred on the TiO_2 termination. A study by Iwahori *et al* [7] using friction force microscopy was able to image the mixed terminated surface before and after exposure to several partial pressures of water. They concluded that changes in the friction force were only visible for the SrO terminated surface, being due to surface hydroxylation.

Several theoretical investigations have provided further evidence for the different adsorption modes seen in experimental work. A density functional theory (DFT) study by Baniecki *et al* [8] found that the most favourable adsorbate configuration for the (1 x 1) SrO terminated surface in a partially dissociated structure, whereas on the TiO_2 terminated surface molecular adsorption was favoured. These findings have been corroborated by other publications [9, 10]. Much of our understanding with the interaction of water with STO is at monolayer or sub-monolayer coverage and as far as we are aware there have been no quantitative experimental investigations of the structure at the STO(001) interface with liquid water. The main aim of this chapter is to provide a quantitative structural analysis of the STO(001) / liquid H_2O interface using surface x-ray diffraction (SXRD). We also demonstrate that with our particular preparation procedure we obtain a titanium-rich mixed terminated surface. We explore the effects of water adsorption on the structure of both surface terminations.

6.2 Experimental Procedure

The experiments were carried out at the ID32 beamline of the European Synchrotron Radiation Facility (ESRF) [11]. The X-ray measurements were performed with the samples at room temperature using a monochromatic focused beam with an energy of 17.7 keV (λ = 0.7 Å), defined by slits to a size of (200 μm x 20 μm). The surface (7 mm x 5 mm) of the 2 mm thick STO (001) sample (0.1 wt% Nb, Crystal GmbH, Berlin) underwent ultrasonic cleaning in acetone after which it was rinsed with de-ionised water. It was mounted to a Mo backplate via spot welding with Ta clips and inserted into the UHV chamber (base pressure of 10^{-10} mbar). In order to produce a well-ordered clean surface, repeated cycles of argon ion sputtering (1 keV, 10 mA, 45°) and annealing up to 700°C in an O_2 partial pressure of 1 x 10^{-2} mbar were performed until a sharp (1 x 1) Low Energy Electron Diffraction (LEED) pattern was obtained. Auger Electron Spectroscopy showed no signs of contamination within the detection limits. After preparation, the sample was transferred to a small, portable, ion pumped UHV chamber (baby chamber) with a base pressure in the 10^{-9} mbar range. It features a cylindrical shaped beryllium window, which allows unrestricted transmission of the incident and reflected X-ray beams [12] (see Chapter 3). It was taken to the experimental hutch and directly mounted on the six-circle diffractometer for the surface X-ray diffraction measurements. The STO(001) cubic surface unit cell was described by the lattice vectors (a, b, c) parallel to the [100], [010] and [001] directions, respectively, where a and b lie in the surface plane and c is perpendicular to the surface (a = b = c = 3.905 Å).

The angle of incidence of the X-ray beam with respect to the surface was kept constant at 0.3° for all measurements with 2 x 2 mm^2 slits, in front of the detector, at 1 m from the beamspot on the sample. The experimental data was collected by measuring the scattered intensities obtained upon rotating the surface around its normal, otherwise known as rocking scans. This data was then integrated and corrected in order to evaluate the structure factors of the different (h,k,l) reflections which when represented versus perpendicular momentum transfer are known as Crystal Truncation Rods (CTRs) [13].

A large data set of 20 CTRs for the as-prepared surface was measured. Immediately after, the baby chamber was vented with and kept in a constant flow of nitrogen to ensure limited surface contamination for when an electrochemical droplet cell for controlled water exposure was installed (see Chapter 3.5.3.2). The ultra pure water used went prior to exposure through several freeze pump thaw cycles to ensure a contaminant free liquid. Together, with the use of a computer controlled pumping system and endoscope a small droplet of approximately 2 mm in diameter was carefully brought into contact with the sample surface creating a meniscus [12]. A further 13 CTRs were measured in these conditions. To determine any possible residual effects on the surface due to the adsorption of water, 10 CTRs were measured after removal of the water droplet by drying with a flow of nitrogen. A comparison of the experimental structure factors is shown in Figure 6.2. The black, red and green error bars are the clean, water adsorbed and nitrogen flow structure factors respectively. It should be noted that Fractional Order Rods (FORs) were also investigated for each condition but no intensity was found. From the analysis of the experimental data for each condition, the standard deviations $\sigma_{h,k,l}$ of the structure factor amplitudes [F$_{h,k,l}$]were evaluated by the squared sum of a systematic error, estimated from the measurements of several equivalent reflections to be close to 12% [14]. The analysis of the symmetry-equivalent reflections shows the same p4mm plane group symmetry for each of the three measured data sets.

The experimental data were tested against model surface structures with a set of free parameters (see below) using a version of the program ROD that utilises a least squares refinement procedure (See Chapter 2.4.4).

6.3 Results and Discussion

6.3.1 UHV Surface

The starting point for the structure determinations was the two possible bulk, i.e. TiO_2 and SrO terminated surfaces of the STO (001) substrate. Structure factors for both surfaces were computed assuming a single termination with fully occupied atomic positions. However, both produced a poor fit to the experimental data having a minimum χ^2 value of 3.3. After different tries a model was fit to the data consisting of a surface with both types of termination. A total of 82 free fitting parameters were used for the analysis. Allowing displacements, i.e. fitting the z-component of the position of all atoms to a depth of 6 unit cells (12 atomic layers) for the TiO_2 terminated terrace and 5.5 unit cells for the SrO terminated terrace, resulted in 65 parameters.

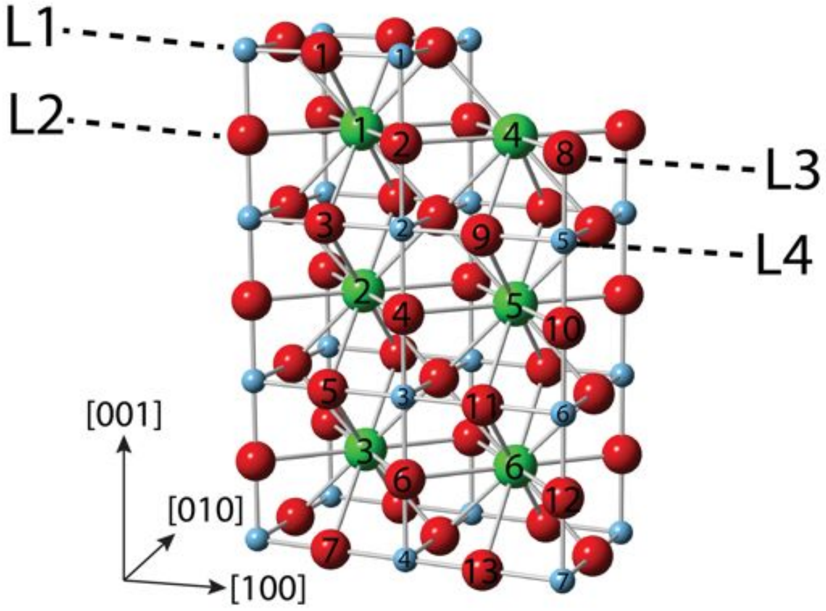

Figure 6.1: Ball and stick model representation of the clean surface with two terminations, TiO_2 and SrO, found in this study. Small light blue, large red and largest green spheres are titanium, oxygen and strontium atoms respectively. The labelled layers (L1, L2, L3, and L4) are the same as used in Table 6.1. The numbering of the Ti, Sr, and O atoms is the same as used in Table 6.2 and **??**.

Taking into account disorder in-plane gave ten (static) Debye-Waller parameters and five parameters allowing for partial occupancy of SrO and TiO_2 in the first two atomic layers. Finally, we allowed for roughness and introduced a scaling parameter. A χ^2 value of 1.0 and R-value 0.12 was produced which proves the excellent agreement between the experimentally measured and calculated structure factors, visually evidenced in Figure 6.3.

Figure 6.1 schematically displays the main features of the final best-fit structure. It is comprised of two terraces, with the one being terminated by TiO_2 and the other one by SrO. The TiO_2 termination is shown higher (half unit cell corresponding to 1.9 Å) in the [001] direction and the small blue, larger red and largest green atoms represent titanium, oxygen and strontium respectively. The contribution from each terrace to the scattering signal is considered to be incoherent meaning that the surface is populated with both terminations over large areas. It should be noted that when adding the scattering contributions from both terraces coherently, the

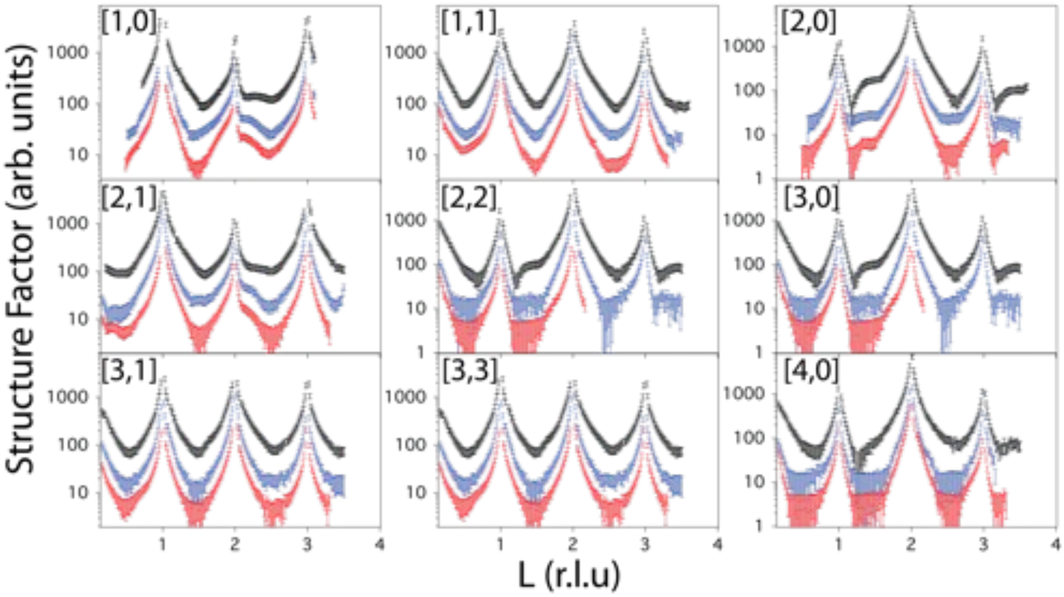

Figure 6.2: Comparison of experimental structure factors for the different conditions measured; clean (UHV), water adsorbed and nitrogen flow-dried surface are black (top), blue (middle) and red (bottom) error bars, respectively. Profiles are offset for clarity.

fit gets much worse producing a best χ^2 value of 4.4. The surface coverage of each terrace was experimentally determined to be 50% from the refinement procedure. It has been shown that the surface percentage coverage of TiO_2 and SrO terminations for the (1 x 1) surface is heavily dependant on the preparation procedure [18, 19]. In the present study, where the sample was prepared via argon ion sputtering and annealing in oxygen (1 x 10^{-2} mbar) to moderate temperature (700°C), the surface coverage of each TiO_2 and SrO termination was found to be 68% and 32%. This follows from the one to one ratio of both terraces as mentioned above, additionally taking into account the partial occupancies of the two topmost layers from each terrace as given in Table 6.1. Furthermore, the roughness parameter was found to be $\beta = 0.2$ which reflects the fractional occupancies of the terraces (for a very smooth and very rough surface $\beta = 0$ and $\beta = 1$, respectively). The atomic displacements of the first two atomic layers from both terminations of the best-fit model of this study and that of others in the literature [9, 17, 18] are listed in Table 6.2, with the atom labels corresponding with those used in Figure 6.1.

Its been suggested by Ravikumar *et al* [17] that lateral displacements are present in the SrO ter-

Table 6.1: Occupancies of the first two atomic layers for each termination of the $SrTiO_3$(001) substrate. The layers correspond to Figures 6.1 and 6.4. Occupancies apply to all conditions measured in the experiment.

Terrace termination	Layer	Occupancy
T1: TiO2	L1 (TiO2)	0.29
	L2 (SrO)	0.43
T2: SrO	L3 (SrO)	0.13
	L4 (TiO2)	0.64

Table 6.2: Comparison of the atomic displacements in the [001] direction (out-of-plane) between the UHV prepared mix terminated STO(001) surface from this work, [14], [15] and [9]. The atom labels correspond with those seen in Figure 6.1. A negative value indicates an atom displacing towards the bulk. Also shown are is the TiO_2/SrO ratio for each of the experimental work. ’*’ indicates very large error up to 50%. Ref [15] has an average error of ± 0.02 Å.

Termination	Atom	Atomic Displacements (Å)				
		This Work (68:32)	SXRD [14] (78:22)	SXRD [15] (66:33)	[9]	
					Force-Field	B3LYP
TiO_2	Ti(1)	-0.12 ± 0.02	0.00 ± 0.03	-0.02	-0.15	-0.11
	O(1)	-0.23 ± 0.06	-0.5 ± 0.3	-0.37	-0.08	-0.03
	Sr(1)	-0.06 ± 0.00	-0.01 ± 0.01	-0.01	0.09	0.14
	O(2)	0.04 ± 0.02	0.2 ± 0.1	0.39	-0.01	0.00
SrO	Sr(4)	0.10 ± 0.01	-0.25 ± 0.07	0.09	-0.12	-0.22
	O(8)	0.27 ± 0.05	-0.3 ± 0.4	0.2*	0.05	0.01
	Ti(5)	0.09 ± 0.01	-0.24 ± 0.07	0.2	0.07	0.06
	O(9)	-0.08 ± 0.02	-0.4 ± 0.7	-0.37	0.06	0.03

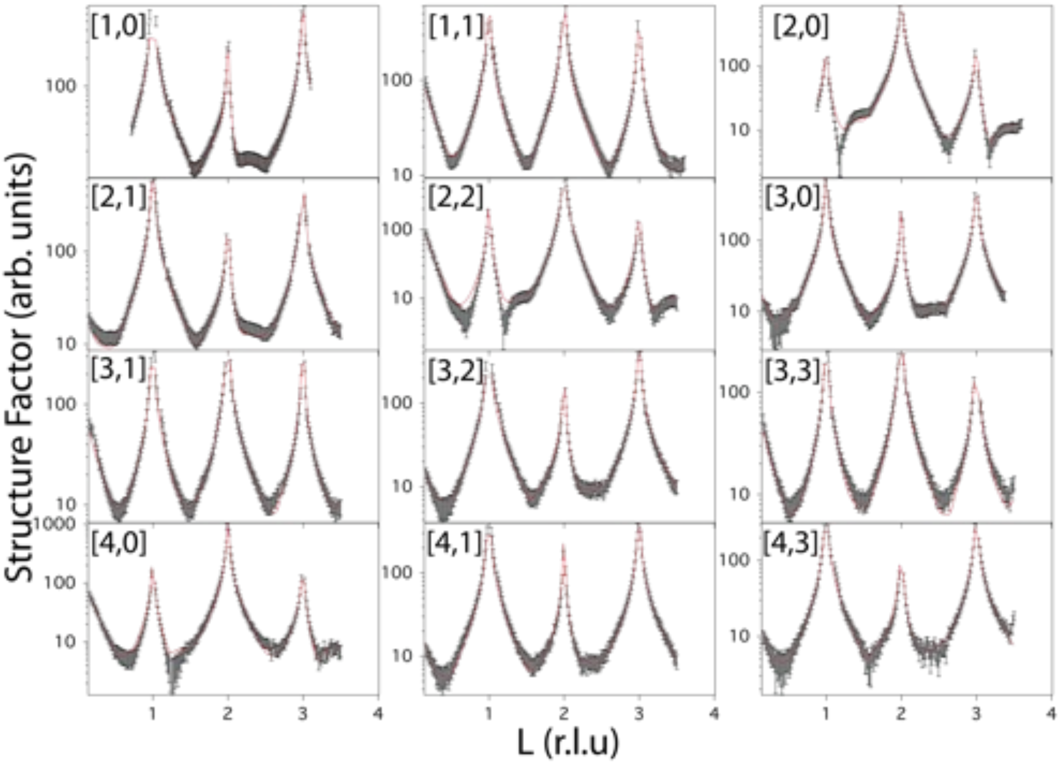

Figure 6.3: Best-fit to the CTRs for the UHV-SrTiO$_3$(001) surface. Black error bars and solid red line are experimental and calculated structure factors (best-fit), respectively.

mination of the substrate thus breaking the four-fold symmetry. However, the fact that LEED produced a clear (1 x 1) pattern and no FORs were found suggests that the surface was not reconstructed under our preparation conditions. Consequently, the cations were only permitted to move along the [001] direction. This maintains the *p4mm* symmetry of the surface.

When comparing our findings with other results reported in the literature, it is quite clear from Table 6.2 that the atomic displacements given in Ref [16] agree best with our study overall, where the atomic shift directions from the two topmost layers of both terraces, T1 and T2, are identical. Moreover, this agreement is especially highlighted for Sr(4) of the SrO terminated terrace which in the earlier work is found to displace away from the bulk by 0.09 ± 0.02 Å similar to the displacement of 0.10 ± 0.01 Å found in here. In contrast, the two other studies [9, 18] find a strong negative displacement, i.e. toward the bulk. Except for Ti(5), the displacements of the cations given in Ref[16] are slightly smaller though the general trend is similar to our results.

Similarly, for the TiO_2 terminated terrace the atomic positions given in Ref [16] match better with our values than from the other two publications. For both terminated terraces, both cations displace in the same direction with a similar magnitude as found here, i.e. inwards for the TiO_2 terminated terrace and outward for the SrO termination. As regards the anions, the results presented here and in Ref[16] show that O(1) exhibits a much larger displacement whereas O(2) displaces much less in our case. For both terraces both oxygens relax in opposing directions: inward for O(1) and outward for O(2); outward for O(8) and inward for O(9). In this respect, too, only the results published in Ref[16] are in reasonable agreement with our findings.

The lack of agreement with the results from Ref [15] for the atomic positions of the TiO_2 terminated terrace is notable. However, our results are in striking disagreement regarding the SrO terminated terrace. This is especially the case for Sr(4) of the SrO terminated surface, which displaces in the opposite direction. Similarly pronounced is the disagreement for the other atomic positions of the SrO terminated terrace. Large inward displacements are reported for all atoms of the SrO terrace in Ref [15] whereas we find that Sr(4), Ti(5), and O(8) all displace outward by 0.10 ± 0.01 Å, 0.09 ± 0.01 Å, and 0.27 ± 0.05 Å, respectively. We find only for O(9) an inward-displacement but with a much smaller magnitude than listed in Ref [15].

Neither of the two calculations from the theoretical study by Evarestov *et al* Ref [9] shows reasonable agreement with the present or any of the other two experimental studies, except for Ti(1) in the TiO_2 terminated terrace. Large differences in the relaxation are seen with all other atoms in this termination, particularly for Sr(1) and O(2). Similarly, discrepancies are seen for the SrO terminated terrace, with Sr(4) and O(9) shown to displace in directions opposite to those found here.

One possible reason for the reasonable agreement between the results of this study and Ref [16] and poor agreement with Ref [15] may be the preparation method, which strongly influences the TiO_2/SrO termination ratio and structure of the surface [18, 19]. In Ref [16] the authors studied several samples prepared in different ways. The displacements shown in Table 6.2 were found for a sample that was given a final annealing in 0.1 mbar O_2 at 700°C after etching and annealing in a tube furnace. For this sample it was reported that it had a ratio of 66:33 of TiO_2/SrO terminated surface areas. Although it showed a (2 x 2) reconstruction, the TiO_2/SrO ratio is closer to the ratio for the sample of this study whereas the sample of Ref [15], prepared by sputter/annealing (900 K) cycles, had a ratio of 78:22 TiO_2/SrO.

An important question to answer is whether the perfect, ideal termination of the STO(001) (1 x 1) surface exists. Early experimental work, such as a combined LEED and AR-XPS investigation [20] on the Ti-rich surface, suggest that it does not. They found that the unreconstructed p(1 x 1) STO(001) surface, terminated with a TiO_2 layer and obtained by simple chemical etching, is always accompanied by oxygen vacancies. These findings are in agreement with several X-ray and electron scattering experiments [21-23] that detect the presence of oxygen vacancies and surface buckling. It is surprising, given the stability of the (1 x 1) surface, that there is a scarcity of atomically resolved images displaying the coexistence of TiO_2/SrO terraces (step height ∼2 Å). This is perhaps due to the dependence on surface preparation and hence could limit their stability in UHV conditions [24]. Using a new approach to surface preparation, in-situ fracturing of STO at room temperature, Guisinger *et al* [25] observed the coexistence of TiO_2/SrO terraces using cross-sectional STM. As regards to the electronic structure, the formal valences of Ti^{4+}, Sr^{2+}, and O^{2-} of the STO(001) surface would not be polar. However, the real valences are considerably different [26, 27], resulting in an excess of negative and positive charge on the TiO_2 and SrO planes, respectively. The electrostatic charge of the order of $\pm$ 0.5 e_0 is rendering the (001) axis (weakly) polar, contrary to simple expectations. As a consequence, the ideal SrO or TiO_2 terminated surfaces of $SrTiO_3$(001) cannot be stable and must relax or reconstruct as shown by the calculations and experimental work. Surface roughness and/or changes in the stoichiometry, as observed in the present study, will also contribute to a lowering of the electrostatic energy. However, these modifications, which will also depend on specific preparation procedures, would be very difficult to take into account by total energy calculations.

6.3.2 STO(001) in Contact with Water

As mentioned above, quantitative experimental investigations of the STO (001) / H_2O interface are quite scarce. On the other hand, several theoretical investigations [4, 6, 8, 9, 10, 20] have been conducted. The general consensus seems to be that water adsorption is more reactive on the SrO terminated surface leading to molecular and dissociative adsorption. In contrast, only molecular adsorption occurs on the TiO_2 termination. Following from the structure determined for the clean surface, we started the analysis with positioning H_2O/OH molecules on both terminations. There was no change in the TiO_2/SrO ratio indicating that water adsorption has little effect on the stoichiometry of substrate surface. Furthermore, the occupancies of the TiO_2 and SrO in the first layers were exactly the same as for the clean surface, while the roughness parameter increased to 0.4 from 0.2 for the clean surface. The oxygen atom of the H_2O/OH was allowed the freedom to displace in-plane, in both the [010] and [100] crystallographic directions. After attempting several different sites, the most favoured found for the TiO_2 terminated terrace is atop titanium. For the SrO terminated terrace, the favoured position is the same as that which an oxygen atom would occupy if the perovskite lattice were extended. This agrees well with the literature [9, 10, 28]. The best-fit model is shown in Figure 6.4 and produced a χ^2 value of 1.4 and R-value of 0.16. This indicates a very good agreement between experiment and model, as visually evidenced in Figure 6.5.

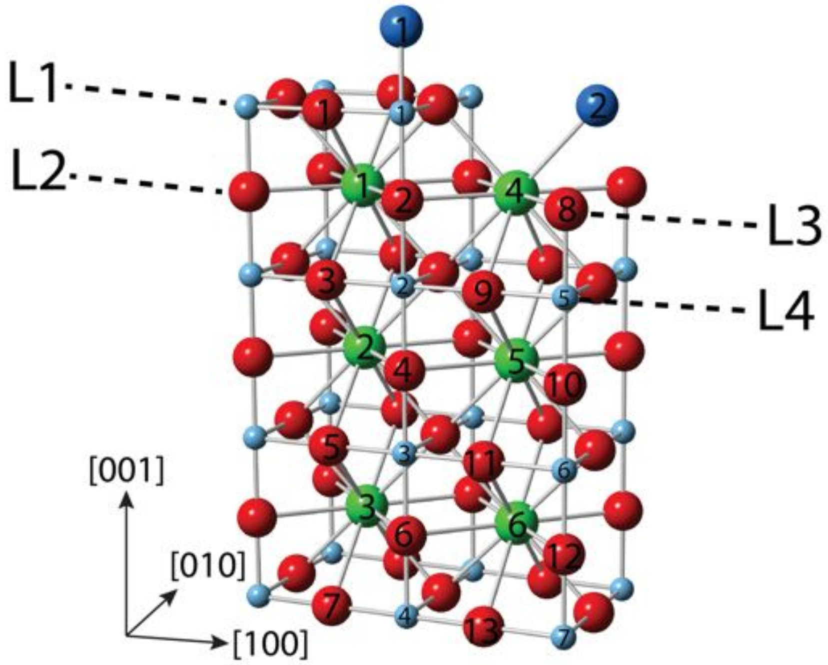

Figure 6.4: Ball and stick model representation of $SrTiO_3(001)$ surface with water adsorption. Colour scheme same as Figure 6.1. Large dark blue spheres are water species either OH or H_2O. The labelled layers (L1, L2, L3, and L4) are the same as used in Table 6.1. The numbering of the Ti, Sr, and O atoms is the same as used in 6.2 and III.

The X-ray scattering strength is proportional to the electron density, and thus it is extremely difficult in a surface X-ray diffraction experiment to distinguish between H_2O, OH, and O on the STO surface because of the low scattering contribution from hydrogen. However, in order to deduce whether an oxygen is in its atomic form, protonated or doubly protonated bond distances can provide indirect evidence. Starting first with the TiO_2 terminated terrace, the distance between the oxygen of the (the assumed) $H_2O(1)$ and Ti(1) was found to be 2.30 ± 0.04 Å which is in good agreement with the literature where bond distances of 2.21 Å [28], 2.26 Å [9] and 2.27 Å [10] are published for molecular water adsorption. This is strong evidence that the mode of adsorption favoured for the TiO_2 terminated terrace is molecular in nature. For the SrO terminated terrace, the distance between Sr(4) and the oxygen in OH(2) was found to be 2.60 ± 0.04 Å again in excellent agreement with the literature values of 2.59 Å [28], 2.61 Å [9] and 2.55 Å [10]. The occupancies of sites $H_2O(1)$ and OH(1) were found to be 0.89 ± 0.07 and 0.79 ± 0.06 respectively. Furthermore, in the literature it is suggested that with the dissociation of the water molecule, the liberated hydrogen atom forms a H-bond with the surface oxygen atom i.e. O(8) of the substrate creating a second OH. In our case this determination is very difficult because of the insensitivity of this atom to out-of-plane displacements and its large associated error. This is mainly due to both the low atomic number of the oxygen atom O(8) and its low site occupancy, as indicated in Table 6.1. Nevertheless, the excellent agreement of the bond distances of Sr(4) and OH(2) leads us to believe dissociation is the favoured adsorption mode.

6.3.3 Nitrogen

After the measurements were completed for the water-adsorbed surface, a flow of nitrogen was used to evaporate the water droplet. Since the atmosphere within the chamber after this process is saturated with water it was expected that the surface would be very similar to the water covered surface and was thus used as the starting point for analysis. The best-fit produced a χ^2 value of 1.5 and R-value of 19% and the comparison between the experimental data and best-fit are shown in Figure 6.6 There was no change in the TiO_2/SrO ratio, the occupancies of the TiO_2 and SrO in the first layers compared with the other two surfaces studied. The roughness parameter was 0.4 as for the STO(001) liquid water interface. All of this points to the stoichiometry being insensitive to water adsorption. By inspection of Figure 6.2 and Table 6.3 it is obvious that the N_2 dried surface largely resembles the water-covered surface. This

Table 6.3: The experimentally determined atomic displacements in the [001] direction, i.e. normal to the surface, for the UHV prepared, water adsorbed, and nitrogen dried $SrTiO_3$ (001) surface. The atom labels correspond with those seen in Figures 6.1 and 6.4. A negative value indicates an atom displacing towards the bulk.

Atom	Atomic Displacements (Å)		
	Clean (UHV)	Water	N_2
Ti(1)	-0.12 ± 0.02	-0.12 ± 0.03	-0.23 ± 0.05
O(1)	-0.23 ± 0.06	-0.16 ± 0.07	0.23 ± 0.13
Sr(1)	-0.06 ± 0.00	0.09 ± 0.01	0.14 ± 0.01
O(2)	0.04 ± 0.02	0.04 ± 0.06	-0.06 ± 0.09
Ti(2)	-0.16 ± 0.01	0.19 ± 0.01	0.11 ± 0.01
O(3)	-0.03 ± 0.01	-0.23 ± 0.02	-0.06 ± 0.03
Sr(2)	-0.11 ± 0.00	0.04 ± 0.01	0.04 ± 0.01
O(4)	-0.02 ± 0.02	0.23 ± 0.02	0.23 ± 0.04
Ti(3)	-0.15 ± 0.01	0.06 ± 0.01	0.05 ± 0.01
O(5)	0.05 ± 0.01	0.02 ± 0.08	0.05 ± 0.03
Sr(3)	-0.01 ± 0.00	0.09 ± 0.01	0.04 ± 0.01
O(6)	-0.22 ± 0.01	-0.18 ± 0.02	-0.13 ± 0.03
Ti(4)	-0.04 ± 0.00	0.01 ± 0.01	-0.05 ± 0.01
O(7)	-0.19 ± 0.01	0.12 ± 0.08	-0.08 ± 0.02
Sr(4)	0.10 ± 0.01	0.23 ± 0.04	0.12 ± 0.04
O(8)	0.27 ± 0.05	0.03 ± 0.21	0.04 ± 0.37
Ti(5)	0.09 ± 0.01	-0.12 ± 0.01	0.02 ± 0.01
O(9)	-0.08 ± 0.02	0.23 ± 0.02	0.23 ± 0.03
Sr(5)	0.10 ± 0.01	0.06 ± 0.01	0.08 ± 0.01
O(10)	-0.23 ± 0.01	-0.23 ± 0.02	-0.23 ± 0.03
Ti(6)	0.14 ± 0.01	-0.02 ± 0.01	-0.08 ± 0.01
O(11)	0.11 ± 0.01	-0.11 ± 0.02	-0.03 ± 0.01
Sr(6)	0.09 ± 0.01	0.01 ± 0.01	0.02 ± 0.01
O(12)	0.20 ± 0.01	0.23 ± 0.08	-0.23 ± 0.02
Ti(7)	0.09 ± 0.00	0.01 ± 0.01	0.03 ± 0.01
O(13)	0.01 ± 0.01	0.19 ± 0.02	-0.12 ± 0.02

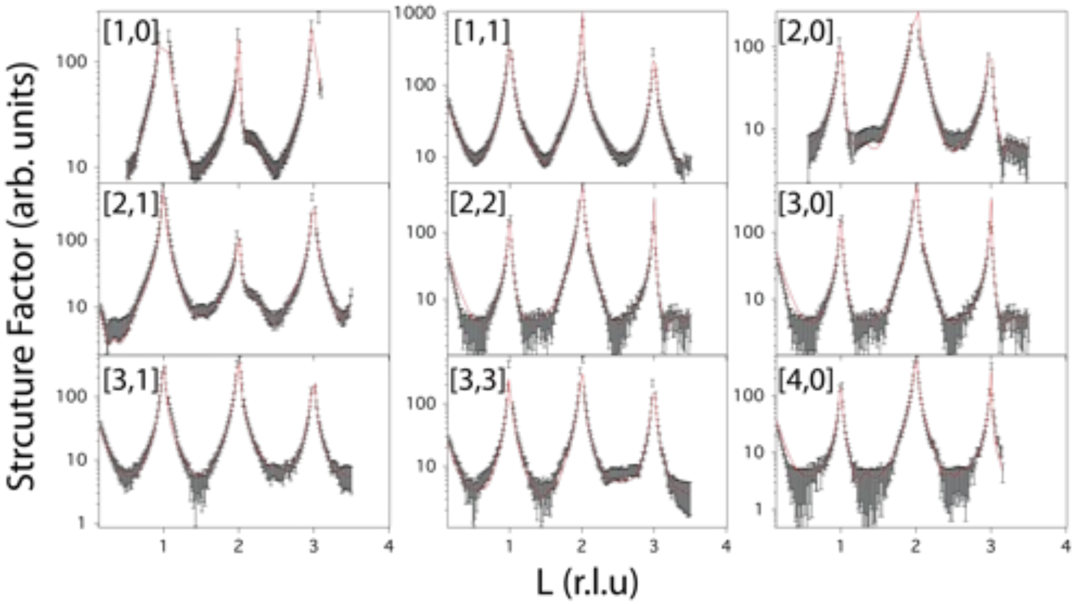

Figure 6.5: CTRs for the water adsorbed $SrTiO_3(001)$ surface. Black error bars and solid red line are experimental and calculated structure factors (best-fit), respectively.

is especially the case for the surface cations (Ti(1) and Sr(1)) of the TiO_2 terminated terrace, which are displaced in similar directions and magnitudes. The largest difference between the N_2 dried and the water covered surface is that the sites $H_2O(1)$ and OH(1) i.e the oxygen atoms representing the H_2O/OH molecule, were found to have an occupancy of 0 by the fit. Furthermore, larger displacements and error bars are seen for the anions (O(1) and O(2)), which now are displaced by similar magnitudes but in opposite directions. As for the SrO terminated terrace, the cations and anions show similar displacements to the water-covered surface. The close similarity of atomic displacements between this condition and the water-covered condition lead us to believe that most likely a highly disordered overlayer of water is present on the surface.

6.4 Conclusions

In summary, these SXRD results demonstrate that the $SrTiO_3$ (001) surface, prepared via argon ion sputtering and annealing in 1 x 10^{-2} mbar O_2 partial pressure, is comprised of terraces which exhibit either a SrO or TiO_2 terminating layer. They cover equally large areas and the

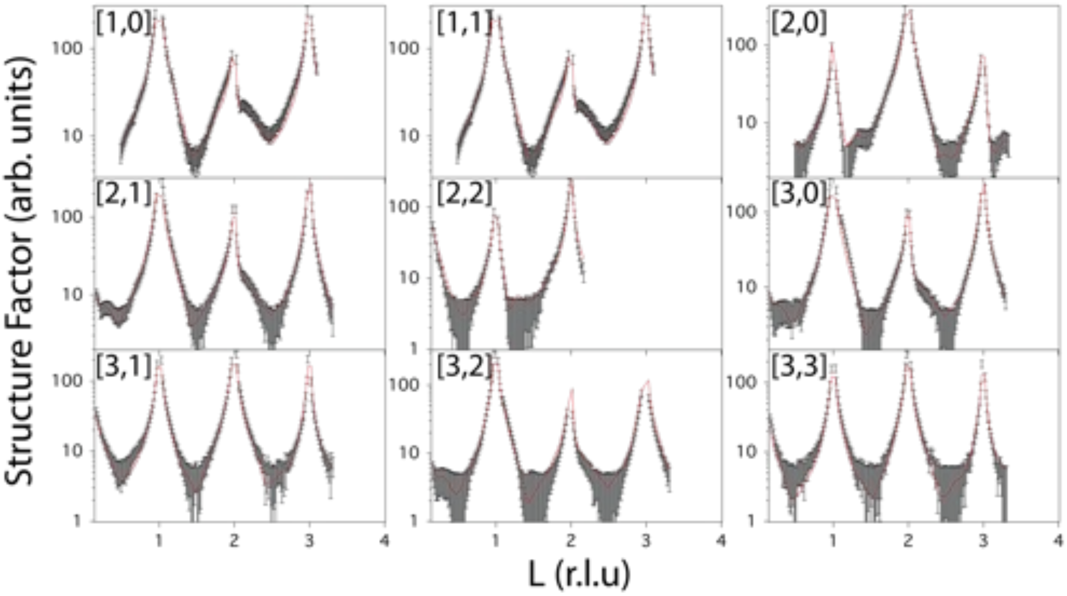

Figure 6.6: CTRs for the nitrogen blow-dried $SrTiO_3$(001) surface. Black error bars and solid red line are experimental and calculated structure factors (best-fit), respectively.

resulting scattering signal is an incoherent superposition of the signals originating from both terraces. The first two layers of both terraces are only partially occupied and this leads to a final surface coverage TiO_2:SrO ratio of 68:32. When contacting this surface under controlled conditions with a drop of water, our results suggest that the adsorption mode favoured for the TiO_2 terminated terrace is molecular in nature with the bonding position atop of the surface Ti atom. On the other hand, for the SrO terminated terrace it appears that dissociation is the favoured adsorption mode with the oxygen atom of the OH positioned where an oxygen would be located if the perovskite lattice was extended. Removal of the water droplet with a flow of nitrogen led to a surface structure that is similar to the water-covered surface however, most likely, with a disordered overlayer of water. This is reflected in the similarity of atomic displacements between the water covered surface and nitrogen dried surface. The ratio of the TiO_2 and SrO covered surface areas and the layer occupancies did not change over the course of the experiment proving that water is not influencing the cation concentration of the STO(001) surface.

To further develop the work presented in this chapter focus should be placed on an STM investigation of the $SrTiO_3$ (001) surface to determine whether the proposed model for the clean surface is correct. It is expected that the surface will be populated with half unit cell step heights accompanied with very rough terraces. This investigation could be taken further by adsorbing liquid water *ex situ* to determine if the mixed dissociated model presented is correct.

The water/$SrTiO_3$ system has been extensively studied over the years however research is still far away from finding a full understanding. New technologies have emerged and are emerging in which water adsorption on the surface of $SrTiO_3$ can play a major role in the physics and chemistry of the application. One such example is oxide-based electronics, where a layer of an insulator (eg. lanthanum titanate) grown on insulating $SrTiO_3$ forms a two-dimensional electron gas at the interface causing it to become metallic. The performance of $SrTiO_3$ is critically dependant on its surface structure; oxygen vacancies on the surface produce a carrier charge density at the interface. It is thus essential to have an understanding of the structure of water adsorption on $SrTiO_3$.

References

[1] F. Wagner, S. Ferrer, G. Somorjai, Surf. Sci., 101, 462, (1980)

[2] S. K. Hodak, T. Supasai, A. Wisitsoraat, J. H. Hodak, J. Nanosci. Nanotechnol., 10, 7236, (2010)

[3] P. Blennow, A. Hagen, K. K. Hansen, L. R. Wallenberg, M. Mogensen, Solid State Ion., 179, 2047, (2008)

[4] W. J. Shi, S. J. Xiong, Surf. Sci., 604, 1987, (2010)

[5] L. Q. Wang, K. F. Ferris, G. S. Herman, J. Vac. Sci. Technol. Vac. Surfaces Films., 20, 239244, (2002)

[6] W. Wei, Y. Dai, M. Guo, Y. Ma, B. Huang, J. Solid State Chem., 187, 64, (2012)

[7] K. Iwahori, S. Watanabe, M. Kawai, K. Kobayashi, H. Yamada, K. Matsushige, J. Appl. Phys., 93, 3223, (2003)

[8] J. D. Baniecki, M. Ishii, K. Kurihara, K. Yamanaka, T. Yano, K. Shinozaki, T. Imada, Y. Kobayasji, J. Appl. Phys., 106 (2009)

[9] R. A. Evarestov, A. V. Bandura, V. E. Alexandrov, Surf. Sci., 601, 1844, (2007)

[10] B. B. Hinojosa, T. Van Cleve, A. Asthagiri, Mol. Simul., 36, 604, (2010)

[11] J. Zegenhagen, B. Detlefs, T. L. Lee, S. Thiess, H. Isern, L. Petit, L. Andre, J. Roy, Y. Mi, I. Jourmard, J. Electron Spectrosc. Relat. Phenom., 178, 258, (2010)

[12] F. U. Renner, Y. Grunder, J. Zegenhagen, Rev. Sci. Instrum., 78, 033903, (2007)

[13] E. Vlieg, J. Appl. Crystallogr., 33, 401, (2000)

[14] I. K. Robinson, Handbook of Synchrotron Radiation (North Holland, Amsterdam, 1991) Vol. 3

[15] G. Charlton, S. Brennan, C. A. Muryn, R. McGrath, D. Norman, T.S. Turner, G. Thornton, Surf. Sci., 457, L376, (2000)

[16] A. Fragneto, G. M. De Luca, R. Di Capua, U. Scotti di Uccio, M. Salluzzo, X. Torrelles, Appl. Phys. Lett., 91, 101910, (2007)

[17] V. Ravikumar, D. Wolf, V. Dravid, Phys. Rev. Lett., 74, 960, (1995)

[18] Q. D. Jiang, J. Zegenhagen, Surf. Sci., 338, L882, (1995)

[19] M. R. Castell, Surf. Sci., 516, 33, (2002)

[20] http://meetings.aps.org/link/BAPS.2012.MAR.V18.10

[21] N. Erdman, K. R. Poeppelmeier, M. Asta, O. Warschkow, D. E. Ellis, L. D. Marks, Nature., 419, 55, (2002)

[22] R. Herger, P. R. Willmott, O. Bunk, C. M. Schleptz, B. D. Patterson, B. Delley, Phys. Rev. Lett., 98, 076102, (2007)

[23] A. E. Becerra-Toledo, M. S. J. Marshall, M. R. Castell, L. D. Marks, J. Chem. Phys., 136, 214701, (2012)

[24] K. Johnston, M. R. Castell, A. T. Paxton, M. W. Finnis, Phys. Rev. B., 70, 085415, (2004)

[25] N. P. Guisinger, T. S. Santos, J. R. Guest, T. Y. Chien, A. Bhattacharya, J. W. Freeland, M. Bode, ACS Nano., 3, 4132, (2009)

[26] J. Goniakowski, C. Noguera, Surf. Sci., 365, L657, (1996)

[27] R. I. Eglitis, D. Vanderbilt, Phys. Rev. B., 77, 195408, (2008)

[28] H. Guhl, W. Miller, K. Reuter, Phys. Rev. B., 81, 155455, (2010)

Chapter 7

Conclusions and Future Work

This thesis investigates the adsorption of water, in both the gas and liquid phase, on three important model metal oxide surfaces; $TiO_2(110)$, $ZnO(10\bar{1}0)$ and $SrTiO_3(001)$.

Using STM, we were able to show that an ordered (2 x 1) overlayer is formed after exposing the $TiO_2(110)(1 \times 1)$ surface to a partial pressure 1×10^{-6} mbar H_2O for ~3 h. Previous work in the group, by Tom Woolcot, has shown that a similar overlayer is formed when dipping the surface in liquid water and PES measurements suggest that the overlayer is comprised of hydroxyls only. Repeating the experiment on a $TiO_2(110)(1 \times 1)$-(1×2) surface revealed that the rows of OH in the overlayer lie in registry with the Ti_{5c} rows of the substrate.

SXRD measurements agree with the STM findings showing a best-fit theoretical model described by every other Ti atom in the [001] direction occupied with an OH in an atop position. The same average structure was found after exposing the surface to several partial pressures of H_2O ranging from 1×10^{-6} mbar up to 10 mbar and after the dipping the surface in ~20 ml ultra pure deaerated liquid H_2O for ~15 s. With the use of an electrochemical cell, *in-situ* SXRD measurements were collected for immersion of liquid water on the surface. It was found that the contact layer of the interface was similar to the partial pressure and dipping structures i.e every other Ti atom in the [001] direction occupied with an OH in an atop position. However, now there was the presence of a hydration layer described by three water adsorption sites; above the bridging oxygen/hydroxyl and bridging between the terminal hydroxyl and bridging bridging oxygen/hydroxyl.

Further studies on this system may concentrate on the importance of when the (2 x 1) overlayer is formed in terms of H_2O coverage. This experiment would simply be an extension of the attempts made in this thesis, where the $TiO_2(110)(1 \times 1)$ surface was exposed to different partial pressures and coverages of H_2O. The highest exposure of water obtained in this work was 100 L (1×10^{-7} mbar for 10 s) however only bridging hydroxyls not terminal hydroxyls were seen to be present on the surface. Elucidation of this H_2O critical exposure/coverage, coupled with DFT and MD simulations, may provide information to the exact nature of the overlayer. Another possible investigation of interest is to repeat the above mentioned experiments on the highly reduced $TiO_2(110)(1 \times 2)$ surface to determine the adsorption behaviour of the H_2O molecules with the strands of (1 x 2) reconstruction.

The interaction of H_2O with the ZnO($10\bar{1}0$) surface has been investigated as a function of water coverage from monolayer to the multilayer regime using SXRD. Ancillary measurements, using STM, on the surface after adsorbing 10 L H_2O (~1 ML) revealed an ordered overlayer with (2 x 1) periodicity. SXRD measurements of the nominally UHV (5 x 10^{-9} mbar) surface produces a (1 x 1) structure consisting of an overlayer that consists of H_2O/OH adsorbates bonded to the surface Zn in off tetrahedral sites. Chemical information (H_2O versus OH) could not be obtained due to the relatively large error bars on the atomic positions. The overlayer is of monolayer coverage and was formed from the H_2O in the residual vacuum. After these measurements, the surface was exposed to a constant partial pressure of 5 x 10^{-7} mbar of H_2O. We detect the presence of a second water layer with partial occupancy and no change to the contact layer. Significant changes occurred when exposing the surface to 8 mbar partial pressure of H_2O. The H_2O/OH molecule of the contact layer shifts to an atop position of the surface Zn and the second water layer is now fully occupied.

The ZnO($10\bar{1}0$) / H_2O interface has been widely studied at sub-monolyer to monolayer coverages however, supsrisingly very little is known when going beyond monolayer coverage. An interesting technique to apply to this system is ambient pressure XPS (AP-XPS) as it could provide key information in determining the structural changes in the contact layer at higher coverages.

Using SXRD, we have demonstrated that the $SrTiO_3(001)$ surface under UHV conditions, prepared via argon ion sputtering and annealing in 1 x 10^{-2} mbar O_2 partial pressure, is comprised of terraces which exhibit either a SrO or TiO_2 terminating layer. They cover equally large areas and the resulting scattering signal is an incoherent superposition of the signals originating from both terraces. The first two layers of both terraces are only partially occupied and this leads to a final surface coverage TiO_2:SrO ratio of 68:32. With the use of an electrochemical cell, analysis after contacting this surface with a droplet of water under controlled conditions suggests that the adsorption mode favoured for the TiO_2 terminated terrace is molecular in nature with the bonding position atop of the surface Ti atom. On the other hand, for the SrO terminated terrace it appears that dissociation is the favoured adsorption mode with the oxygen atom of the OH positioned where an oxygen would be located if the perovskite lattice was extended. The removal of the water droplet with a flow of nitrogen revealed a structure similar to that of the water-covered surface, as reflected by the similarity in atomic displacements. The ratio of the TiO_2 and SrO covered surface areas and the layer occupancies did not change over the course of the experiment proving that water is not influencing the cation concentration of the $SrTiO_3(001)$ surface.